Universidade do Porto
FEUP Faculdade de Engenharia

MESTRADO INTEGRADO EM BIOENGENHARIA

RGD-Based Metal Organic Frameworks For Selective Delivery Of Therapeutics To Tumour Vasculature

Luís Daniel Ferreira Vasconcelos

Dissertação submetida para obtenção do grau de
MESTRE EM BIOENGENHARIA – RAMO DE BIOTECNOLOGIA MOLECULAR

Presidente do Júri: Alexandre Tiedtke Quintanilha
(Professor Catedrático do Departamento de Biologia Molecular do Instituto de Ciências Biomédicas Abel Salazar da Universidade do Porto)

Orientador académico: Luís Miguel Gales Pereira Pinto
(Professor Associado do Departamento de Biologia Molecular do Instituto de Ciências Biomédicas Abel Salazar da Universidade do Porto e Investigador Principal do grupo Molecular Biophysics do Instituto de Biologia Molecular e Celular da Universidade do Porto)

Porto, Julho de 2012

MESTRADO INTEGRADO EM BIOENGENHARIA 2011/2012

Editado por

FACULDADE DE ENGENHARIA DA UNIVERSIDADE DO PORTO
Rua Dr. Roberto Frias
4200-465 PORTO
Portugal

Tel. +351 225 081 400

Fax +351 225 081 440

Correio electrónico: feup@fe.up.pt

Endereço electrónico: http://www.fe.up.pt

"Like all other things, the sea will not endure forever. But by our standards it is eternal. As we look across its moving surface, remembering that it has scarcely changed since the first man saw the light of day, our minds wash clear of the petty ambitions and jealousies and meannesses that form so large part of everyday existence. From the waters that gave us life we may draw not only food for our bodies and raw materials for our factories, but also refreshment for our spirit."

Sir Arthur C. Clarke

ABSTRACT

Metal Organic Frameworks (MOFs) are a class of hybrid materials formed by the self-assembly of organic bridging ligands and metal connecting centers [1, 2]. A distinct property of these materials is their extremely high and adaptable porosity [3], which makes them potentially useful to drug loading [4]. MOFs pores are usually large and with regular geometry, which facilitates the design of delivery vehicles for a controlled and progressive release [4]. Moreover, these materials possess other potential advantages when compared to other nanomedicine strategies, such as their biocompatibility and versatile architecture, both key issues for maximizing dug loading and optimizing release kinetics [1]. To these already remarkable physicochemical properties we wish to add target delivery.

The Argine-Glycine-Aspartic Acid (RGD) sequence represents a basic module for targeting drugs and imaging agents to αvβ3-integrin expressing tumor vasculature [5, 6]. In this project we have hypothesized that a MOF, build up from a wild type or a N-terminal carboxylate modified, linear RGD peptide and a transition metal, under the appropriate reaction conditions, would form porous crystalline frameworks capable of targeting αvβ3-integrin expressing cells.

Two main distinct strategies were used in order to build RGD based frameworks. One based on the elementary binary system of metal cation and RGD ligand and another which involved the synthesis of a rigid scaffold formed by metal atoms and Adenine nucleobase where the flexible RGD peptide could potentially bind as a coligand.

Attempts to prepare RGD-based MOFs were done following the conventional hydrosolvothermal route playing on several parameters, such as the reaction time, temperature, stoichiometry, pH, solvents, additives, metal cation (Fe(II), Zn(II), Mn(II), Cu(II)), etc. Crystallization trials using vapor diffusion techniques and natural evaporation of solvent were done to optimize crystal formation conditions. Even though, in the course of this work no single crystal of the complex was obtained that was suitable for X-ray diffraction.

Characterization of products was made by a combination of techniques. The successful formation of the metal peptide coordination complexes was determined by Fourier Transform Infrared Spectroscopy and Circular Dichroism. Topological analysis of the synthesis products was made by Scanning Electron Microscope (SEM) and elemental analysis was measured by Energy Dispersive analysis of X-rays Spectroscopy (EDS).

Computational Methods were also used to perform a preliminary analysis of the interaction preferences between the motif Arg-Gly-Asp and the metal atom Zn(II)

ACKNOWLEDGEMENTS

First of all, I am especially grateful to my supervisor, Professor Luís Gales for making me part of his group at IBMC, for his commitment to interdisciplinary science and for his constant support in the last couple of years. Thanks also to Joana Durão for all the help and good atmosphere in the lab.

I also owe a great deal of gratitude to a number of other colleagues and professors outside IBMC. Those especially deserving of a mention include Dr. Sérgio Sousa and Professor Alexandre Magalhães at FCUP for the development of the Molecular Dynamics Simulations, Silvia Maia and Professor Paula Gomes at FCUP for the contribution in the synthesis of sucRGD peptide, Dr. Filipe Paz and Professor João Rocha at CICECO for all the valorous discussions and for letting me use their FTIR and RAMAN spectrometers, Dr. Eduardo Tejera at FFUP for all the discussions about coordination chemistry and Dr. Khirud Gogoi at UCSD for all the shared knowledge on peptide synthesis. I have learned a great deal from all of them.

I am sincerely grateful to Professor Natércia Teixeira at FFUP, for all her kindness, patience and understanding.

Finally, my greatest appreciation goes to Professor Steven Dowdy at UCSD, for being an inspiration and for opening the doors of cutting-edge science for me.

ABREVIATIONS

AA	Aminoacid
AdeH	Adenine
AP	Adipic Acid
AZT	Azidothimidine
BDC	1, 4 Benzene Dicarboxylate
BioMOF	Biocompatible Metal Organic Framework
Bu	Busulfan
CD	Circular Dichroism
CDV	Cidofovir
DAD	Diode Array Detector
DCM	Dichloromethane
DIPC	Diisopropylcarbodiimide
DMAP	N, N – dimethylaminopyridine
DNA	Desoxyribonucleic Acid
DMF	N, N – dimethylformamide
ECM	Extra Celular matrix
EDS	Energy Dispersive of X-rays Spectroscopy
ESI-IT	Electrospray Ionization – Ion Trap
FTIR-ATR	Fourier Transform Infrared Spectroscopy - Attenuated Total Reflectance
HD	Hanging Drop
HOBt	Hydroxybenzotriazole
LC	Liquid Chromatography
LD	Lethal Dose
MD	Molecular Dynamics
MIDAS	Metal Ion-Dependent adhesion Site
MIL	Materials of Institute Lavoisier
MOF	Metal Organic framework
MPF	Metal Peptide Framework
MS	Mass Spectrometry
MTBE	Methyl-tert-butyl ether
RGD	Arginine-Glycine-Aspartic-Acid
RNA	Ribonucleic Acid
RP –HPLC	Reverse Phase High Performance Liquid Chromatography
SBF	Simulated Body Fluid
SEM	Scanning electron Microscopy
SD	Sitting Drop
SPPS	Solid Phase Peptide Synthesis
SucRGD	Succinated Arginine-Glycine-Aspartic-Acid
TEA	Triethylamine
TFA	Trifluoroacetic acid

CONTENTS

CHAPTER 1

1. INTRODUCTION

Metal Organic Frameworks (MOFs), also known as Coordination Polymers, are the latest class of ordered porous solids [7-10]. First publications referring to Coordination Polymers date back from the 1960s [11], the first seminal paper that established the new field of study, was published in the early 1990s by Robson [12] and the term Metal Organic Framework was popularized by Yaghi et al. around 1995 [13]. Since then a lot of potential applications have been explored in strategic domains such as catalysis [14-16], selective adsorption of gases [17, 18], fabrication of membranes [19, 20] or thin films [21, 22], contrasting agents [23], enantioselective separation of molecules [24], magnetism and others [25-28]. One of their distinguishable advantages when compared to their organic (carbon) or inorganic counterparts (zeolites, silica), is the possibility to easily set their composition by changing its components, the metal and/or the organic linker [29]. The type of linker is almost unlimited, ranging from polycarboxylates, phosphonates, sulphonates, imidazoles, amines, pyridyl, phenolates and interestingly aminoacids [30] and polypeptides [31]. Thousands of MOFs have been reported with a few hundred showing to be porous [32]. When compared to zeolites, besides their wider chemical versatility, MOFs structure exhibit a bigger set of pore sizes and shapes (tunnels, cages, etc), sometimes presenting a flexible, sometimes the so called breathing porosity [3], which allows a reversible adaptation to the adsorbate [33, 34]. The chance to functionalize the organic linker constitutes another major advantage of MOFs. This can be done during or after synthesis by adding various organic functionalities (polar, apolar), thus changing the physicochemical properties of the solid [35-37].

1.1. MOFs For Biomedical Applications

The use of nanocarriers that ensure an efficient therapy is dependent of its capacity to (1) efficiently entrap drugs with high payloads, (2) control the release and avoid the “burst effect” (important release within the first minutes), (3) control matrix degradation, (4) offer the possibility to easily engineer its surface to control *in vivo* fate and (5) be detectable by imaging techniques [4]. Future molecular medicine strategies need to associate therapeutic and diagnosis capacities in order to turn personalized medicine a reality [4]. The next step comprehends the development of a nanocarrier that can serve both as drug carrier and as diagnostic agent – satisfy criteria (4) and (5) – to evaluate drug distribution and treatment efficiency (theranostics) [4].

The synthesis of new bioactive compounds of very high molecular weight with therapeutic activity and/or with low aqueous solubility becomes increasingly complex and the process for their commercialization very slow [38]. Current therapeutics are limited by their non specific distribution throughout the body leading to high doses, rapid clearance, poor pharmacokinetics, and high side effects [39, 40]. Despite the development of different strategies to improve the efficacy of conventional drugs, nanoparticle based therapeutics have received an increase amount of attentions and funds over the past 20 years [41]. Many of the drawbacks of small molecules drugs can be overturned through the use of these novel systems. Usually, a nanoparticle therapeutic is composed of an active agent incoporated within the nanoparticle carrier; a wide diversity of nanocarriers have been used for this purpose, such as polymeric nanoparticles, micelles, lipossomes, iron oxide and gold [42, 43]. These nanomaterials are characterized for their properties such as small size, high drug loading, defined surface properties, improved pharmacokinetics, and biocompatibility [44-47].

These nanocarriers systems usually allow a better control of the drug plasmatic levels, increasing the efficiency and decreasing the toxicity, as well as an increase in the drug stability by protection from biodegradation. Additionally some carriers can include targeting ligands such as peptides [6] or nucleotides [48] that can address drug release to diseased tissues (*e.g*. tumor regions) and can be engineered to contain multiple agents (e.g. imaging and therapeutic agents), both of which are much harder to achieve by conventional therapeutics [49].

1.2. Coordination Chemistry Basics

Most metal ions react with electron-pair donors to form coordination compounds or complexes. The donor species, or ligand, must have at least one pair of unshared electrons available for bond formation [50].

The number of covalent bonds that a cation tends to form with electron donors is its coordination number. Typical values for coordination numbers are two, four, and six. The species formed as a result of coordination can be electrically positive, neutral or negative [50].

Chelates are a particular class of coordination compounds, produced when a metal ion coordinates with two (or more) donor groups of a single ligand to form a five- or six-membered heterocyclic ring [50]. One example is the copper complex with glycine, where copper bonds to both oxygen of the carboxyl group and the nitrogen of the amine group (Scheme 1).

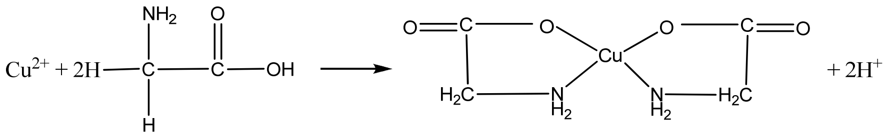

Scheme 1

A ligand that has a single donor group, such as ammonia, is called unidentate, whereas one such as glycine, which has two groups available for covalent bonding, is called bidentate [50]. Each ligand in a complex is a Lewis base with at least one pair of electrons that forms a coordinate covalent bond to the central atom or ion. Because both electrons in the bond come from the ligand, is said that the ligand coordinates to the metal [51]. The ligands directly attached to the central ion in a complex (conventionally enclosed within brackets) make up the coordination sphere of the central ion. The number of points where ligands are attached to the central metal atom is called the coordination number of the complex [51].

1.2.1. Electronic And Geometric Structures Of Metals In Biological Systems

Common geometries adopted by transition metal ions are illustrated in Figure 1. In biological systems these geometries are usually distorted in both bond length and bond angle.

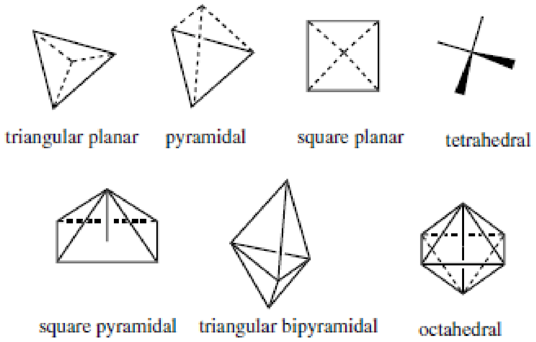

Figure 1| Common transition metal coordination geometries (adapted from [52])

As a consequence of their partially filled *d* orbitals, transition metals exhibit variable oxidation states and a rich variety of coordination geometries and ligand spheres [52]. Although a free metal ion would exhibit degenerate *d*-electron energy levels, ligand field theory describes the observed splitting of these *d*-electrons for metal ions in various ligand environments. In all cases the amount of stabilization or destabilization of *d*-electron energy levels centers about the so-called barycenter of unsplit *d*-electron energy levels [52]. The most important of these for bioinorganic applications are shown in Figure 2 for octahedral, tetrahedral, and square-planar ligand fields.

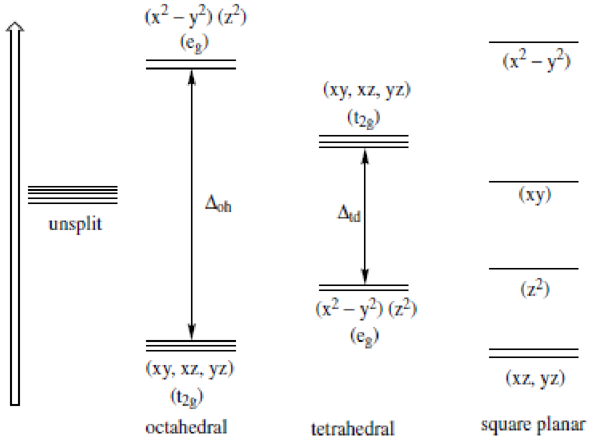

Figure 2| Approximate energy levels for d electrons in octahedral, tetrahedral, and square-planar fields (adapted from [52])

The $t_{2g}(d_{xy}$, d_{yz}, and $d_{xz})$ and $e_g(d_{x2\text{-}y2}$ and d_{z2}) energy level designations identify symmetry properties of the *d* orbitals and are often used to indicate the degenerate energy levels [52]. Generally, the energy gap for tetrahedral fields is approximately one-half that for octahedral fields, and that for square-planar fields is approximately $1.2\Delta_{oh}$. Many thermodynamic and kinetic properties of transition metal coordination complexes can be predicted by knowing the magnitude of Δ [52]. Measurement of ultraviolet and visible absorption spectra of transition metal complexes that arise from these quantum mechanically forbidden *d–d* transitions provide a measure of Δ [52]. To describe the d-orbital splitting effect for the octahedral field, one should imagine ligand spheres of electron density approaching along the *x*, *y*, and *z* axes, where the d_{x2-y2} and d_{z2} lobes of electron density point. Figure 3 illustrates representations of high-probability electron orbit surfaces for the five *d* orbitals [52].

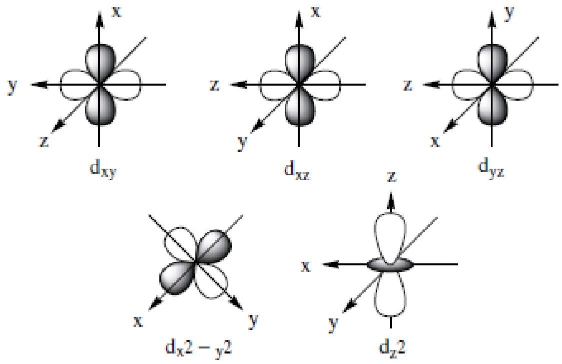

Figure 3| Representations of the five *d* orbitals along *x*, *y*, and *z* axes (adapted from [52])

1.3. Biocompatible Metal Organic Frameworks

One of the most recently explored application for porous solids is biomedicine, what brought the necessity for MOFs to be constructed from benign, biocompatible building blocks [53]. To present, toxicity studies regarding MOFs are very scarce and the available data is mostly restricted to the toxicity evaluation of metals and linkers taken individually [32]. Though, it is obvious to consider only metals that exhibit acceptable toxicity. As a general rule, the decision to exclude one composition for biomedical application depends on several parameters, such as the balance between the risk and benefit, the kinetics of degradation, biodistribution, accumulation in tissue and organs and excretion from the body [54].

1.3.1. Metals in biological systems

It is relatively easy to point out the most appropriate metals to use, based on their toxicity estimated by their oral lethal dose 50 (LD50). These metals include Ca, Mg, Zn, Fe, whose toxicity range from few µg/kg up to more than 1 g/kg (calcium) (Table 1)

Table 1| Oral LD50 (Rats) and Daily Requirements (Humans) of selected metals (adapted from [32])

Metal	LD50 (g/kg)	Daily dose (mg)
Zr	4.1	0.05
Ti	25	0.8
Cu	0.025	2
Mn	1.5	5
Fe	0.45	15
FeO	30	
Zn	0.35	15
Mg	8.1	350
Ca	1	1000

These values depend on the chemical formulation (salts, metal conteranion, and oxidation state). Besides the LD50 criterion, it is important to consider the metal daily dose, particularly when repetitive administration of the MOF is involved.

Metal ions may serve multiple functions, depending on their location within the biological system. Many chemical and physical properties of the elements and their ions are responsible for their inclusion in biological systems. These include ionic charge, ionic radius, ligand preferences, preferred coordination geometries, spin pairing, systemic kinetic control, and the chemical reactivity of the ions in solution. Table 2 shows some of these properties for metals already used in the synthesis of MOFs.

Table 2| Metals in biological systems (adapted from [52])

Metal	Coordination Number, Geometry	Preferred Ligands	Funtions and Examples
Magnesium, Mg^{2+}	6, octahedral	O-Carboxylate, phosphate	Structure in hydrolases, isomerases, phosphate transfer, trigger reactions
Calcium, Ca^{2+}	6-8, flexible	O-Carboxylate, carbonyl, phosphate	Structure, charge carrier, phosphate transfer, trigger reactions
Zinc, Zn^{2+} (d10)	4, tetrahedral	O-Carboxylate, carbonyl, S-thiolate, N-imidazole	Structure in zinc fingers, gene regulation, anhydrases, dehydrogenases
Zinc, Zn^{2+} (d10)	5, square pyramid	O-Carboxylate, carbonyl, N-imidazole	Structure in hydrolases, peptidases
Manganese, Mn^{2+} (d5)	6, octahedral	O-Carboxylate, phosphate, N-imidazole	Structure in oxidases, photosynthesis
Manganese, Mn^{2+} (d4)	6, octahedral	O-Carboxylate, phosphate, hydroxide	Structure in oxidases, photosynthesis
Iron, Fe^{2+} (d6)	4, tetrahedral	S-Thiolate	Electron transfer, nitrogen fixation in nitrogenases, electron transfer in oxidases
Iron, Fe^{2+} (d6)	6, octahedral	O-Carboxylate, alkoxide, oxide, phenolate	
Iron, Fe^{2+} (d6)	6, octahedral	N-Imidazole, porphyrin	Dyoxigen trasnport in hemoglobin and myoglobin
Iron, Fe^{3+} (d5)	4, tetrahedral	S-Thiolate	Electron transfer, nitrogen fixation in nitrogenases, electron transfer in oxidases
Iron, Fe^{3+} (d5)	6, octahedral	O-Carboxylate, alkoxide, oxide, phenolate	
Copper Cu^{+} (d10) Cu^{2+} (d9)	4, tetrahedral	S-Thiolate, thioether, N-imidazole	Electron transfer in Type I blue copper proteins
Copper, Cu^{2+} (d9)	5, square pyramid; 6 tetragonal	O-Carboxylate, N-imidazole	Type II copper oxidases, hydrolase; Type III copper hydrolases, dioxygen transport in hemocyanin
Copper, Cu^{2+} (d9)	4, square planar	O-Carboxylate, N-imidazole	Type II copper oxydases

Ligand preferences and possible coordination geometries of the metal center are important bioinorganic principles. Metal-ligand preferences is closely related to the hard-soft acid-base nature of metals and their preferred ligands [52] (Table 3).

Generally, hard metal cations form their most stable compounds with hard ligands, whereas soft metal cations form their most stable compounds with soft ligands. Hard cations can be thought of as small dense cores of positive charge, whereas hard ligands are usually the small highly electronegative elements or ligand atoms within a hard polyatomic ion [52].

Table 3| Hard-Soft Acid-Base classification of metal ions and ligands

Metals, Ions, Molecules				**Ligands**
HARD				HARD
H^+, Na^+, K^+	Mg^{2+}, Ca^{2+}, Mn^{2+}, VO^{2+}	Al^{3+},Co^{3+}, Cr^{3+}, ga^{3+}, Fe^{3+}, Tl^{3+}, Ln^{3+}, MoO_3^+	SO_3, CO_2	Oxygen ligands in H_2O, CO_3^{2-}, NO_3^-, PO_4^{3-} $ROPO_3^{2-}$, $(RO)_2PO^{3-}$, CH_3COO^- OH^-, RO^-, R_2O, and crown ethers Nitrogen ligands in NH_3, N_2H_4, RNH_2, Cl^-
INTERMEDIATE				INTERMEDIATE
Fe^{2+}, Ni^{2+}, Zn^{2+}, Co^{2+}, Cu^{2+}, Pb^{2+}, Sn^{2+}, Ru^{2+}, Au^{3+}, SO^2, NO^+				Br^-, SO_3^{2-}, nitrogen ligands in NO_2^-, N_3^-, N_2 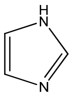 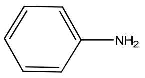
SOFT				SOFT
Cu^+, Au^+, Tl^+, Ag^+, Hg_2^{2+}	Pt^{2+}, Pb^{2+}, Hg^{2+}, Cd^{2+}, Pd^{2+}	Pt^{4+}		Sulfur ligands in RSH, RS-, R_2S, R_3P, RNC, CN-, CO,R^-, H^-, I^-, $S_2O_3^{2-}$, $(RS)_2PO_2^-$, $(RO)_2P(O)S^-$

1.3.2. Ligands

To what concerns the linker itself, there are essentially two possibilities: exogenous or endogenous linkers. The most common is the use of exogenous linkers, synthetic or obtained from natural compounds which do not participate in any of the body metabolic cycles. Some of the more relevant exogenous MOFs for bioapplications are CPO-27(Mg) [55], MIL100(Fe) [56] and BioMOF1 [57]. Pore size for these solids range from 4-29 Å, with BET surface areas ranging from 1200 to 2200 $m^2.g^{-1}$, and in some cases present accessible Lewis acid sites where biomolecules (NO, CO, H_2S, drugs, etc) can coordinate strongly for a better control of the release [58] [59] [60].

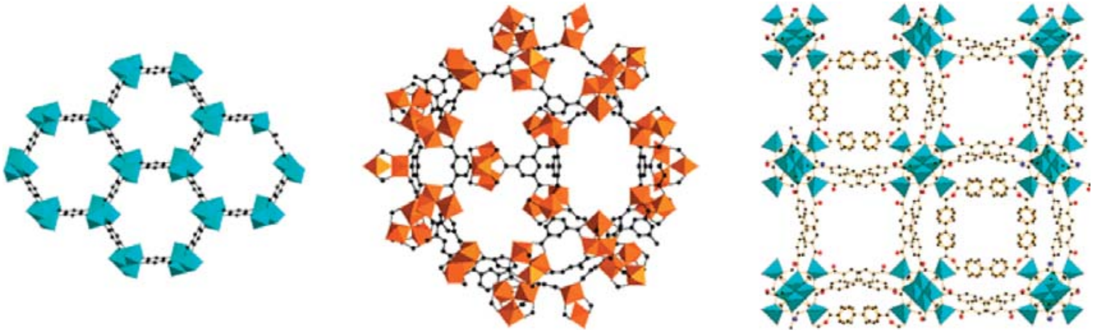
(a) (b) (c)

Figure 4| Structural view of a few topical MOFs integrating exogenous linkers for bioapplications, (a) CPO-27(Mg,Zn) [55], (b) MIL100(Fe) [56] and (c) Bio-MOF1 [57] (adapted from [32])

One important feature for exogenous linkers in order to avoid associated toxicity is the possibility of its body excretion after *in vivo* administration of the MOF. Data from toxicity of a few organic linkers is available (LD50) and generally indicate that typical polycarboxylic or imidazole linkers are not very toxic (Table 4), maybe because of their high polarity and easy removal under physiological conditions [32].

Table 4| Oral LD50 (rats) for selected organic linker (adapted from [32])

Ligand	LD50 (g/kg)
Terephthalic acid	1.13
Trimesic 2,6 naphtalenedicarboxylic acid	5.5
1-methylimidazole	8.4

Funtionalization of the exogenous linkers can also improve pharmacokinetics of MOFs, tuning their absorption - distribution – metabolism – excretion (ADME) [32]. Additionally, the presence of functional groups within the framework can modulate the host – guest interaction allowing a better control of release [32]. It is though important to note that the addition of a functional group to a MOF will, besides affecting host – guest interaction, alter its flexibility during adsorption and delivery of the biomolecule [37].

The alternative use of endogenous organic linkers is a breakthrough regarding biocompatibility of MOFs once the spacer can be reused once administered, what reduces the risk of adverse effects. It is possible to find a significant number of reports on MOFs based on endogenous linkers [61, 62]. Examples are the iron (III) gallate, fumarate or muconate MOFs that exhibit either rigid small porous structure or a flexible porous matrix. [63-65]. Also, reports on porous amino acid [30] and more recently peptide [2, 3, 31] based MOFs has been reported. These type of MOFs are structurally and functionally similar to other MOFs [66], though peptides, for their structural diversity, conformational flexibility and intrinsic chirality promise to reveal properties such as gated adsorption and chiral recognition [31].

1.4. Drug Delivery With MOFs

The development of nanotechnologies applied to drug delivery has allowed specific targeting of tissues, cells and even subcellular structures [67, 68]. Lipids and polymers have been, until present, the most studied drug nanocarriers [69, 70]. The therapeutic advantages reached through the use of drug nannocarriers have permited the clinical use of the first nanodrugs (Doxil®, Abraxane®, and Ambisome®), though there are still many potent drugs lacking efficient nanotransport, mainly because of the low drug loadings (< 5 wt %) achieved, the present of burst release, poor biological barrier bypass and/or associated toxicity [32].

Inorganic or hybrid porous materials offer a potential alternative to organic nanocarriers. The high and regular porosity associated to important pore volumes and surface areas can lead to major improvements in drug loading capacities and ability to control drug release [32].

The first evidence of the high potential of porous MOFs for drug loading was given by Horcajada *et al.* by using a model drug, the anti-inflamatory and analgesic ibuprofen and the model mesoporous rigid chromium carboxylates MOFs (MIL-100(Cr) [71] and MIL-101(Cr) [9]). These MOFs were chosen despite the toxicity associated with chromium, because of their mesoporosity (cages of Ø ≈ 25-34 Å) accessible from microporous windows (Ø ≈ 5-16 Å) to permit the drug access, large pore volumes up to 2 $cm^3.g^{-1}$ and specific surface areas within the 2100-4400 $m^2.g^{-1}$ range (BET values), to ensure efficient drug loadings, and water stability, to avoids rapid degradation phenomena and drug release [32].

Ibuprofen was encapsulated into the porous MOFs with exceptional efficiency by a simple impregnation process. High drug loadings up to 1.4 g of ibuprofen per gram of MIL-101(Cr), have been achieved, corresponding to ~56 ibuprofen molecules for each smaller cage and ~92 molecules in the larger cage. The much lower capacity of MIL-100(Cr) (0,35 g/g) in comparison with MIL-101(Cr) (1.38 g/g) is attributed to the non accessibility of Ibuprofen molecules (~10 x 5 Å) to the smaller mesoporous cages, which are accessible only through narrow pentagonal windows (~5 Å) [32].

More recently other classes of MOFs were tested for their capacity of drug loading, namely MIL-53(Cr,Fe), which are able to reversibly modulate their pore size upon the application of an external stimuli (*e.g.* drug molecules [38]).

Both these rigid and flexible porous metal carboxylate MOFs have also shown an important progressive release of Ibuprofen under biological simulated conditions (Simulated Body Fluid (SBF), pH 7.4, 37 °C). Drug cargo showed to be fully released from MIL-100(Fe, Cr), MIL-101(Cr), and MIL-53(Fe, Cr) within 3, 6, or 21 days respectively. Release mechanism of ibuprofen was admitted to be governed by diffusion processes combined with drug-matrix interactions [32].

An *et al.* reported the encapsulation of the cationic antiarrythmic drug, procainamide, into the mono-dimensional pore system of the anionic zinc adeninate framework $Zn_8(adeninate)_4(biphenyldicarboxylate)_6O_2Me_2NH_2$. 8DMF.11$H_2O$ (Figure 5a), named BioMOF-1 [57].

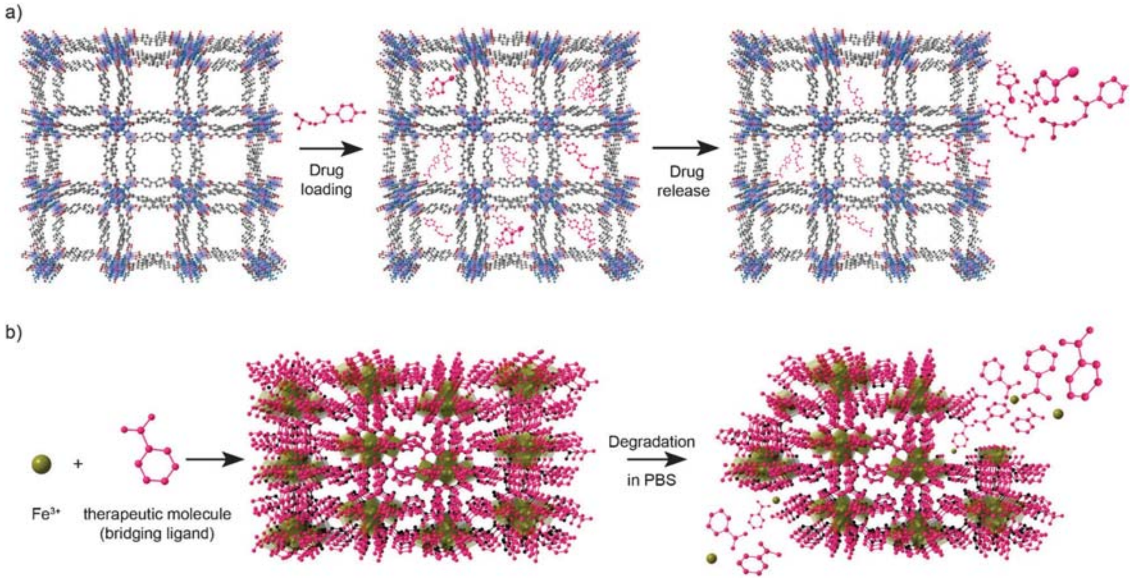

Figure 5| Ilustration showing two possible approaches to use MOFs as therapeutic carriers. (a) The use of MOFs for encapsulating and further releasing therapeutic species. (b) The use of therapeutic species as bridging organic ligands to build up the MOF; the therapeutic species are released as the MOF degrades (adapted from [72])

Also recently other different drugs, namely the antitumoral busulfan (Bu) and doxorubicin (Doxo), the antiviral azidothimidine triphosphate (AZT-Tp) and cidofovir (CDV) [73], and the etoxysuccinato-cisplatin [74], have been used to test MOFs efficiency on loading and control release under biological conditions (Table 5). The controlled release is of major importance, once due to its short *in vivo* half-life it is necessary to administer this compound every 3-4 h, making very interesting the possibility of a controlled release of this drug.

Table 5| Drug loading capacities of different drugs on several porous MOFs (adapted from [32])

	Drug loading (wt %)			
Drug	**BioMOF-1**	**MIL-100**	**Mil-101_NH$_2$**	**MIL-53**
Etoxysuccinato-cisplatin			12.8	
Procainamide	2.2			
Busulfan		25.5		14.3
Azidothimidine triphosphate (AZT-Tp)		21.2	42.0	0.24
Azidotimidine		6.1		
Cidofovir		16.1	41.9	
Doxorubicin		9.1		
Ibuprofen		33		22
Caffeine		24.2		23.1
Urea		69.2		63.5
Benzophenone 4		15.2		5
Benzophenone 3		1.5		

1.5. Amino Acid Based Metal Organic Frameworks

With the general formula NH_2CHRCO_2H – where NH_2 and CO_2H are the amino and carboxylic acid terminal groups, respectively, and R represents the side chain – α-amino acids (AA) are highly functional small molecules whose side chain groups are like prototypes of metal coordination and weak interactions in proteins [75]. AA link together via amide bonds to form peptides and proteins to perform essential biological functions [76].

AAs are excellent organic ligands and have shown to be able to coordinate to metal ions by both their carboxylate and amino groups. In nature, chelates of AAs and metals are common, having important biological functions as transporters of metal ions through blood [75]. This behavior is based on covalent or weak interactions of both N and C terminal, and the side chain groups of amino acids, such as the charged groups of arginine and aspartic acid and the aromatic rings of tyrosine and tryptophan, in metal complexes, in solution and in the solid state [75].

It is possible to differentiate tree major types of AA based MOFs, either constructed from metal ions and natural AA; metal ions, natural AAs and additional bridging anions and polydentate organic ligands; or metal ions and chemically-modified natural AAs (*e.g.* with additional metal binding groups) [72].

All natural AAs are formed by a α-carbon atom bonded to an amino and a α-carboxylic group. These metal groups allow the formation of AAs discrete complexes through the formation of the typical five-membered glycinate chelate ring (O, N-chelating mode) [72]. Notably, the α-carboxylate group can coordinate metal ions in bi- or tridentate bridging modes (Figure 6). This occurrence can lead to the formation of extended metal ion-AA frameworks [72].

Coordination networks based on pure aminoacids can present 1D [77], 2D or 3D extended structures [78-83]. 2D metal ion-AA frameworks have been obtained when glycine (Gly) coordinates to metal ions as Ni(II) [78], Mn(II) [84], Co(II) [79] and Fe(II) [85] in a stoichiometry of 2 moles of AA to 1 mole of metal. Typically, these 2D structures involve the interaction of one metal ion with an octahedral geometry to other four metal ions bridged by four Gly ligands adapting a μ-O1:O2 coordination mode [72] (Figure 6).

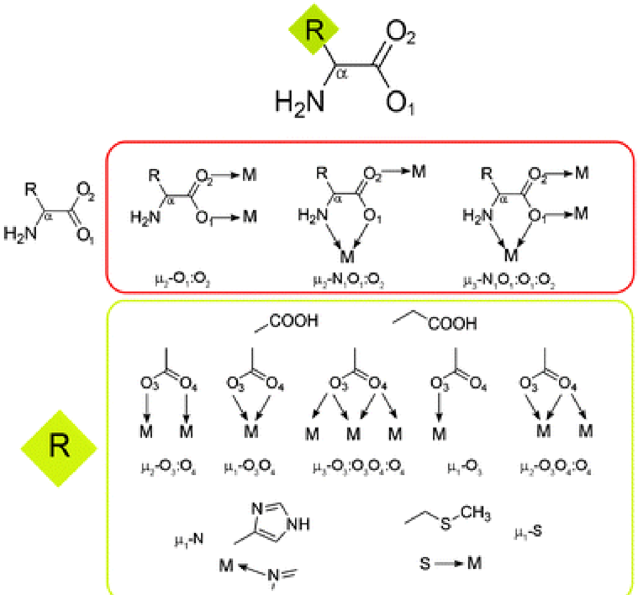

Figure 6| Typical structure of a natural AA (top) and the potential coordination modes that this structure can adopt *via* their backbone (middle) or side chains (bottom). Top side chains correspond to Asp and Glu, and bottom ones to His and Met (adapted from [72]).

Coordination can also result in a 2D framework when two AA ligands connect to an octahedral metal ion in the typical O,N-chelating mode. This mode leads to additional bridging to neighboring metal ions through the second oxygen atom of the AA carboxylate group (μ-N1O1:O2 coordination mode) (Figure 6) [72]. These type of 2D structures have been obtained by combining L-phenylalanine (Phe) with Mn(II) [86] and Cu(II) [87], L-tryptophan (Trp) with Mn(II) [80] and Ni(II) [81], and L-glutamine (Gln) with Cu(II) [82].

Although reports on 3D metal ion-AA frameworks are to present still scarce, there are some AAs with metal binding groups on their side chains, such as the β-carboxylate group of Asp and Glu, the imidazole group of histidine (His), the thiol or thioether groups of cysteine (Cys) and methionine (Met) respectively, and the phenol ring of tyrosine (Tyr). These groups, that serve as metal binding sites in proteins, can be used to bridge metal ions together forming dimensionally higher metal ion-AA networks [72] (Figure 6).

A representative example of one of these 3D AA derived MOFs, is the homochiral complex of Zn (II) and Asp [Zn(Asp)].H_2O [30] (Figure 7).

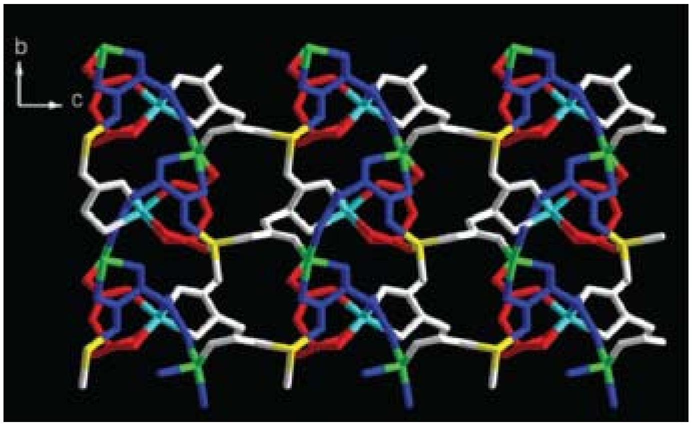

Figure 7| 3D network between Zn(II) and Asp (adapted from[30])

The framework comprehends multiple coordination geometries of zinc, which are distorted, multiple binding modes of Asp to zinc, and three conformations of the ligand within the structure [30] (Figure 8).

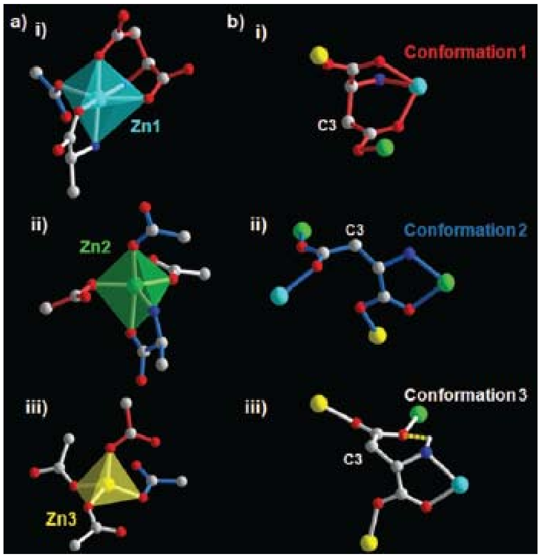

Figure 8| Three distorted coordination geometries of Zn (adapted from[30])

Bridging of 4-, 5-, and 6-coordinated Zn(II) ions through Asp ligands via (μ2-N1O1:O2 and μ2-N1O3:O4 modes results in the formation of a 3D framework with cavities of 33 $Å^3$ and a total solvent accessible volume of 7.3%. Surprisingly the structure seems to rearrange itself after H_2O guest molecules used as solvent, leave at 350 °C.

Other interesting coordinated metal ion-AA have been described (Figure 9), as the [Cu(L-Asp)(Im)].2H_2O, (Im = Imidazole) reported by Pellacanni *et al.* [88].

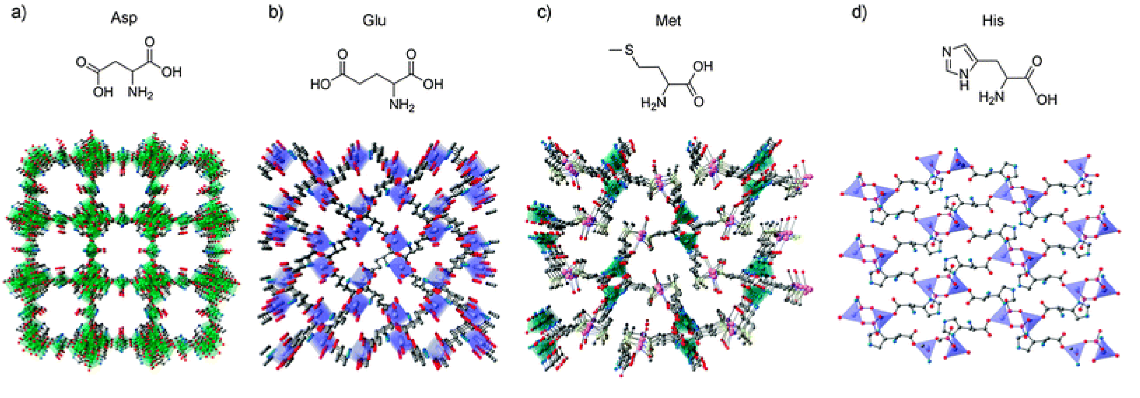

Figure 9| Metal–AA frameworks 3D projection along with their AA components of (a) [$Ni_{2.5}$(OH)(L-Asp)$_2$]·6.55H_2O, (b) Zn(L-Glu)(H_2O)]·H_2O, (c) [Ag_3Cu_3(L-Met)·6(NO_3)$_3$(H_2O)$_3$]·7H_2O and (d) Zn(HPO_3)(His)(H_2O)$_{1/2}$ (adapted from [72])

Also Glu has been used to create a series of nearly isostructural 3D MOFs, formulated as [M(L- or D-Glu)(H_2O)].H_2O (where M represents Cd(II) [89], Zn(II) [90], Cu(II) [91] or Co(II) [92]). In all these frameworks, Glu ligands serve as multidentate ligands to coordinate to three different metal ions in μ2-N1O1:O2, μ1-O3:O4 and μ2-O2:O4 modes, where each octahedral metal ion is coordinated with three Glu ligands (Figure 9).

Finally, for the specific interest of this project, it becomes mandatory to explore the possibility of formation of metal ion-Argine (Arg) complexes. The guanidinium group of L-arginine (L-Arg) in some enzymes is an important binding site for various hydrogen bond acceptors such as carboxylate , superoxide , and phosphate groups, and is recently attracting much attention as the recognition site for the guanine base in DNA–Zn finger interactions [93].

Ohata group [93-95] revealed the striking architecture of self-organized systems based on molecular recognition, formed by two programmed components, $[Cu(Arg)_2]^{2+}$ and a dicarboxylate ion (*e.g.* L2- = o-,m-, or p-phthalate (pa)) [94]. In these structures, the Arg side chains are extended outward, and one guanidinium group is hydrogen bonded to the carboxylate group of a neighboring L2-, and the other is to the carboxylate group from another neighboring L2-, forming a double helical structure [94, 95] (Figure 10).

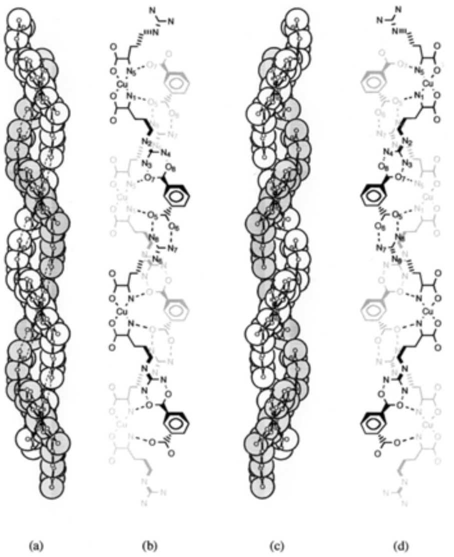

Figure 10| (a-d) View of $[Cu(D\text{-}Arg)_2](m\text{-}pa)\cdot 6H_2O$ (1D) showing an infinite left-handed double-helical chain. The chains run along the *a* axis (adapted from [95])

1.6. Peptide Based Metal Organic Frameworks

Peptides are biopolymers composed of AAs linked by peptide bonds. Each peptide has a distinctive conformation, which depends of the sequence and stereochemical configuration of their constituent AAs. Peptide chemistry offers a virtually unlimited structural diversity, including additional metal coordinating sites [31]. Peptides have specific recognition properties and possess intrinsic chirality, what makes them prime candidates for the synthesis of chiral MOFs [31].

Peptides always have an amino and a carboxylic acid terminus, both groups with capacity of coordinating metal ions in different coordination modes [72]. Coordination of the terminal amino group to metal ions, usually occurs in a monodentate or chelating mode, where the oxygen atom of the neighboring amide group also coordinates to the same metal ion forming a five-membered chelate ring [72] (Figure 11). Peptides can also adopt a O, N-chelating mode similar to that observed for AAs [72] (Figure 6). Through their carboxylate terminal group, peptides can coordinate to metal-ions in any one of the coordination modes of carboxylic acids (Figure 6). To take advantage of an increased number of metal binding groups it is possible to synthesize peptides made from constituents such as Asp and Glu.

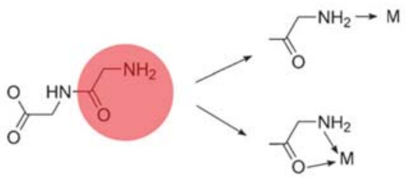

Figure 11| Potential coordination modes for the terminal amino group of peptides (adapted from [72])

The dipeptide glycylglycine (GlyGly) constitutes the simplest peptide and can illustrate the ability of AA of acting as bridging ligands [72]. Takayama *et al.* first synthesized tree metal-peptide frameworks by adjusting the pH of aqueous solutions containing Zn(II) or Cd(II) metal salts and GlyGly [96]. These authors obtained a 2D framework of [M(GlyGly)$_2$].2H$_2$O (M is Zn(II) or Cd(II)) at pH 6. In these MOFs each octahedral metal ion is connected to other four metal ions through four bridging GlyGly ligands. Coordination is accomplished by a GlyGly bridge between two metal ions through the terminal carboxylate group in a monodentante mode and through the terminal amino group by forming a five membered chelate ring. Interestingly, when pH was set to 9 a novel 2D MOF with formula [Cd(GlyGly)$_2$].H_2O was formed. In these frameworks the carboxylate groups of GlyGly bind to two Cd(II) ions while their amino groups bind to another Cd(II) ion in a monodentate mode. Consequently, each Cd(II) ion is linked to six other Cd(II) ions by four GlyGly ligands.

Later on other peptide based frameworks made from dipeptides have been reported [2, 3, 97]. Examples include the [Zn(GlyThr)$_2$].2H_2O [98], [Cd(AlaThr)$_2$].4H_2O [2], [Cd(AlaAla)$_2$] [2] and [Zn(GlyAla)$_2$].solvent [3], all consisting of metal-peptide sheets connected through strong hydrogen bonds. The type of connectivity exhibited by these peptides is similar to that observed for [M(GlyGly)$_2$].2H_2O [96], where each metal ion is connected to four other metal ions through four dipeptide ligands. These structures differ on the coordination spheres of their metal ions (number and configuration) and/or the metal-peptide coordination modes, leading to the formation of pores of different topologies.

Probably the most interesting of the peptide based MOF is [Zn(GlyAla)$_2$].solvent synthetized by Rosseinsky *et al.* [3]. In this MOF, the zinc ion are coordinate tetrahedrally to four peptide ligands, where two peptide ligands are coordinated by the C-terminal Ala carboxylate groups and two by N-terminal Gly amine groups, both in a monodentate mode [3]. A grid-like structure is reveled formed by the coordination of each ligand to two Zn(II) ions (Figure 12a). The layers are aligned in a A-A mode in the third dimension by hydrogen bonds between all the amide groups in adjacent layers, originating square shaped, 1D pores with an accessible volume of 532.1 Å^3 per unit cell at 100 K (28%) (Figure 12b). One remarkable property of this MOF, result from its adaptable porosity, is the reversibility of the structural changes undergone after desorption/reabsorption of solvent molecules [3].

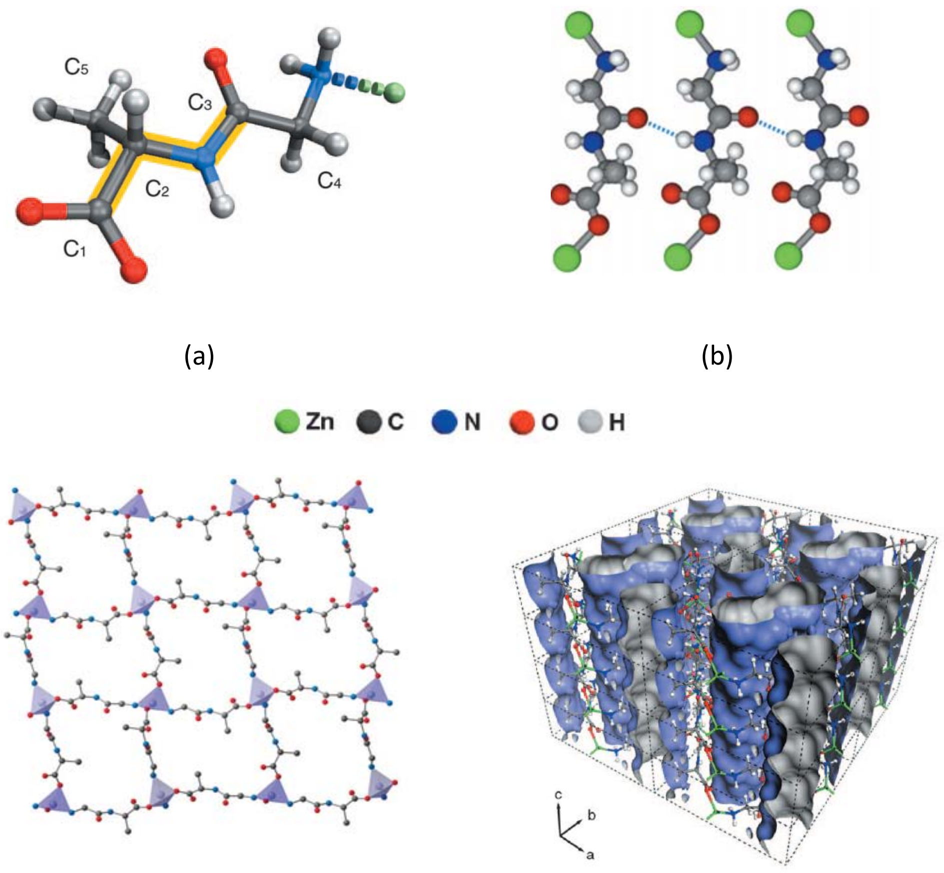

(a) (b)

(c) (d)

Figure 12| (a) The GlyAla dipeptide ligand, representation of the stacking of the layers by alignment of hydrogen bonds and the walls of the channels, (c) one layer of [Zn(GlyAla)$_2$], (d) perspective view of the channels (adapted from [3]).

It becomes clear that variations in the AA sequence results in different metal-peptide structures, and that versatility offers an unlimited number of functionally tunable 2D and 3D metal-peptide frameworks. Gasque *et al.* synthesized two MOFs made by connecting Pb(II) or Cd(II) ions through GlyGlu ligands [99]. The first has a 2D metal-peptide framework, where both carboxylte groups from Glu residue coordinate to four Pb(II) ions in a tridentate mode. The second 3D porous [Cd(GlyGlu)$_2$].3H$_2$O, has 1D channels and is formed by octahedral Cd(II) ions linked in three dimensions to four other Cd(II) ions by four GlyGlu ligands (Figure 13). In this case, the amino groups do not participate in the coordination of Cd(II) ions, and only the carboxylate groups of the Glu residue bind to Cd(II) ions in a bidentate mode. Thus the simple addition of metal-binding sites to the peptide allows the formation of 3D metal-peptide frameworks [72].

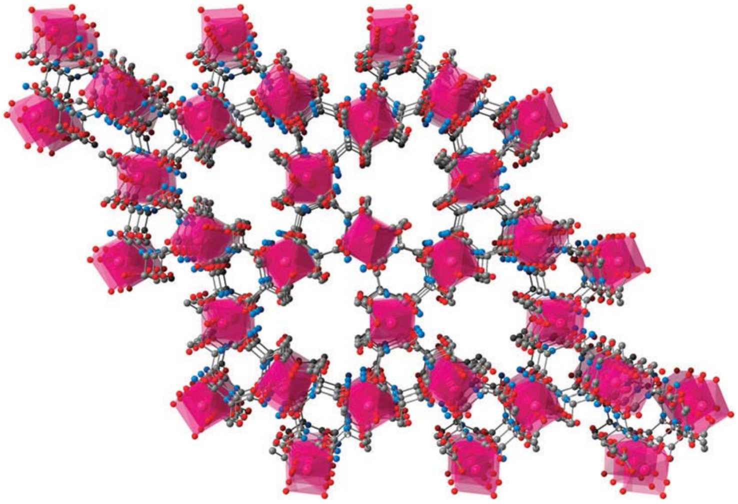

Figure 13| **The porous structure of [Cd(GlyGlu)$_2$] (adapted from [72])**

1.6.1. Tripeptide Ligands

The number of publications reporting MOFs constructed of more than two peptides is scarce but two major works can be pointed. Lee *et al.* have published in 2008 two tripeptide based structures of Cd(Gly$_3$)$_2$.H$_2$O and Cd(L-Ala$_3$)$_2$ [2]. In that same year Mantion *et al.* reclaimed the first report on a peptide based MOF, what they have coined as Metal Peptide Framework (MPF), constructed from a previously prepared oligovaline peptide [31]. The simple oligopeptide, Z-(L-Val)$_2$-L-Glu(OH)-OH, was efficiently used to grow porous copper (MPF-2) and calcium (MPF-9) frameworks (Figure 14), under mild synthetic conditions, without the need of autoclave, microwave, or slow diffusion protocols [31]. This porous networks, which are stable up to ~250 °C, formed due to metal-oxygen and metal-nitrogen bonding and various types of hydrogen bonding along with the π-π staking [31].

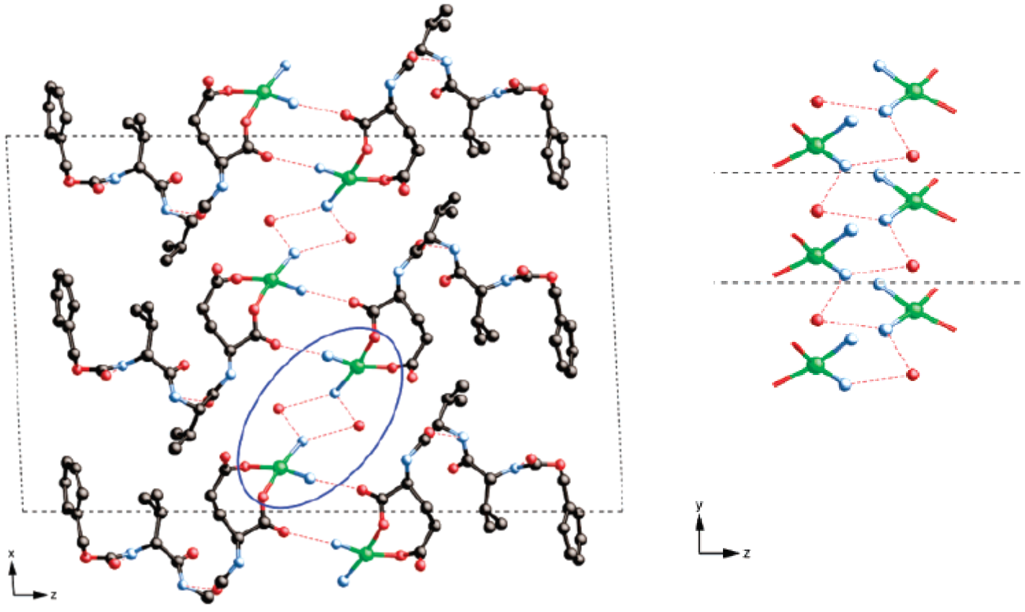

(a) (b)

Figure 14| View of the crystal structure of MPF-9. Hydrogen bonding network in the *ac* plane showing H-bonds between ammonia and the L-Glu acid residue (a), and in detail water molecule hydrogen bonds with ammonia molecules of neighboring Cu complexes (b) (adapted from [31]).

Lee *et al.* prepared a Cd(Gly$_3$)2.H$_2$O structure, which is analogous to that of GlyGly dipeptide complex, where each Cd(II) ion is octahedrally ligated by six peptides: the N-terminal group of two peptides supply two apical nitrogen ligands, and one oxygen from each of the four C-terminal carboxylates supply four equatorial ligands [2] (Figure 15). Each carboxylate group bridges two Cd ions to form chains of eight membered rings that extend the framework in one dimension [2]. The second dimension of the framework is formed by the peptide backbone where two triglycine peptides adopt a antiparallel orientation to each other, forming a ring that is close by ligation to two Cd(II) ions [2].

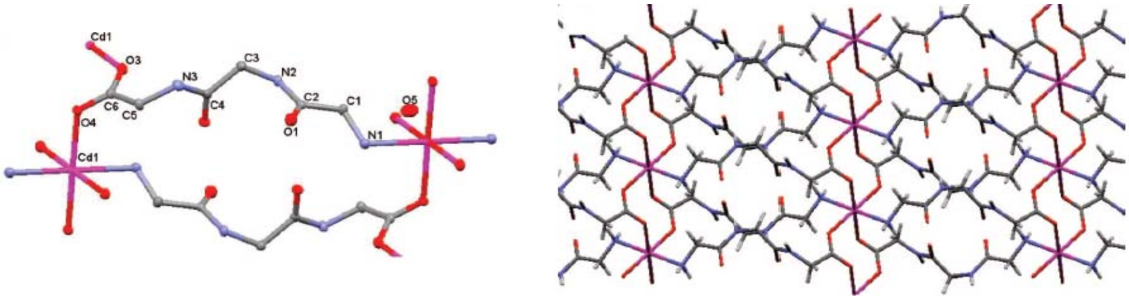

(a) (b)

Figure 15| (a) Structure of Cd(Gly_3)$_2$·H_2O,. (b) View along the crystallographic c axis, clearly showing the 8-membered rings formed by Cd-bridging carboxylate groups, similar to (adapted from [2])

The structure (Cd(L-Ala_3)$_2$) allowed to study the influence of chirallity, by addition of the simple methyl group of alanine, in the resulting structure of the metal-peptide framework [2]. The complex forms a one dimensional extended molecular chain where infinite series of rings are linked together through the Cd(II) ions (Figure 16). Each Cd(II) is octahedrally coordinated by four trialanine peptides, once the steric hidrance from the side chains methyl groups prevents the carboxylate group from bridging between Cd(II) ions [2]. Carboxylate groups from two peptides coordinate each Cd(II) in a monodentate fashion while the N-terminal of the other two peptides supply two nitrogen ligands, and the N-terminal amide carbonyl oxygens provide the final two ligands to the metal [2].

Other interesting characteristics of this complex is the antiparallel orientation of the ligands, forming a ring, similar to Cd(Gly_3)$_2$.H_2O, and the peptide folding around the methyl group of the N-terminal Ala residue, so that it points into the center of the ring [2]. Together with the opposite tripeptide side chain, the two methyl groups form a hydrophobic core that fills the central cavity of the ring [2] (Figure 16b). Methyl groups from second and third residues face outward and make hydrophobic contact with methyl groups from adjacent metal-peptide chains, propagating the structure in the second dimension [2] (Figure 16c). Hydrogen bonding interactions between amide N-H and carbonyl oxygens extend the structure in the third dimension [2].

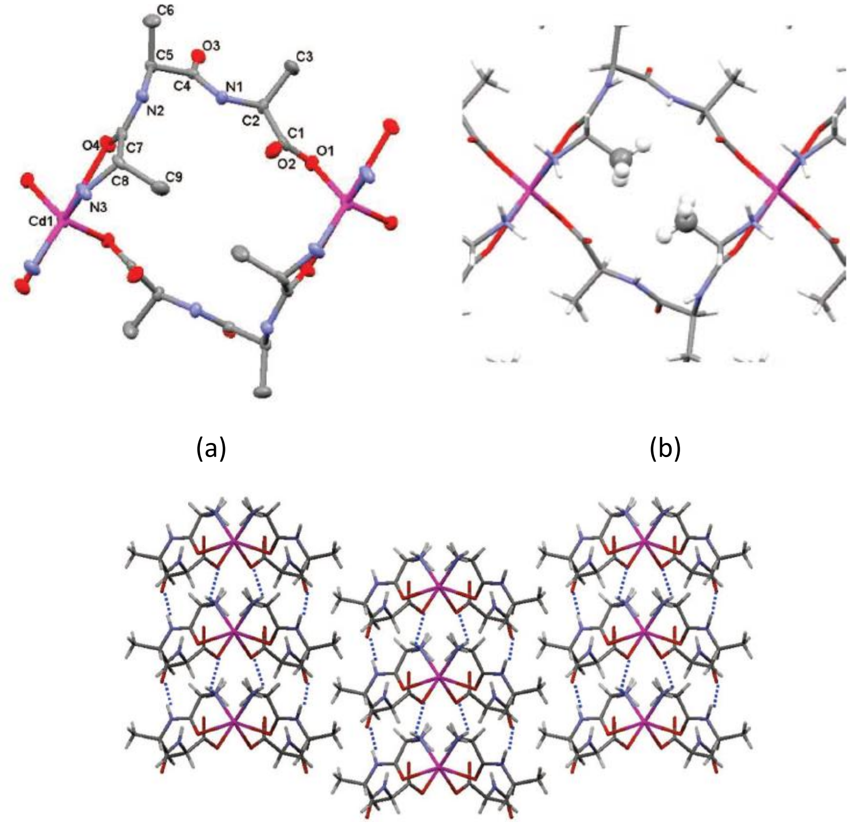

(a) (b)

(c)

Figure 16| (a,b) Structure of $Cd(Ala_3)_2$, packing of the two methyl groups within the center of each ring to form a hydrophobic core, (c) view along the crystallographic *c* axis illustrating the packing of chains within the crystal mediated by interdigitation of the alanine methyl groups and the hydrogen bonding between amide groups (adapted from [2])

1.7. High-Dimensional Metal Organic Frameworks

In contrast to the binding preferences of metal ions, the nature of organic ligands including the type, number, and the position of the binding group, the electronic structure, as well as the steric tension of the ligand skeleton may play important roles on the overall framework connectivity and physical/chemical performance [100]. Intermolecular weak interactions such as hydrogen bonding and π-π stacking can also help to tailor the higher-dimensional networks of the resulting target complexes [100].

Synthesis of new highly connected MOFs with polynuclear metal clusters as secondary building units (SBUs) or with higher-order stranded helical structures have found a great deal of interest due to their intriguing structural diversities and potential applications as functional materials [101].

SBUs are molecular complexes and cluster entities in which ligand coordination modes and metal coordination environments can be utilized in the transformation of these fragments into extended porous networks using polytopic linkers [13]. SBUs usually not only have predefined and rigid coordination geometries, but also are generated in situ, which often provide a versatile pool of connectors for the rational synthesis of MOFs [102] Eddaoudi *et al.* [8] have found that multidentate linkers such as carboxylates allow the formation of more rigid frameworks due to their ability to aggregate metal ions into M-O-C clusters SBUs. The SBUs are sufficiently rigid because the metal ions are locked into their positions by the carboxylates; thus instead of having one metal ion at a network vertex, SBUs serve as large rigid vertices that can be joined by rigid (e.g. teraphtalic acid) [101] or flexible (adipic acid and glutaric acid) [101] organic links to produce extended frameworks of high structural stability [8].

One of the most famous SBUs is the dimetal tetracarboxylate square paddle-wheel cluster that often acts as the planar 4-connected node [102]. In most cases, two metal atoms are bridged by four carboxylates to give this SBU [102]. Examples of these SBUs are the [$Cu_2(OCO)_4$] [8], the [Zn(BDC)(H_2O).(DMF)] (BDC = 1,4 benzenedicarboxylate) [8] and the particularly interesting for its nucleobase incorporation, the new cadmium-adeninate "paddle-wheel" [$Cd_2(Ad)_2(IN)_2(DMF).H_2O$].DMF (IN = isonicotinic acid) [102] (Figure 17).

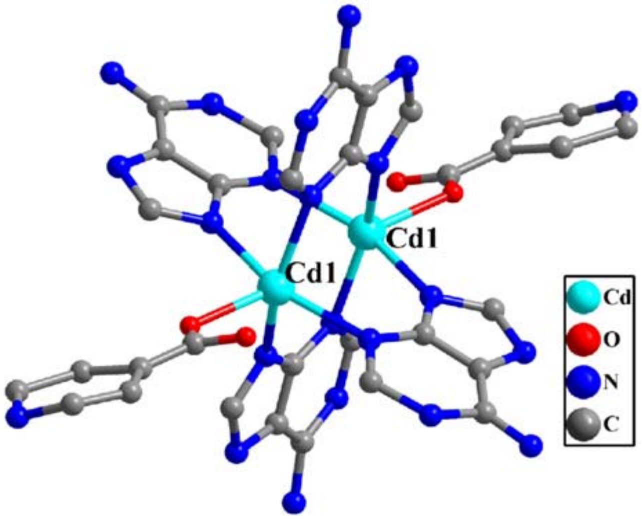

Figure 17| The cadmium(II)-adenine paddle-wheel subunit (adapted from [102])

1.7.1. Nucleobase-based metal complexes

Nucleobases are key constituents of nucleic acids as DNA and RNA and are involved in base pairing [76]. Nucleobases have accessible nitrogen and oxygen electron lone pairs, which allows these molecules to act as multidentate organic ligands [103]. As one of the native nucleobases, adenine (AdeH), a purine nucleobase, can undergo a variety of acid-base reactions and exists as surprising tautomers, which thus offer the possibility of coordination as neutral and also as both anionic and cationic ligands [104]. Adenine is ideal for constructing MOFs due to (1) its imidazole ring that mimic the imidazole derivatives, (2) its rigidity, which helps enable the preparation of permanent porous materials , (3) and as a result from its three kinetically favored endocyclic sites (N1, N3, and N7) and potential H-bonding site (N6), AdeH can potentially exhibit versatile binding modes upon coordination with metal ions [104]. Theoretically, the N3, N9 atoms in adenine ligand can mimic a carboxylate group to form the metal adeninate “paddle-wheel” subunit [102].

1.7.2. Flexible coligands

The rigid structures provided by the assembly of SBUs based on Cd(II)-adenine, produce porous structures [102] that can be decorated with flexible coligands (adipic acid, glutaric acid) allowing the expansion of links between vertices [101, 104]. A representative example of these high-dimensional complexes is given by the synthesis of a 2D trinuclear Cd(II)-complex with adenine nucleobase by Yang *et al.* [104]. By the assembly of flexible adipic acid (H_2ap), adeH nucleobase and Cd(II) salts under hydrothermal conditions, the authors successfully isolated a infinite 2D Cd(II) aggregate ($([Cd_3(\mu3\text{-ade})_2\text{-}(ap)_2(H_2O)_2].1.5H_2O)_n$, with trinuclear Cd(II) as secondary building units [104] (Figure 18).

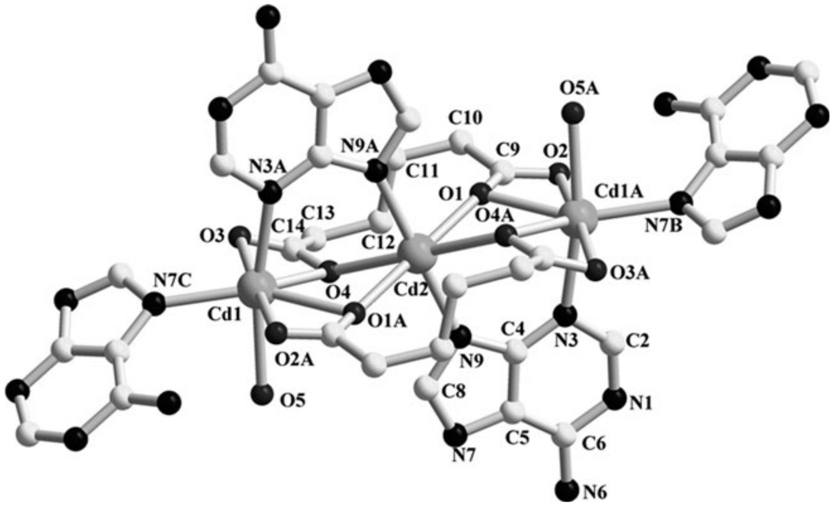

Figure 18| View of the trinuclear Cd(II)-subunit (adapted from [104])

Crystal structure determination revealed that the basic building block of trinuclear Cd(II) contains three Cd(II) ions, two AP anions, two bridging Ade, two coordinated water molecules (O5 and O5A) and two free lattice water molecules with 50% occupancy number for O6 and 25% for O7. Cd2, located at an inversion center of the trinuclear subunit, exhibits a distorted octahedral geometry formed by four carboxylate oxygen atoms from two ap anions and two ade imidazole nitrogen atoms (N9 and N9A), resulting in a CdN_2O_4 donor set [104].

1.8. Integrin αVβ3 and RGD Peptide

Targeted delivery of therapeutics and diagnostics to tumour vasculature constitutes a potential approach for treatment of cancer, since the process of formation of new blood vessels that feed the tumor mass, known as angiogenesis is essential for tumour growth and endothelial cells are genetically more stable and therefore less prone to develop resistance [6]. Because they are in direct contact with the blood stream, these cells are easily accessible for targeting conjugates. The restricted expression profile observed for αVβ3-integrin, which is expressed on angiogenic but not on resting endothelial cells, makes it an ideal target [6]. Taking advantage of this characteristic for targeting and imaging, αVβ3-integrin specific ligand motif Arg-Gly-Asp (RGD), has been introduced into proteins, polymers, lipossomes, virus and other gene delivery vehicles (Figure 19).

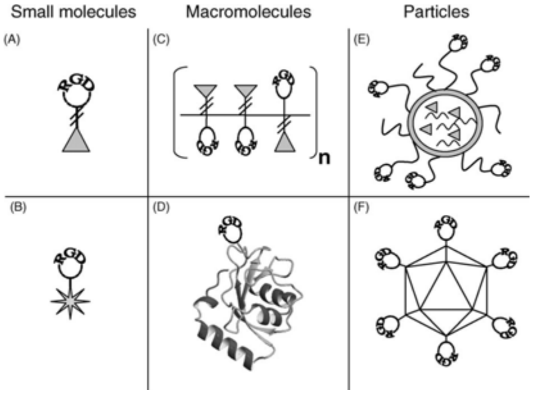

Figure 19| Schematic representation of RGD-mediated drug delivery and imaging constructs (adapted from [6]).

1.9. Integrin Biology

1.9.1. The integrin family of cell adhesion receptors

Integrins are heterodimeric cell surface receptors that mediate adhesion to the Extra Cellular Matrix (ECM) and immunoglobulin superfamily molecules. Each subunit crosses the membrane once, with most of each polypeptide (> 1600 amino acids in total) in the extracellular space and two short cytoplasmic domains (20–50 amino acids).

At least 24 distinct integrins can form by the association of the 18 α and 8 β subunits [105] (Figure 20). The variety of integrin heterodimers allows the preferential binding to distinct ECM proteins. The set of integrins present on a given cell dictates the extend to which that cell will adhere to and migrate on different matrices [105]. αV integrins recognize the RGD sequence on their respective ligands (*e.g.* fibronectin, vitronectin), and were in fact identified on the basis of their ability to recognize the RGD sequence [106].

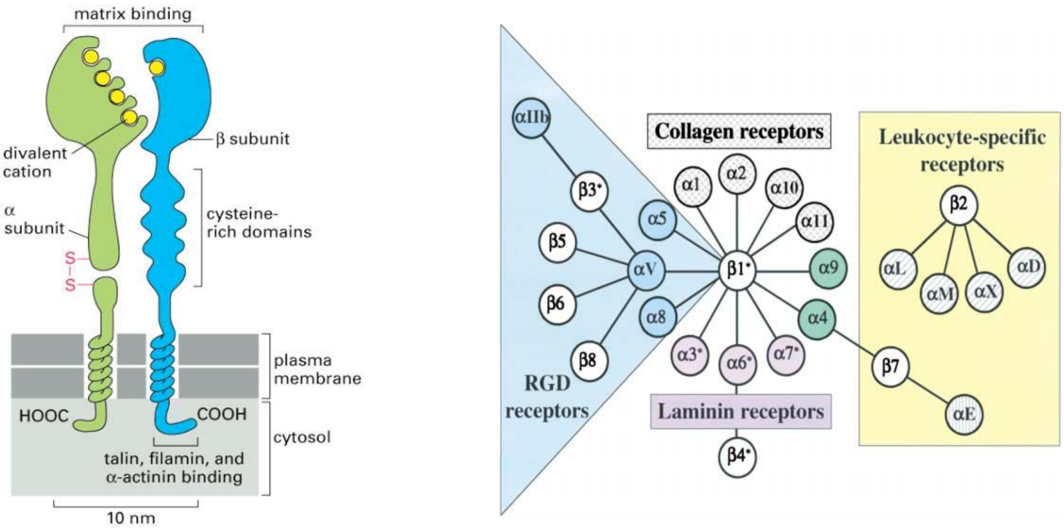

(a) (b)

Figure 20| (a) General structure of integrins where extension of extracellular and cytoplasmatic domains can be compared (adapted from [107]) , (b) the Integrin receptor family (adapted from [105])

Integrin subunits span the plasma membrane and in general have short cytoplasmic domains of ~40-70 amino acids. Outside the cell plasma membrane, the α and β chains lie close together along a length of about 23 nm and the final 5 nm N-termini of each chain forms a ligand binding region for the ECM [107].

An integrin is 280 Å long and consists of one α (150 to 180 kD) and one β (90 kD) subunit, both of which are type I membrane proteins. β subunits have four cysteine-rich repeated sequences [108].

Integrins can be categorized in various ways. For example, the presence of an additional domain inserted toward the N-terminal of the α chains, the alpha A domain (so called because it has a similar structure to the A-domains found in the protein von Willebrand factor; also termed α-I domain), identifies a subset of integrins. Integrins carrying this domain either bind to collagens, or act as cell-cell adhesion molecules [105]. This α-A domain is the binding site for ligands of such integrins [105]. Those integrins not carrying this inserted domain, still have an A-domain in their ligand binding site, but this A-domain is found on the β subunit [105].

A central feature of integrin interaction with physiologic ligands is the monodentate binding of a ligand carboxylate to a Mg^{2+} ion hexacoordinated at the metal ion-dependent adhesion site (MIDAS) in the integrin A domain. This interaction stabilizes the A domain in the high-affinity state, which is distinguished from the default low-affinity state by tertiary changes in the domain that culminate in cell adhesion [109].

The A-domains have up to three divalent cation binding sites. One is permanently occupied in physiological concentrations of divalent cations, and carries either a calcium or a magnesium ion. The other two sites become occupied by cations when ligands bind – at least for those ligands involving an acidic amino acid in their interaction sites (Figure 21). Many ECM proteins feature acidic amino acids as part of the RGD peptide.

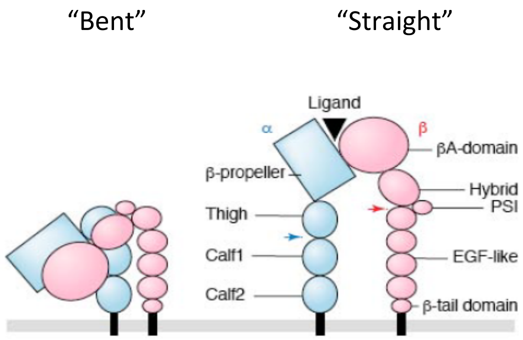

Figure 21| "Knee-jerk" model of integrin activation (adapted from [110])

1.9.2. αVβ3-integrin structure: extracellular domains

αVβ3 is one of the most promiscuous integrins, as it binds to multiple ligands including vitronectin, angiostatin, and osteopontin, and also serves as a receptor for several viruses such as foot and mouth disease virus, adenovirus, and human immunodeficiency virus [108].

The crystal structure of the extracellular domain of αVβ3 integrin was solved by Arnaout and colleagues [108], in what represented a truly major advance in the integrin field. Their work confirmed previous predictions of an A domain within the β subunit and of a β-propeller domain within the α subunit. The propeller domain and the β-A domain are complexed to form the ligand binding head of the integrin, which is attached to two legs, one from each subunit [108]. The N-terminal propeller domain of the α subunit is attached to a elongated leg formed of tree β sandwich domains termed thigh, calf1, and calf2 [105] (Figure 22).

The β subunit domain organization is slightly more complex; although the β-A domain is at distal end of the molecule (furthest from the C-terminal membrane insertion site), it is not at the N terminus of the primary sequence [108]. Instead, it is inserted into a loop in a so called hybrid domain [108]. The hybrid-A domain unit is preceded in the sequence by an N-terminal 54-residue PSI domain, which in the 3D structure lies below the hybrid A-domain”head” and is a disulfide bonded to the distal end of the β subunit leg [108] (Figure 22). This leg is formed of four tandem cystein-rich repeats highly characteristic of integrin β subunits [105], followed by a C-terminal disulfide-bonded β sheet domain termed the β-tail domain [105] (Figure 22).

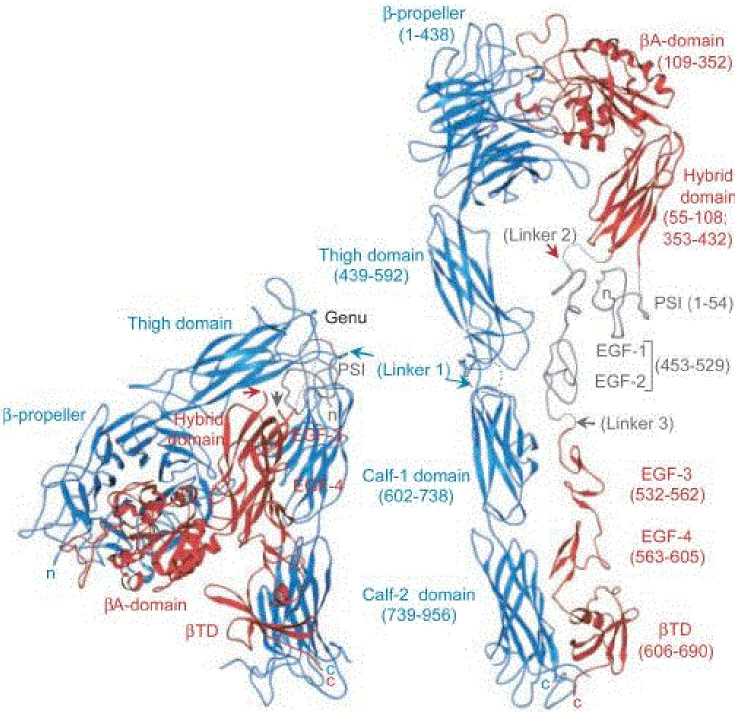

Figure 22| Structure of the extracellular segment of αVβ3 (adapted from [108]

1.9.3. RGD - αVβ3-integrin binding site

Crystal structures obtained after soaking cycloRGDF and Mg^{2+} into the crystal showed cycloRGD bound at the αβ interface with the arginine residue binding the propeller domain of the α subunit and the aspartate joining the coordination sphere of a Mn^{2+} ion bound at the MIDAS site [105] (Figure 23).

The Arg side chain inserts into a narrow groove at the top of the propeller domain (Figure 23a), formed primarily by the D3-A3 and D4-A4 loops [111]. The arginine guanidinium group is held in place by a bidentate salt bridge to Asp218 at the bottom of the groove and by an additional salt bridge to Asp150 at the rear (Figure 23b) [111]. The contacts leave most of the upper portion of the Arg side chain exposed to solvent, whereas the spacious rear of the groove probably contains water molecules that may provide additional contacts to the Arg guanidinium group [111].

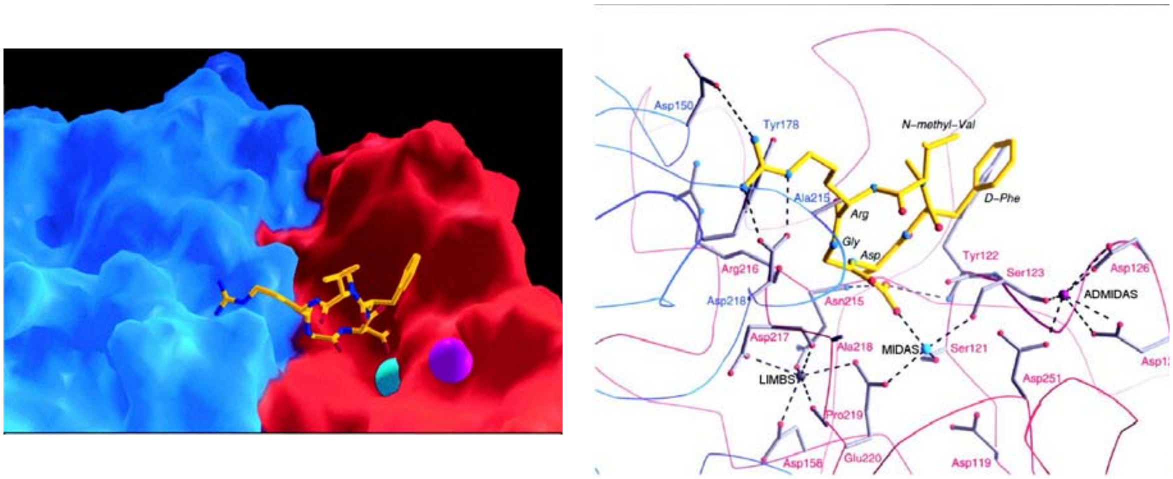

(a) (b)

Figure 23| The ligand-integrin binding site. (a) Surface representation of the ligand- binding site, with the ligand peptide shown as ball-and-stick model, where carbon, nitrogen, and oxygen atoms of cycloRGD are shown in yellow, blue, and red, respectively, and the two visible Mn^{2+} ions (MIDAS and ADMIDAS (adjacent to MIDAS)). (b) Interactions between ligand and integrin. The peptide (yellow) and residues interacting with the ligand or with Mn^{2+} ions are shown in ball-and-stick representation. αV and β3 residues are labeled blue and red, respectively. Oxygen and nitrogen atoms are in red and blue, respectively. The three Mn^{2+} ions in β3 at MIDAS, ADMIDAS, and LIMBS are also shown. Hydrogen bonds and salt bridges (distance cutoff, 3.5 Å) are represented with dotted lines (adapted from [111]).

Contacts between the ligand Asp and βA primarily involve the Asp carboxylate group. One of the Asp carboxylate oxygens contacts a Mn^{2+} ion at MIDAS in βA (Figure 23b). The second Asp carboxyl oxygen forms hydrogen bonds with the backbone amides of Tyr^{122} and Asn^{215} and also contacts the aliphatic portion of the Arg^{214} side chain. Additional contacts involve the hydrophobic portion of the Asp side chain and the beta carbon atom of Asn^{215}. Unlike the ligand Arg, the ligand Asp side chain is completely buried in the complex [111].

The glycine residue, which completes the prototype RGD ligand sequence, lies at the interface between the α and β subunits (Figure 23b). It makes several hydrophobic interactions with αV, the most critical of which appears to be the contact with the carbonyl oxygen of Arg^{216}. The remaining two residues of the pentapeptide face away from the αβ interface and are not in the consensus ligand sequence [111].

1.9.4. Requirements of RGD-peptide as an αVβ3 ligand

The RGD sequence constitutes the basic module for a variety of RGD containing peptides (Figure 24) which display preferencial binding to either αVβ3 integrin and related αV, or other types of integrins [6].

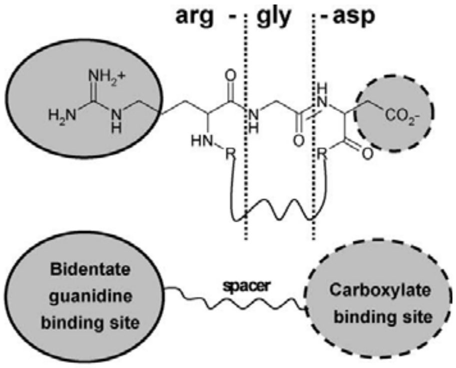

Figure 24| Schematic representation of the RGD binding motif (adapted from [6])

It is accepted that the relative affinity and specificity of all natural and synthetic RGD ligands, is highly depend by other amino acid residues flanking the RGD motif, especially at the two positions following the aspartic acid [112].

These residues, in addition to directly interacting with the integrin, flanking groups influence the folding of the peptide and thereby the conformational features of the RGD motif [6]. Cyclization, which confers rigidity to the structure, is commonly applied to improve the binding properties of the RGD-peptides. Furthermore, linear RGD peptides showed highly susceptible to chemical degradation, which usually is due to the reaction of the aspartic acid (D) residue with the peptide backbone [113]. Once the rigidity conferred by cyclization prevents this, cyclic peptides are more stable. Also the modification of the peptide with non natural amino acids, such as the introduction of the D-amino acids as well as the replacement with the peptidomimetic structures have yielded RGD peptide ligands with increased specificity and nanomolar or higher affinity [114].

The RGD peptide c(RGDf-N(Me)-V), also known as Cilengitide (Structure 1), is one of the best studied RGD peptide ligands for αVβ3 integrin. This RGD peptide displays affinity in the subnanomolar range in competing with biotinylated vitronectin or fibrinogen for binding to immobilized integrinds [6]. Cilengitide has also an exceptional selectivity, displaying a 1000 fold preference for αVβ3 integrin over αIIbβ3 integrin [115]. The reasons for these features were attributed to the constrained ring structure and the introduced D-amino acid residue that force the RGD-sequence into the proper conformation for binding to the αVβ3 integrin.

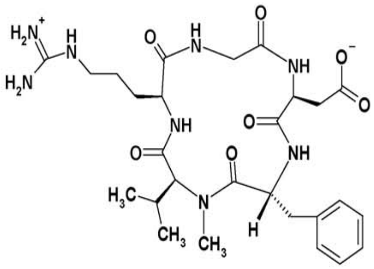

Structure 1| c(RGDf[N-Me]V) also known as Cilengitide

The mechanism of action of this drug is thought to happen in two ways: through attacking the tumor cells directly in a targeted manner and through starving tumor cells by stopping the formation of new blood vessels (angiogenesis) that feed the tumor [116]. Cilengitide belongs to a new class of investigational targeted anti-cancer therapies – the integrin inhibitors. At present date, Merck's Cilengitide has reached phase III for the treatment of glioblastoma and phase II clinical trials for the treatment of non-small cell lung cancer and prostate cancer [117]

1.9.5. Integrins in cancer

The role of integrins in cell migration and invasion is one of their most studied functions in tumour biology [118]. Integrins directly bind components of the ECM and provide the traction necessary for cell motility and invasion [119]. Integrins continue to regulate cell growth in some tumours, despite the deregulation of adhesion dependent control of proliferation in tumour cells. In addition to their ligation dependent effects, in some cases unligated integrins can positively or negatively influence tumour cell survival, consequently affecting tumour growth and metastasis. The way integrins affect tumour cells in their ligated or unligated states is a crucial determinant of the efficacy of integrin antagonists in cancer [119].

Integrins are also expressed in tumour associated host cells, such as the vascular endothelium, perivascular cells, fibroblasts, bone marrow-derived cells and platelets [119]. Integrins on the surface of these tumor associated cells can strongly influence the malignant potential of a tumour. Blocking crucial signaling events in the tumour microenvironment and in the tumour cells themselves, using integrin antagonists, may therefore inhibit tumour progression [119].

1.9.6. Targeted delivery of therapy

Integrin targeted therapeutics has proved successful delivering chemotherapeutics [5], oncolytic viruses [120], pro-apoptotic peptides [121] and radionucleotides [122] to both tumour cells and the supporting vasculature. A study by Murphy *et al.* [5] showed that delivery of targeted nanoparticles loaded with doxorubicin to integrin αVβ3 positive tumour vasculature inhibited the growth of metastasis while eliminated the toxicity and weight loss associated with systemic administration of this drug. This delivery method resulted in a 15-fold improvement in tumour anti metastatic activity when compared to administration of free drug. The preferential activity of these nanoparticles on metastases suggest that growing metastatic tumours may have a greater dependence on angiogenic vessels and consequently be more susceptible to integrin αVβ3 targeted therapy [119].

CHAPTER 2

2. EXPERIMENTAL SECTION

2.1. Reagents

Amino acids and RGD peptide were purchased from Bachem Bioscience (CA, USA), and all other chemicals were purchased from Sigma Aldrich (St. Louis, USA) at reagent grade. All chemicals were used as received.

2.2. Methods

2.2.1. Synthesis of N-carboxylated RGD peptide

H-Arg-Gly-Asp-OH (RGD) peptide was manually synthesized through the orthogonal protection scheme Fmoc/tBu Solid Phase Peptide Synthesis (SPPS), using a pre functionalized Wang resin (Fmoc-Asp(OtBu); 100-200 mesh; 0.54 mmol/g) from Novabiochem, Darmstadt, Germany. 100 mg of resin were used to fill the reaction vessel. Resin pre funtionalized with Asp, was sequentially washed with DCM, pipiridine 20% in N,N-dimethylformamide (DMF) for 1 min, Pipiridine 20% in DMF for 20 min, 4 x DMF for 1 min and finally with 5 x dichloromethane (DCM) for 1 min. After this the ninhydrin test was performed, using a sample of a few beads of resin.

Fmoc-GlyOH (Bachem Bioscience, CA, USA) was then added to the reaction vial dissolved in DCM and a few drops of DMF to clear the solution, followed by N,N'-Diisopropylcarbodiimide (DIPC). Reaction was allowed to proceed for 1 h with agitation each 10 min. System was then flushed, washed 3 x DMF for 1 min and 4 x DCM for 1 min and the ninhydrin test was performed as above. The same steps as for Gly were followed using Fmoc-Arg(Pbf)OH (Bachem Bioscience, CA, USA).

At this point the synthesis of RGD was accomplished and the modification with a succinil group of its N-terminal was started (adapted from Luedtke and Tor protocol [123]). N-terminal amino acid was deblocked by standard removal of the Fmoc protecting group with piperidine and then reacted for 1 h with succinic anhydride in DMF, in the presence of 1-hydroxybenzotriazole (HOBt) as auxiliary nucleophile and N,N-dimethylaminopyridine (DMAP) as condensation catalyst [123]. System was flushed, washed 4 x with DCM and ninhydrine test was performed.

Reaction vessel containing peptide coupled to resin was left under vacuum in a desiccator for 48 h.

Cleavage from resin and full side-chain deprotection was performed by acidolysis with a TFA-based cocktail containing carbocation scavengers (triisopropylsilane), and the cleaved peptide was precipitated with anhydrous methyl-tert-butyl ether (MTBE) in a liquid nitrogen bath (-196 °C). Cleaved peptides spectra were initially obtained by Liquid Chromatography (LC) and analyzed by Electrospray Ionization – Ion Trap Mass Spectrometry (ESI-IT MS) (Finnigan Surveyor LCQ DECA XP MAX) then purified by reverse-phase medium pressure liquid chromatography (RP-MPLC), lyophilized and finally analyzed by high performance liquid-chromatography/mass spectrometry (HPLC/MS - VWR – Hitachi LaChrom Elite). Peptide purity was also quantitated by HPLC equipped with a diode-array detector (DAD).

2.2.2. Synthesis of [Metal(Ligand)] complexes

Ligands and the metal salts precursor solutions were prepared separately in deionized H_2O (dH_2O). Ligand and metal precursors were then mixed, based on established stoichiometry (Table 6), in a capped 20 ml or 2 ml glass vessel. Additionally some reactions occurred in 10 ml Teflon-lined autoclave (Parr Instruments, Moline, IL, USA) or directly in a 24 well crystallization plate (Hampton Research, Aliso Viejo, CA, USA) (Table 6). These systems were then subjected to distinct synthesis conditions by changing variables such as solvent, temperature, heating/ cooling profiles (using a programmable oven, Memmert, Germany), sonication and agitation (Table 6).

2.2.3. Crystallization methods

As illustrated in Table 6, different crystallization trials were performed, such as natural evaporation of solvent, lyophilization and vapor diffusion (hanging drop, HD and sitting drop, SD). For natural evaporation of solvent the reaction vials were simply left open at atmospheric pressure and RT. Lyophilization process took place for ~48 h (Thermo Fisher Scientific, Waltham, MA, USA). Vapor diffusion techniques (HD, SD) were used in different setups where the effects of concentration of samples, the nature and concentration of precipitant, the volume of drop and pH were tested (Table 6).

2.2.4. Fourier transform infrared spectroscopy (FT-IR) spectra

FT-IR spectra of lyophilized samples were collected using a Bruker Tensor 27 with a Specac ATR window, at University of Aveiro, Portugal. Spectra were recorded from 300 to 4500 cm^{-1} with a resolution of 1 cm^{-1}

2.2.5. Circular Dichroism (CD) spectra

CD spectra of 1 mg/ml aqueous solutions (RGD, Cu^{2+} precursors and product of synthesis) used in P14D assay (Table 6) were measured on a spectropolarimeter with Jasco Canvas Program (model J-815, Jasco, Japan) over the wavelength of 190-260 nm.

2.2.6. Microscopy and Elemental analysis

Observation of synthesis results was primarily done using a light microscope (Nikon) connected to a digital visualization and recording apparatus (Nikon).

Scanning electron microscopy (SEM) and Energy Dispersive analysis of X-rays Spectroscopy (EDS) were performed using a FEI Quanta 400 FEG ESEM at CEMUP (FCT– Science and Technology Foundation contracts REEQ/1062/CTM/2005 and REDE/1512/RME/2005). Samples were prepared, after total solvent evaporation, by direct contact with carbon tape, previously placed on the sample holder.

2.2.7. Computational Methods

The purpose of this computational protocol was to perform a preliminary analysis of the interaction preferences between the motif Arg-Gly-Asp (RGD) and different metal atoms. Zn(II) was chosen as the first metal to be evaluated.

2.2.7.1. Model preparation

A starting structure for the RGD motif was prepared using Pymol. Special care was taken to assign an adequate protonation state to the motif. The side chains of Asp and Arg were considered ionized, the same happening for the C-terminal carboxylate group. The N-terminal amino acid group, one of the controversial interaction points with the metal, was considered neutral (instead of positively charged, as expected at neutral pH) to maximize the possibility of interaction with the metal.

An initial simulation cell with 100 RGD and 100 Zn units was prepared using the packmol program in an initial 40 Å cubic cell. This program distributes units in defined regions of space and guarantees that short repulsive interactions do not disturb the initial stage of simulation. It further ensures that the initial structure is unbiased, i.e. that the results will not be dependent on specific choices made by the user when constructing the initial structure. This is an important issue, as we are interest in finding in an unbiased way the preferred determinants for association.

2.2.7.2. Parametrization

The ANTECHAMBER module [124] of AMBER and the General AMBER Force Field (GAFF) [125] were used to parameterize RGD, with charges derived with RESP at the HF/6-31G(d) level of theory. For Zn(II) the standard parameters available in The Duan *et al.* 2002 force field were considered [126]. Prior to this parameterization scheme the RGD molecule was subject to a energy optimization performed in vacuum, at the same level of theory used in the charge calculation, a standard approach when dealing when organic molecules.

2.2.7.3. Molecular dynamics simulations

The AMBER 10 [127] molecular dynamics package was used in all the molecular dynamics simulations performed. The initial 100 RGD + 100 Zn model was then placed in a rectangular box containing a minimum distance of 12 Å of TIP3P water molecules between the RGD molecules and the box side. The total size of the system was of 25 712 atoms.

MD simulations were carried out using the PMEMD module of AMBER 10, and considering periodic boundary conditions to simulate a continuous system. The Particle-Mesh Ewald (PME) method [128] was used to include the long-range interactions, and a non-bond-interaction cut-off radius of 10 Å was considered. Following a 40 ps equilibration procedure, 10 ns MD simulations were carried out at 298 K, using Langevin temperature coupling and constant pressure (1 atm) with isotropic molecule-based scaling. An integration step of 1 fs was used. The MD trajectory was sampled every 2 ps. All of the MD results were analyzed with the PTRAJ module of AMBER 10.

Table 6| Summary of conditions for synthesis trials

Assay ID	**Ligand (L)**	**Metal salt/ Metal Ion (M)**	**L:M**	**n(L) mmol**	**n(M) mmol**	**Solvent(s)**	**Rx vol (ml)**	**pH**	**Synthesis Method**	**Heating|cooling setup**	**Crystallization method**	**Crystallization setup**
P1A	RGD	$FeCl_2.4H_2O$/ Fe^{2+}	2:1	2.9E-04	1.4E-04	dH_2O	2.0	5.5	Precursors mixed in 20 ml glass vial	1. 1 h @ 80°C 2. From 80°C to Room Temperature (RT) by Natural Convection (NC)	Sitting Drop (SD)	Total Volume: 20 µl V(sample): 8 µl V(NaOH 1 mM): [0-10] µl Precipitant: NaCl 2% V(precipitant): 500 µl
P1B				8.7E-07	4.3E-07							
P1C				1.7E-06	8.7E-07							
P1D				2.9E-06	1.4E-06							
P2A	RGD	$FeCl_2.4H_2O$/ Fe^{2+}	2:1	2.9E-04	1.4E-04	MeOH:NaOH 1M (9:1)	2.0	n.a.	Precursors mixed in 20 ml glass vial	1. From RT to 85 °C, ΔT=2 °Cmin^{-1} 2. 1 h @ 85°C 3. From 85 °C to RT, ΔT=-0.2 °Cmin^{-1}	SD	Total Volume: 10 µl V(sample): 10 µl Precipitant: Triethylamine 2% in MeOH V(precipitant): 500 µl
P2B				8.7E-07	4.3E-07							
P2C				1.7E-06	8.7E-07							
P2D				2.9E-06	1.4E-06							
P3A	RGD	$FeCl_2.4H_2O$/ Fe^{2+}	2:1	2.8E-07 5.7E-07 8.6E-07 1.2E-06 1.4E-06 1.7E-06	1.4E-07 2.8E-07 4.3E-07 5.7E-07 7.2E-07 8.6E-07	$DMF:dH_2O:EtOH$ (1:1:0.5) $DMF:dH_2O:EtOH$ (1:1:1) $DMF:dH_2O:EtOH$ (1:1:1.5) $DMF:dH_2O:EtOH$ (1:1:2)	0.020	n.a.	Precursors mixed directly in SD plate wells	5 min Sonication @ ~4 °C (directly on SD plate)	SD	Total Volume: 20 µl V(sample): variable µl Precipitant: Triethylamine 2% in EtOH V(precipitant): 500 µl
P4A	RGD *Citric acid	$FeCl_2.4H_2O$/ Fe^{2+}	2:1	2.0E-03 L + 1.5E-04 Citric Acid	1.0E-03	30 min boiled dH_2O	1.0	n.a.	Precursors and Citric Acid mixed in 20 ml glass vial	1. 1 h @ 80°C (with stirring) 2. From 80°C to RT by NC	Lyophilization	n.a.
P5A	Asp	$FeCl_2.4H_2O$/ Fe^{2+}	2:1	1.0E-2	5.0E-03	30 min boiled dH_2O	5.0	3.2 6.0 7.1	Precursors and Ascorbic Acid mixed in 20 ml glass vial	1. 1 h @ 80°C (with stirring) 2. From 80°C to RT by NC	Lyophilization	n.a.

								8.8				
P6A	Asp *Ascorbic acid	$FeCl_2.4H_2O$/ Fe^{2+}	2:1	1.0E-2 L + 0.75 Ascorbic Acid	5.0E-03	30 min boiled dH_2O	5.0	7.2	Precursors and Ascorbic Acid mixed in 20 ml glass vial	1. 1 h @ 80°C (with stirring) 2. From 80°C to RT by NC	Lyophilization	n.a.
P6BN								9.0				
P6C				1.0E-2 L + 5.0 Ascorbic Acid				7.0				
P6D								8.2				
P7A	RGD	$FeCl_2.4H_2O$/ Fe^{2+}	2:1	8.0E-3	4.0E-3	30 min boiled dH_2O	2.0	3.0	Precursors mixed in 20 ml glass vial	1. 1 h @ 80°C(+) (with stirring) 2. From 80°C to RT, ΔT=-1.0 °Cmin^{-1}	Hanging Drop (HD)	Drop Volume: 4 µl
P7B				4.0E-3	2.0E-3			5.4			Lyophilization	Drop Volume: 20 µl V(sample): 15 µl V(NaOH 1 mM): [0;1;3;5]µl Precipitant: NaCl 2% V(precipitant): 500 µl
P7C		$Zn(NO_3)_2.6H_2O$ / Zn^{2+}						5.8				
P7D		$MnCl_2.4H_2O$/ Mn^{2+}						5.9				
P7E		$MgCl_2.6H_2O$/ Mg^{2+}						5.9				
P8A	Asp	$FeCl_2.4H_2O$/ Fe^{2+}	2:1	1.0E-2	5.0E-3	30 min boiled dH_2O	5.0	n.a.	Precursors mixed in 20 ml glass vial	1. 1 h @ 80°C(+) (with stirring) 2. From 80°C to RT, ΔT=-1.0 °Cmin^{-1}	Lyophilization	n.a.
P8B		$Zn(NO_3)_2.6H_2O$ / Zn^{2+}										
P8C		$MnCl_2.4H_2O$/ Mn^{2+}										
P8D		$MgCl_2.6H_2O$/ Mg^{2+}										
P9A	RGD	$FeSO_4.7H_2O$/ Fe^{2+}	2:1	2.0E-3	1.0E-3	dH_2O	1.0	n.a.	Precursors mixed in 20 ml glass vial	1. 1 h @ 80°C(+) (with stirring) 2. From 80°C to RT, ΔT=-1.0 °Cmin^{-1}	Natural evaporation inside hood	n.a.
P9B		$Zn(NO_3)_2.6H_2O$ / Zn^{2+}										
P9C		$ZnSO_4.7H_2O$/ Zn^{2+}										
P9D		$Zn(CH_3COO)_2.2H_2O$/ Zn^{2+}										

P9E		$MgSO_4.7H_2O$										
P9F		$CuSO_4.5H_2O$										
P10A	RGD	$Zn(NO_3)_2.6H_2O$ / Zn^{2+}	2:1	4.5E-3	2.3E-3	MeOH:NaOH 1 M (9:1)	0.050	n.a.	Precursors mixed in 2 ml glass vial	1. From RT to 85 °C, ΔT=1 $°Cmin^{-1}$ 2. 1 h @ 85°C 3. From 85 °C to RT, ΔT=-0.2 $°Cmin^{-1}$	n.a.	n.a.
P10B				3.8E-3	1.9E-3							
P10C				2.5E-3	1.3E-3							
P10D				2.3E-3	1.1E-4							
P10E				2.0E-3	1.0E-3							
P10F				1.5E-3	7.5E-4							
P10G				1.0E-3	5.0E-4							
P10H				5.0E-4	2.5E-4							
P10I				2.5E-4	1.3E-4							
P12A	RGD	$Zn(NO_3)_2.6H_2O$ / Zn^{2+}	2:1	1.50E-03	7.50E-04	MeOH	0.050	9.3	Precursors mixed in 2 ml glass vial	1. From RT to 85 °C, ΔT=1 $°Cmin^{-1}$ 2. 6 h @ 85°C 3. From 85 °C to RT, ΔT=-0.2 $°Cmin^{-1}$	n.a.	n.a.
P12B				1.00E-03	5.00E-04							
P12C				5.00E-03	2.50E-04							
P12D				2.50E-03	1.25E-04							
P12E				3.00E-03	1.50E-03		0.10					
P12F				1.50E-03	7.50E-04	dH_2O	0.050	9.6				
P12G				1.00E-03	5.00E-04							
P12H				5.00E-03	2.50E-04							
P12I				2.50E-03	1.25E-04							
P12J				3.00E-03	1.50E-03		0.10					
P13A	RGD	$Zn(NO_3)_2.6H_2O$	2:1	5.20E-03	2.60E-03	dH_2O	0.050	n.a.	Precursors mixed in 2 ml	1. From RT to 85 °C, ΔT=1 $°Cmin^{-1}$	HD	Drop Volume: 4 µl V(sample): 4 µl

P13B		/ Zn^{2+}		2.60E-03	1.30E-03				glass vial	2. 12 h @ 85°C 3. From 85 °C to RT, ΔT=-0.2 °Cmin^{-1}		Precipitant: NaCl 2% V(precipitant): 500 µl
P13C				5.18E-04	2.59E-04							
P13D				5.18E-04	2.59E-04	dH$_2$O+10µl NaOH 1M						
P13E				5.18E-04	2.59E-04	dH$_2$O+20µl NaOH 1M						
P13F				2.59E-04	1.29E-04	dH$_2$O						
P13G				2.59E-04	1.29E-04	dH$_2$O+10µl NaOH 1M						
P13H		Zn(CH$_3$COO)$_2$.2 H$_2$O/ Zn^{2+}		5.18E-04	2.59E-04	dH$_2$O						
P13I				5.18E-04	2.59E-04	dH$_2$O+10µl NaOH 1M						
P13J				5.18E-04	2.59E-04	dH$_2$O+20µl NaOH 1M						
P14A	Asp	Zn(CH$_3$COO)$_2$.2 H$_2$O/ Zn^{2+}	2:1	5.00E-01	2.50E-01	dH$_2$O	5.0	10.2	Precursors mixed in 10 ml Teflon-lined autoclave	1. 72 h @ 150°C 2. From 150 °C to RT by NC	Filtration through a 0.2 µm filter	n.a.
P14B	Gly			1.35E-01	6.75E-02			9.3				
P14C	Arg			5.00E-01	2.50E-01			9.3				
P14D	RGD	CuCl$_2$.H$_2$O/ Cu^{2+}	2:1	1.25E-02	6.25E-03	dH$_2$O	0.25	~ 8	Precursors mixed in 2 ml glass vial	1. 6 h @ RT (with stirring)		
P15A	RGD Adenine (AdeH)	Cd(NO$_3$)$_2$/ Cd^{2+}	1:1:2	RGD: 2.50E-02 AdeH: 2.50E-02	5.00E-02	dH$_2$O	5.00	5.1	Precursors mixed in 10 ml Teflon-lined autoclave	1. From RT to 140 °C, ΔT=0.1 °Cmin^{-1} 2. 72 h @ 140°C 3. From 140 °C to RT, ΔT=-0.08 °Cmin^{-1}	n.a.	n.a.
P16A	Succinated RGD (sucRGD) Adenine (AdeH)	Cd(NO$_3$)$_2$/ Cd^{2+}	1:1:2	sucRGD: 2.50E-02 AdeH: 2.50E-02	5.00E-02	dH$_2$O	5.00	5.0	Precursors mixed in 10 ml Teflon-lined autoclave	1. From RT to 140 °C, ΔT=0.1 °Cmin^{-1} 2. 72 h @ 140°C 3. From 140 °C to RT, ΔT=-0.08 °Cmin^{-1}	n.a.	n.a.
P17A	RGD Adenine (AdeH)	Cd(NO$_3$)$_2$/ Cd^{2+}	1:1:2	RGD: 1.25E-02 AdeH: 1.25E-02	2.50E-02	dH$_2$O	2.5	5.6	Precursors mixed in 10 ml Teflon-lined autoclave	1. From RT to 140 °C, ΔT=0.1 °Cmin^{-1} 2. 72 h @ 140°C 3. From 140 °C to RT, ΔT=-0.08 °Cmin^{-1}	n.a.	n.a.
P17B								6,0				

CHAPTER 3

3. RESULTS AND DISCUSSION

The original idea for this project consisted in synthesizing a metal-peptide framework based on two biocompatible components, the RGD peptide and the Fe(II) cation. The prototypical examples of metal-peptide frameworks reported by [2, 3, 31] gave the necessary directives to set some of the conditions for the first reactions. Our initial bet was that a modified version of the RGD peptide, flanked by two C terminal carboxyl groups, would preferentially coordinate the metal cation, at a specific pH to be experimentally determined, through its carboxylate groups, enabling the formation of an ordered network. We expected that, similarly to previously published works [2, 3, 31], these structures would result in open 3D networks with some degree of porosity.

3.1. Synthesis of N-carboxylates RGD peptide

The first step consisted in the synthesis of a new RGD peptide by modifying its N-terminal through a reaction with succinic anhydride in DMF, after removing the Fmoc protecting group from its Arg N-terminal (Scheme 2).

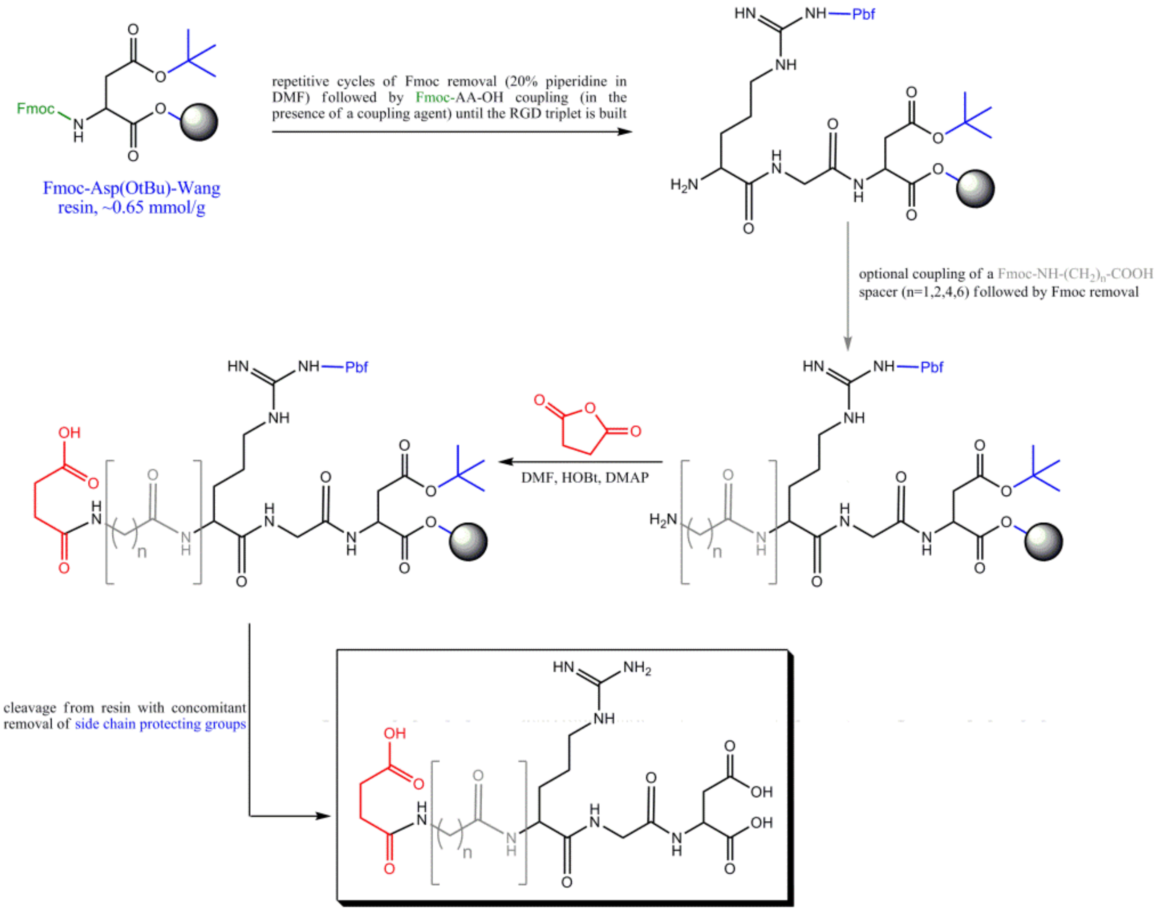

Scheme 2| Schematics of N-carboxylated RGD synthesis. Succinic anhydride was added in the presence of HOBt as auxiliary nucleophile and DMAP as condensation catalyst.

3.1.1. Purification of N-carboxylated RGD peptide

As revealed by Liquid Chromatography/ Diode Array Detection-Mass Spectrometry (LC/ DAD-MS) analysis, it was possible to identify the succinate modified peptide (SucRGD) at a time of retention (tr) of 9.04 min, though as shown in Figure 25, its relative abundance is low, namely in relation to the subproduct presenting a tr of 10.58 min.

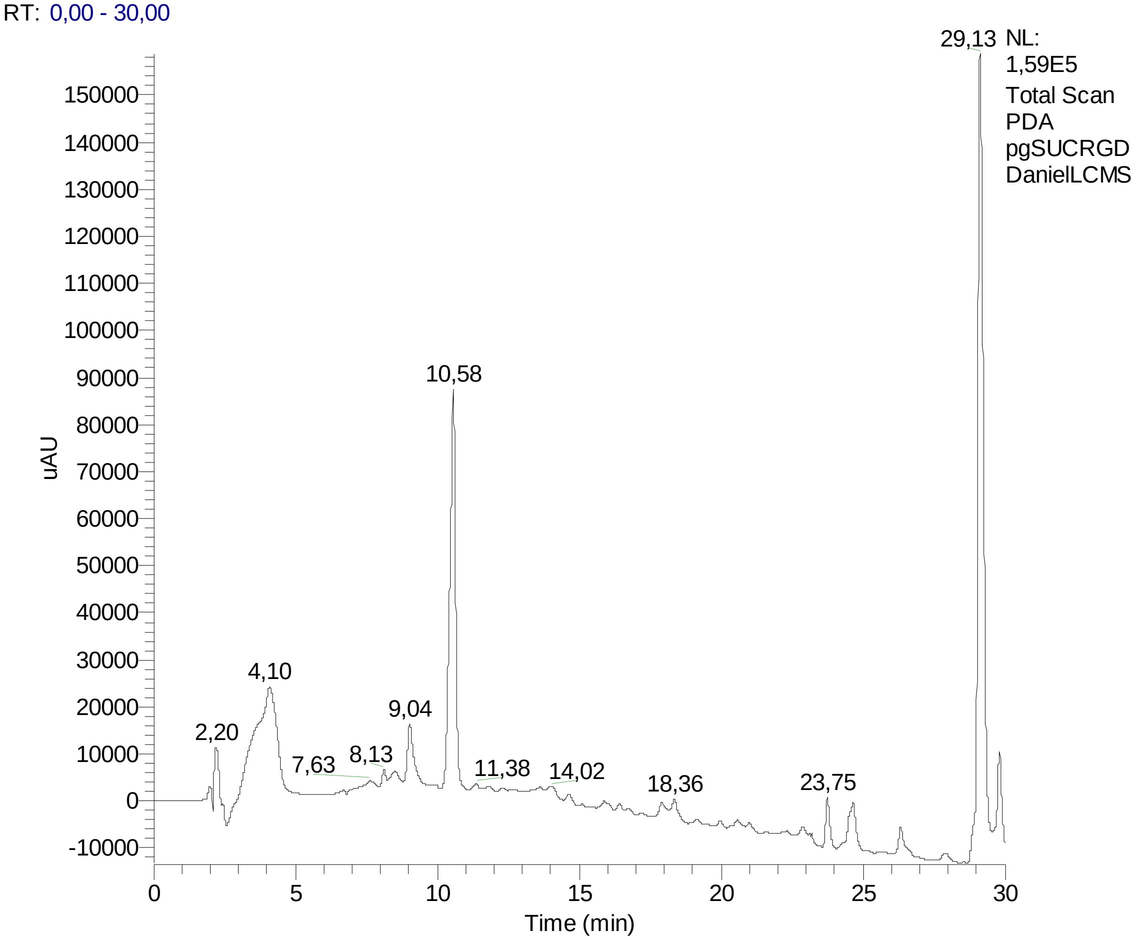

Figure 25| Chromatogram from the synthesized peptide. LC/DAD-MS (UV detection, λ=220 nm), tr= 9.04 min, flux = 0.5 mL/min; Column Nucleodur C18 Gravity

The subsequent analysis of product at 9.04 min by Electrospray Ionization – Ion Trap Mass Spectrometry (ESI-EI/MS) working at positive mode (+p) gave a reason *m/z* of 447.20 [M+H+] for a corresponding expected reason of m/z_{expected} of 446.70 (Figure 26), what confirms the success of the peptide modification by the used synthetic procedure. It is also possible to detect the formation of SucRGD dimmers showing a reason *m/z* of 893.07 (Figure 26).

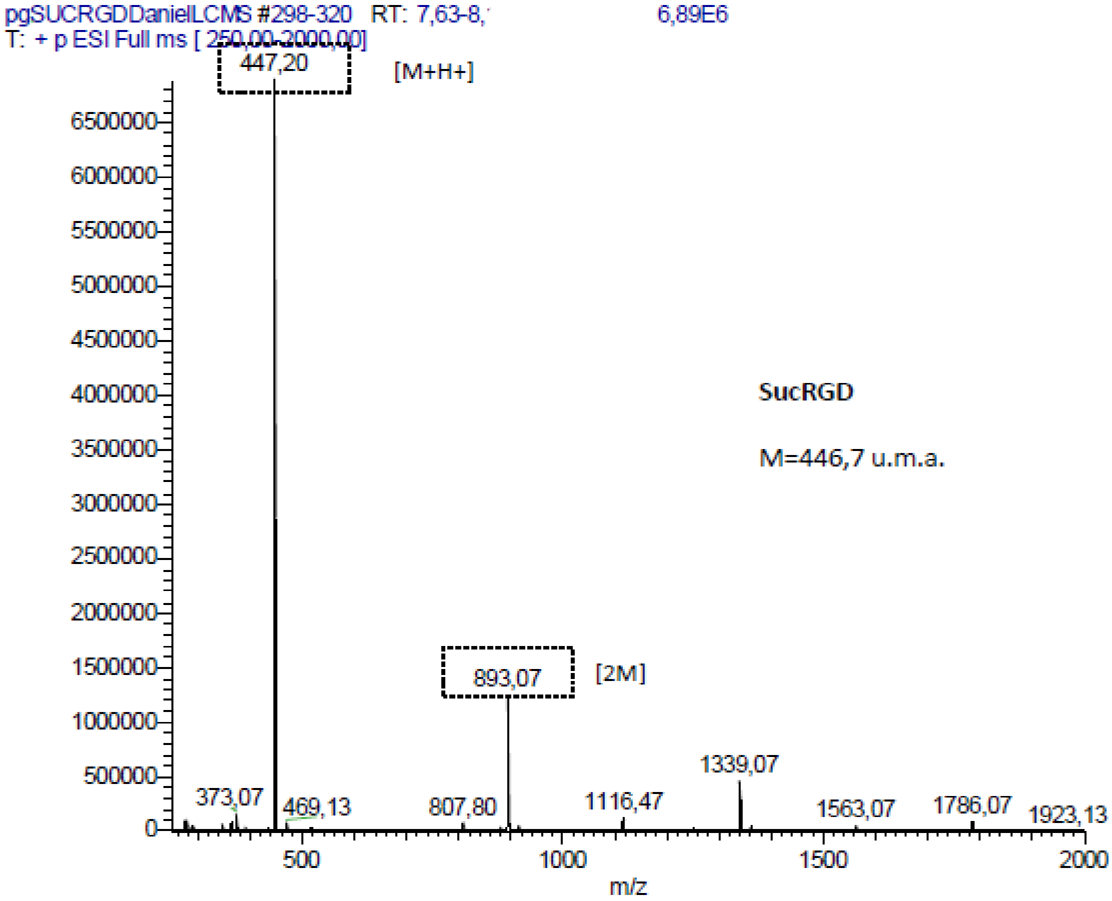

Figure 26| ESI-IT Mass Spectrum from peptide collected by LC-MS, showing the associated value of *m/z* = 447.20 corresponding to the expected ($m/z_{expected}$= 446.7).

The isolated SucRGD peptide fraction presented a final purity of 91.42% as shown in the final HPLC-DAD chromatogram (Figure 27).

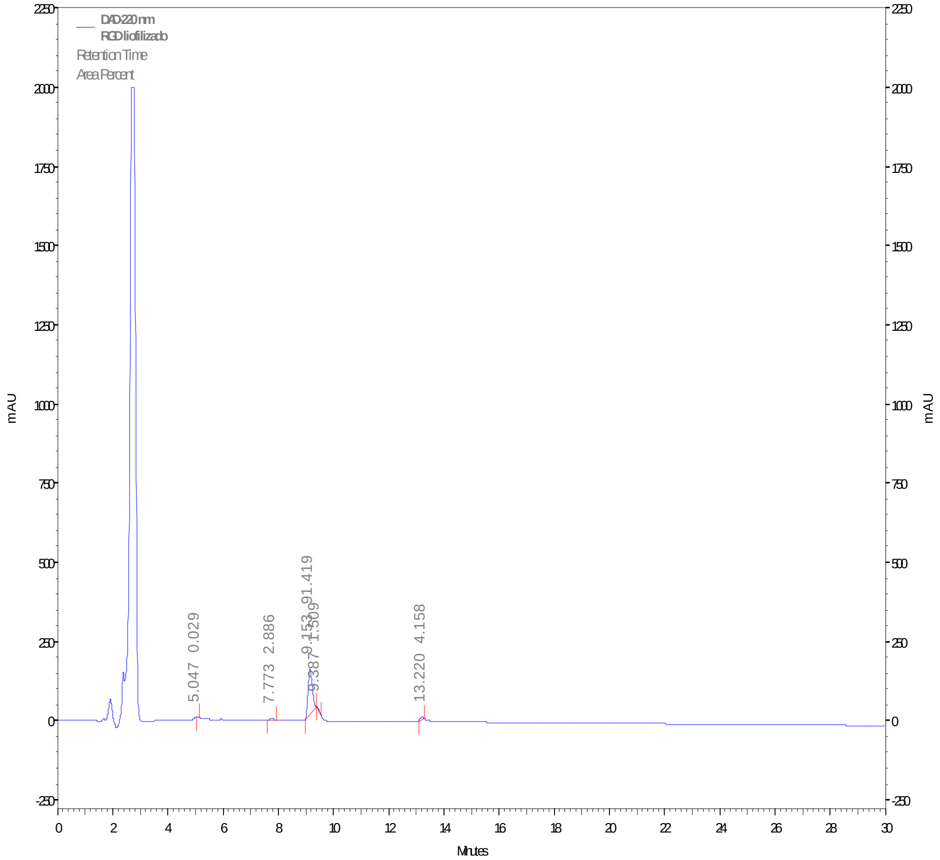

Figure 27| HPLC-DAD chromatogram of synthesized peptide (crude product) under the following conditions: 5 μm Purospher Star RP-C18 column, 150×4.6 mm; 0 to 100% of B in A (A=H_2O with 0.05% TFA; B=CH_3CN) in 30 min and at a flux of 1 mL/min; detection at λ=220 nm ; V $_{\text{injected sample}}$=20 μL.

Table 7| DAD-220 nm results

Retention Time	Area	Area %	Height	Height %
5.047	1858	0.03	0	0.00
7.773	186953	2.89	18878	3.11
9.153	5922471	91.42	555276	91.41
9.387	97737	1.51	0	0.00
13.220	269338	4.16	33328	5.49
Totals	6478357	100.00	607482	100.00

The ESI-IT MS from the isolated SucRGD peptide confirmed a *m/z* reason of 447.20 and no dimmers were detected (Figure 28).

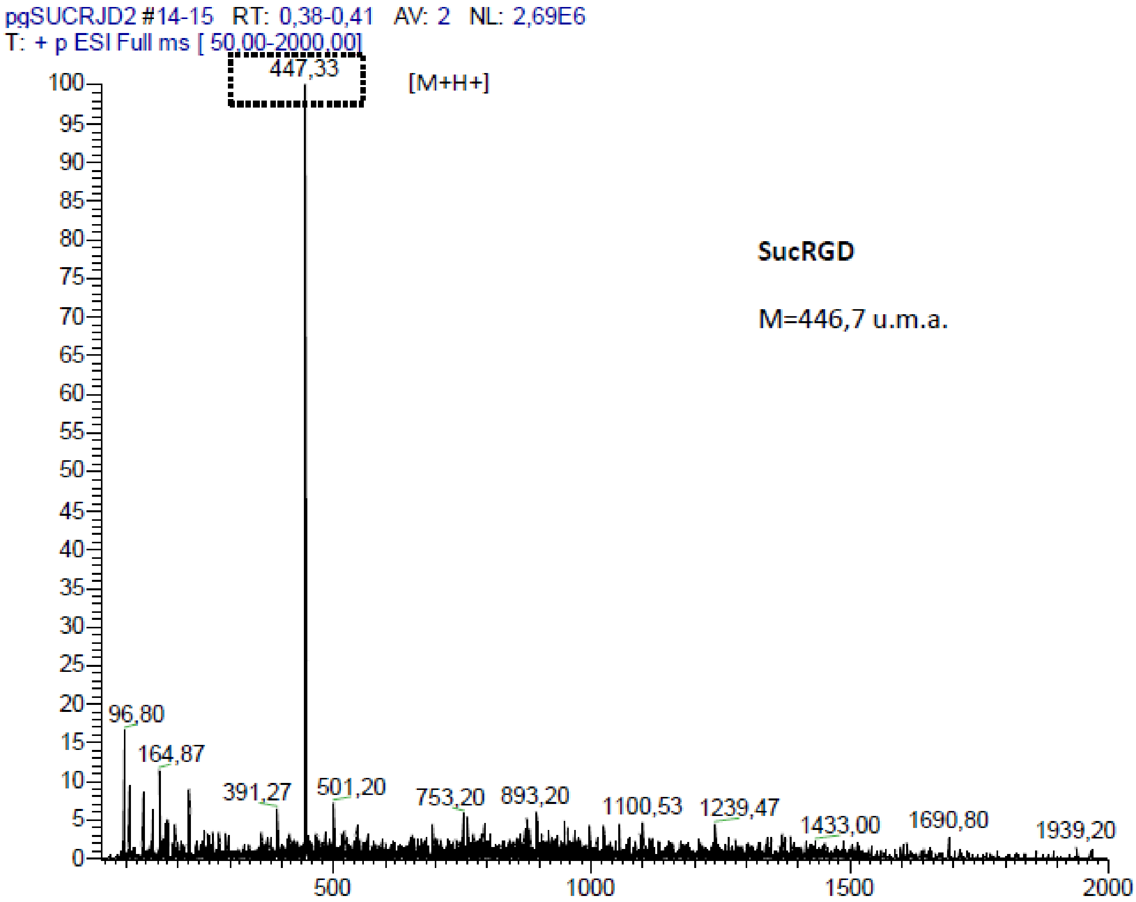

Figure 28| ESI-IT MS spectra from the isolated peptide, showing the correspondence between the obtained reason *m/z* = 447.33 and the expected reason *m/z* = 446.7

3.2. RGD Net Charge Variation With pH

In order to study the influence of pH in the formation of the complexes, the pH was set everytime the reaction volume allowed the use of the available pH sensor. The charge contribution of each of the ionizable groups in RGD, namely at the N-terminus, at the C-terminal, at Arg guanidinum and Asp carbonyl group vary with pH. Figure 29 shows how the net charge of the peptide varies with pH, and from here one can notice that for pH < 4 positive charges are predominant, and that for pH > 8 negative charges predominate.

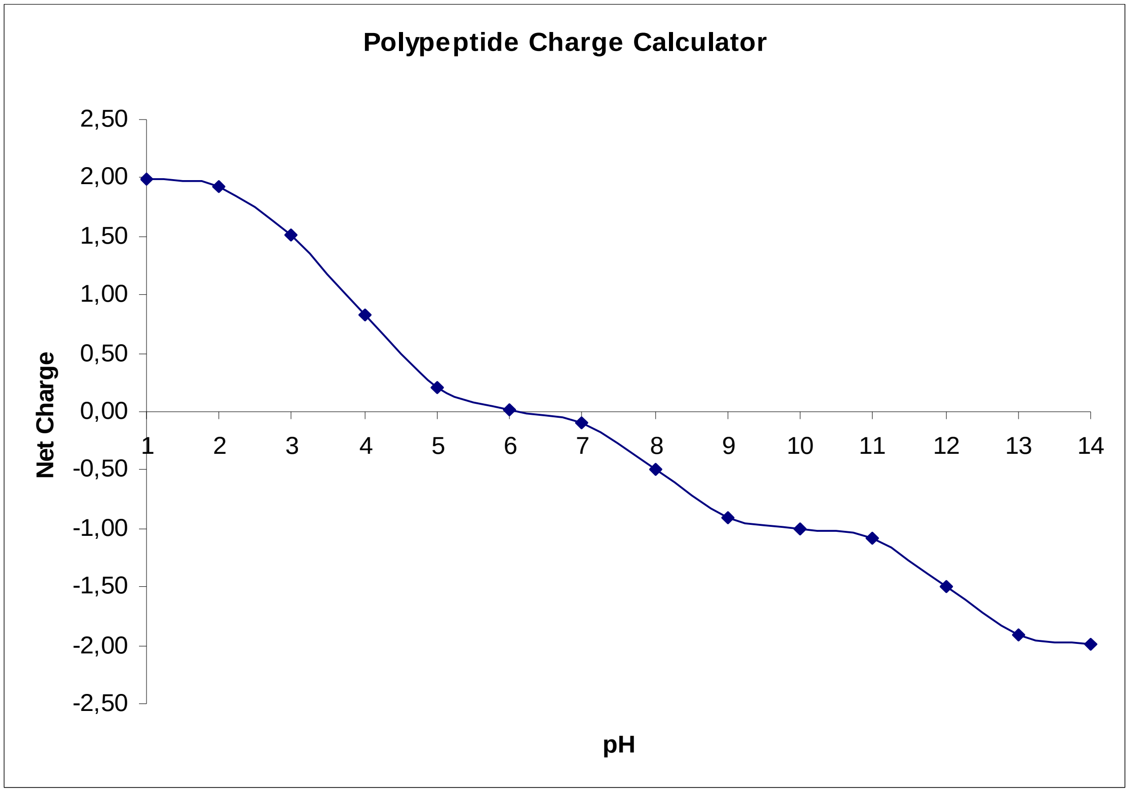

Figure 29| Variation of RGD net charge with pH, considering the contribution of C terminal (Asp), N terminus (Arg) and both residues side chains (model based on Henderson-Hasselbalch equations and developed by Gale Rhodes, University of Southern Maine).

This relation between the RGD peptide net charge and pH reveals the best pH range regarding the coordination through its ionizable groups. For coordination to occur it is essential that the ligand has at least a pair of unshared electrons [52]. While at the carbonyl groups (C terminal and Asp side chain) there are always unpaired electrons from the oxygen atoms, this is not the case for amine groups (N terminus and Arg side chain), that once positively charged do not posses any unshared electron pairs. For this reason one can suppose that at pH > 8, all the RGD carbonyl and amine groups will possess coordination capacity.

In the ideal scenario, the coordinating groups would be “active” or “inactive” by setting the pH to a determined value. This could allow to tune the geometry of the complex in order to favor crystal formation and consequently to obtain distinct framework architectures.

3.3. Synthesis and Crystallization "Trials"

3.3.1. Peptide MOFs

3.3.1.1. [Fe(RGD)]

Conditions leading to the formation of a complex of Fe(II) (from $FeCl_2.4H_2O$ or $FeSO_4.7H_2O$) and RGD are listed in Table 6. Despite the unsuccessful crystallization trials for using these precursors, it was possible to study some of the idiosyncratic aspects of bivalent iron and their implications in the formation of metal-organic complexes. The major hurdle found while working with Fe(II) was to avoid its spontaneous oxidation to Fe(III). Stumm and Morgan [129] presented a kinetic equation for the oxidation of Fe(II) to Fe(III) with O_2 (aq) as the electron acceptor:

$$\frac{-d\left[Fe^{2+}\right]}{dt} = k\left[Fe^{2+}\right]\left[OH^{-}\right]^{2} p_{O_2} \qquad (1)$$

This equation shows that below pH~4 the rate of oxidation becomes very low, and is fundamentally independent of pH. Millero [130] also presented data for the rate of oxidation of Fe(II) in solution which, among other observations, includes observations at pH values higher than 6. Millero's results indicate that at pH values greater than ~8 the rate of ferrous oxidation is also independent of pH, though at alkaline pH the concentration of soluble Fe(II) species is so low due to the formation of ferrous hydroxide ($FeOH^+$, $Fe(OH)_3^-$, $Fe(OH)^0{}_2$) species that it is very difficult to obtain reasonably accurate empirical kinetic data [131]

Strategies used in the present work to avoid Fe(II) oxidation included (1) the deaeration of water used in solutions, by boiling it for ~30 min, (2) the saturation of the free volume inside vials with N_2 gas, and (3) the use of known antioxidant species such as citric and ascorbic acid.

Crystallization trials using Fe(II) (P1A-P6D;P7A;P8A;P9A) did not lead to the formation of suitable X-ray diffracting crystals. When SD vapor diffusion technique was used it was possible to observe the formation of crystal like structures (Figure 30a-d) too small for X-ray data collection. Nevertheless, most of the wells presented orange amorphous structures, attributed to oxidized Fe(III) precipitate (Figure 30e-f).

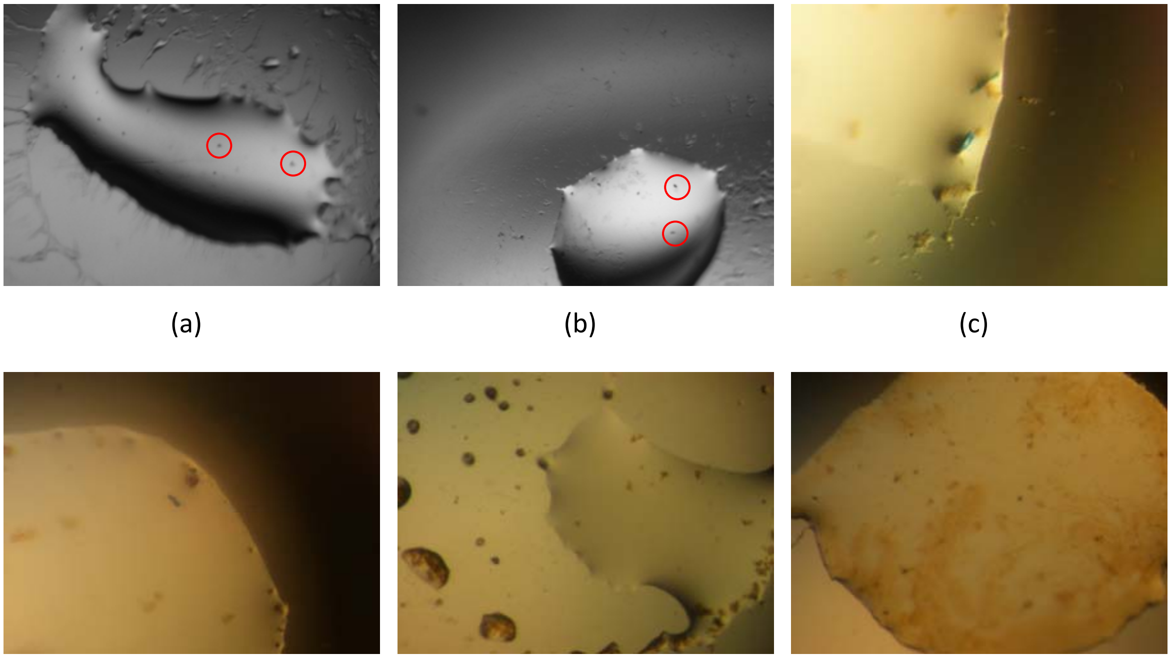

(a) (b) (c)

(d) (e) (f)

Figure 30|Representative results for crystallization trials from assay ID P1A to P1D

The small dots that can be observed in Figure 30a,b were admitted to be small crystals, and based on that assumption we tried to make them grow larger by soaking the well with additional solution of metal and peptide. Though, this strategy was not successful and no crystal growing could be detected.

Based on Rossensky *et al.* [3] procedures we decided to try a combination of MeOH:NaOH 1M (9:1) as solvent, and a different heating/ cooling setup (Table 6 P2A-P2D). Most of the wells in the SD plate showed a clear solution, though it was still possible to observe some crystal like structures (Figure 31a,b) and an orange precipitate (Figure 31c). The SD setup revealed not adequate when using solvents as MeOH, once the solvent condenses in the cover strip, making impossible to make observations under the microscope.

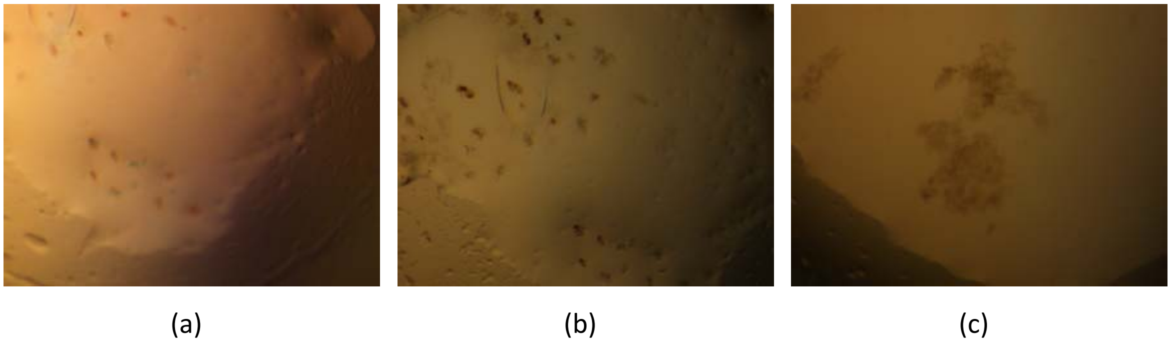
(a) (b) (c)

Figure 31| Representative results for crystallization trials from assay ID P2A to P2D

The next assays for the Fe(II) and RGD system were set up based on Lee *et al.* [2] procedures where different proportions of the triphasic system DMF:dH_2O:EtOH were used as solvents. Here we also tried sonochemical synthesis, in which high energy ultrasounds creates alternating areas of compression (high pressure) and rarefaction (low pressure) which result in formation, growth and collapse of small bubbles. This process called cavitation leads to the rapid release of energy with heating and cooling rates of > 1010 Ks^{-1}, temperatures of ~5000 K and pressures of 1000 bar.

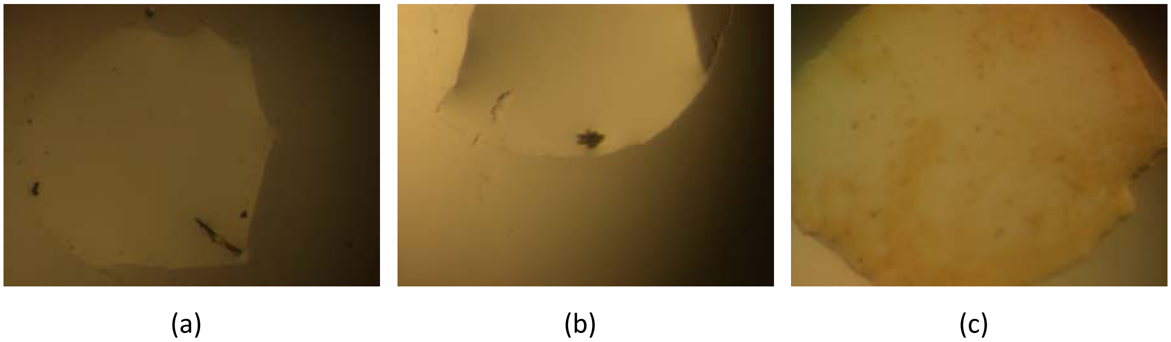
(a) (b) (c)

Figure 32| Representative results for crystallization trial from assay ID P3A

As it can be seen in Figure 32, wells presented a clear solution, amorphous solids or orange precipitates in suspension.

From the observations made for assays (P1A to P3A), despite no solid conclusions can be taken, one can speculate about the influence of solvent polarity. Once the mostly crystalline structures appeared in P1 assays using H_2O as solvent, this seems to be an appropriate solvent for the Fe(II) - RGD system.

3.3.1.2. [Zn(RGD)] and other [M(RGD)]

To test the capacity of RGD to coordinate different transition metals and to overcome the drawbacks found while working with Fe(II), it was decided to extend the set of biocompatible metals, namely Zn(II), Mn(II), Mg(II) and Cu(II) (Table 6).

For these assays (P7A-E, P14D) the reaction volume was decreased what allowed the use of higher concentrations of precursors (Table 6). Even though, it was not possible to notice crystal formation in any of the trials. Again precipitate has formed where Fe(II) and Cu(II) were used, and amorphous solids or clear drops were observed when Zn(II), Mn(II) or Mg(II) were used (Figure 33).

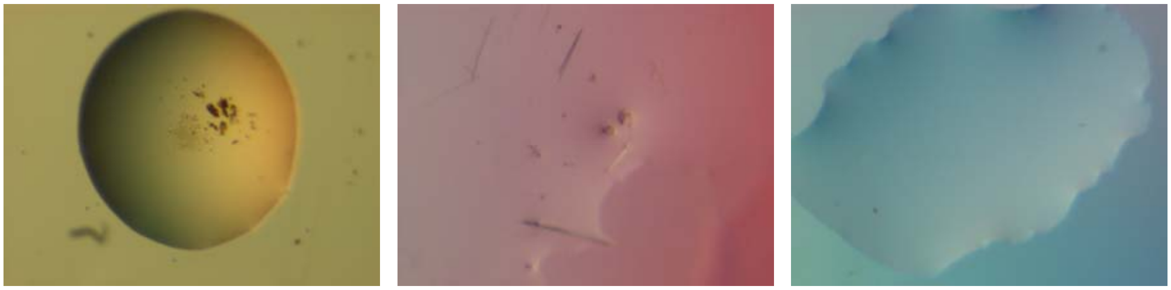

(a) *Fe* (b) *Zn* (c) *Mn*

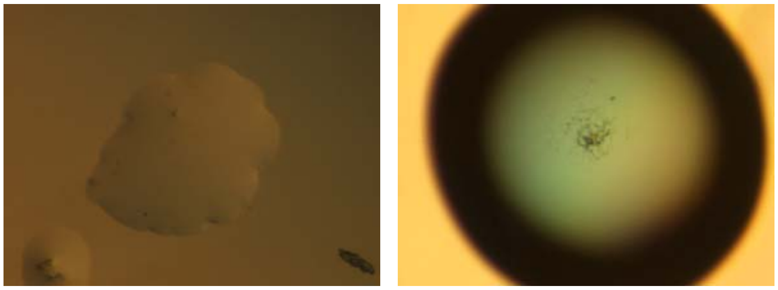

(d) *Mg* (e) *Cu*

Figure 33| Representative results for crystallization trials from (a-d) assay ID P7A-E and (e) P14D

In addition to the use of HD vapor diffusion technique for crystal formation, a set of reactions (P9A-P9F) were prepared using different metal precursors, where natural evaporation (RT, 1 atm) of solvent directly from reaction vials was let to happen. Observations are shown in Figure 34, where it is possible to notice crystalline structures, namely where Zn(II), Mg(II) and Cu(II) were used (Figure 34b, c, e, f). These crystals presented dimensions that allowed them to be mounted in the X-ray difractometer, though any of them allowed the collection of interpretable X-ray data. These solids were attributed to crystals of the metal salt only.

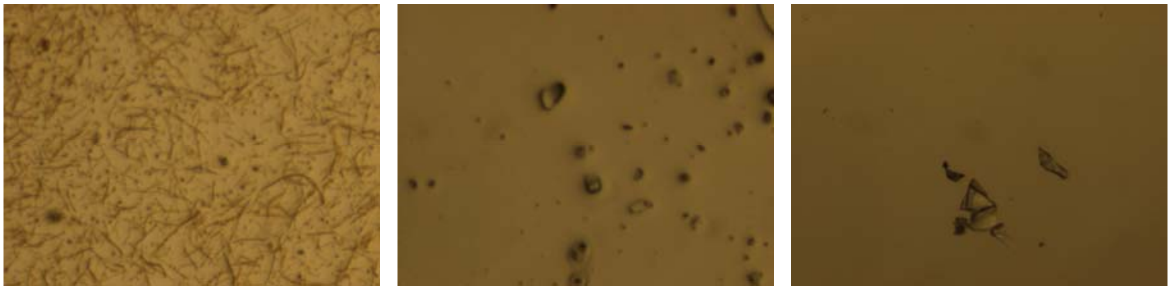

(a) *Fe* (b) *Zn* (c) *Zn*

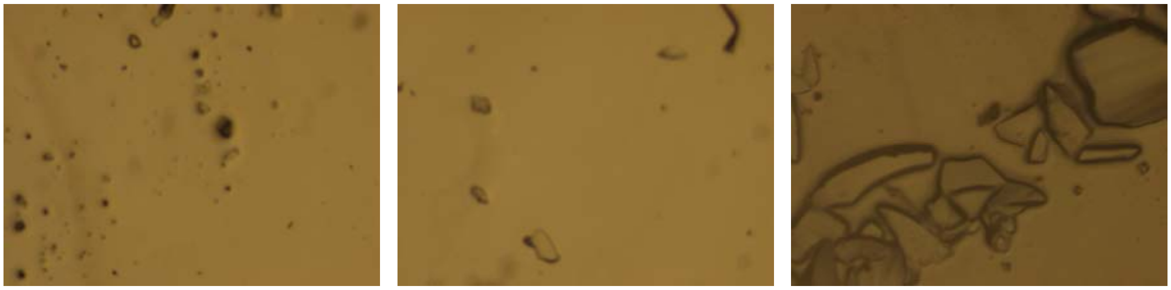

(d) *Zn* (e) *Mg* (f) *Cu*

Figure 34| Representative results for crystallization trials from (a-f) assay ID P9A-F

Zn(II) was already proven to be a good candidate to the formation of metal-aminoacid/ peptide complexes [3, 30]. Hence to explore the influence of the metal salt, Zn(II) was further investigated as metal precursor through the use of some of its different salts - $Zn(NO_3)_2$, $Zn(CH_3COO)_2$, $ZnSO_4$ (assay ID P9B-D). Moreover Zn(II) in the form of $Zn(NO_3)_2.6H_2O$ was used as metal precursor to test MeOH as solvent and the influence of reaction pH. Reactions took place in reduced volumes of 50 µl and subjected to heating/cooling setups with slow temperature variations and extended maximum temperatures (T_{max}) plateaus. Apparently, for the conditions tested the metal salt had no influence in the formation of crystals, since all attempts of crystallization were unsuccessful.

The first set of assays (P10A-P10I) led to the formation of a white amorphous precipitate immediately after mixing the metal and RGD peptide precursor solutions, attributed to $Zn(OH)_2$, which is insoluble. The amount of precipitate varied in a direct proportion with the concentration of precursors. Additional assays were performed in order to avoid the instantaneous formation of the solid by decreasing the precursor quantities and by changing the solvent composition and pH (assays ID P10A to P13E - Table 6). Sample analysis of the referred precipitate by SEM-EDS can be seen in Figure 35.

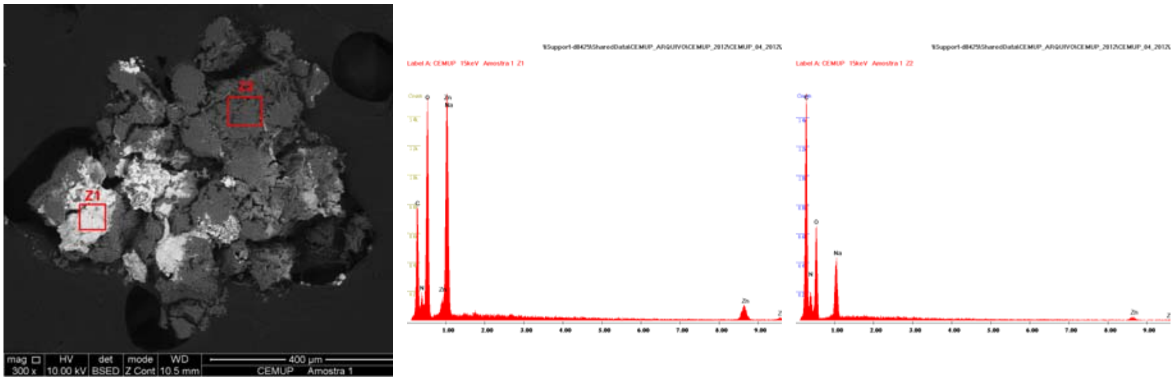

(a) (b) (c)

Figure 35| (a) SEM images of insoluble solid formed after mixing $Zn(NO_3)_2$ and RGD precursor (assay ID P10A). (b,c) EDS spectrum for two distinct zones on the solid (Z1 and Z2).

SEM-EDS revealed the amorphous aspect of the solid (Figure 35a) and the existence of different composition zones (Figure 35b,c). While the light grey colored zone Z1 is composed of C, O, some N and what can be considered high amounts Zn, the dark grey Z2 has only traces of Zn making this structure very heterogeneous in composition. The co-localization of the Zn and C, O and N at Z1 can be interpreted by the presence of a Zn-RGD complex.

3.3.1.3. [Cu(RGD)]

Cu(II) ion has been known to be able to coordinate with peptides to form Cu(II)-peptide complexes with rigid conformation and to induce the peptides self-assembling at nano-scale [132]. Li et al. [132] had shown that Cu(II) can form complexes with RGD octapeptides.

CD spectral analysis of P14D assay, where Cu(II) was reacted with RGD peptide under the same conditions used by Li et al. [132] are shown in Figure 36a. The information provided by this spectrum is limited though it is possible to note the difference between the curve for the potential Cu(II)-RGD complex and the precursor curves. When compared with typical CD curves, which provide a probe of protein secondary structure (Figure 36b), Cu(II)-RGD curve seems to partial fit to a typical coiled structure curve. This somehow is against what was expected once, as stated above, the formation of Cu(II)-peptide complexes, should result in linear, rigid conformation complexes. If that was the case of Cu(II)-RGD complex one would expect to obtain a better fitting to a type of curve that is obtained when beta sheets are present.

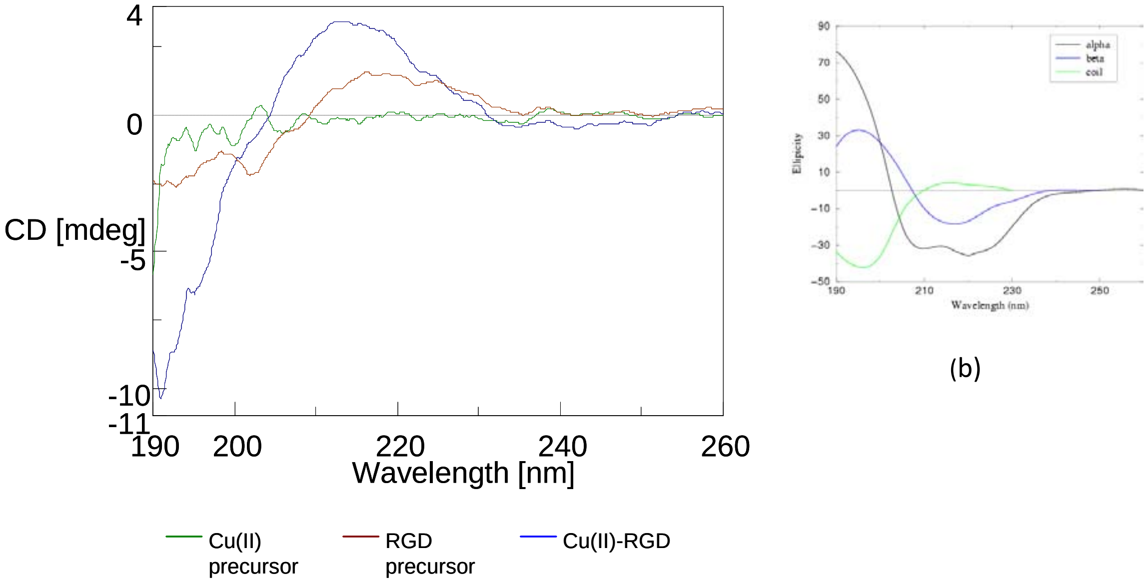

(b)

(a)

Figure 36| (a) CD spectrum of separate Cu(II) and RGD precursor and for the product of reaction between both, in the conditions of assay ID P14D (Table 6). (b) Typical CD curves used for probing protein secondary structure.

CD analysis could be enriched if spectrum was recorder for a wider range of wavelengths. It was expected that negative bands were present at ~550 nm, which are characteristics of the d-d transitions in Cu(II) at a complexation reaction.

3.3.2. Adenine MOFs incorporating RGD and sucRGD

Yang *et al.* [104], reported the use of hydrothermal synthesis to obtain a complex built from Cd(II), the nucleobase adenine (adeH) and adipic acid (H_2ap). Synthesis conditions were reproduced where the H_2ap was substituted by RGD (P15A) and SucRGD (P16A) peptides. The exact same conditions reported were used as a control, while some reactions were set at a different pH than reported (P17A,B).

Results from the microscopic observation of the reaction products, collected immediately after the opening of the Teflon autoclave can be seen on Figure 37. When RGD was used (P15A), it was possible to observe agglomerates of spherical structures at the surface of the solution (Figure 37a,b), while amorphous solids deposited in the bottom (Figure 37c). When sucRGD was used (P16A) only amorphous solids could be observed (Figure 37d-f). By altering the pH for 5.6 (P17A) and 6 (P17B) for reactions involving RGD, it is possible to observe changes in the aspect of products.

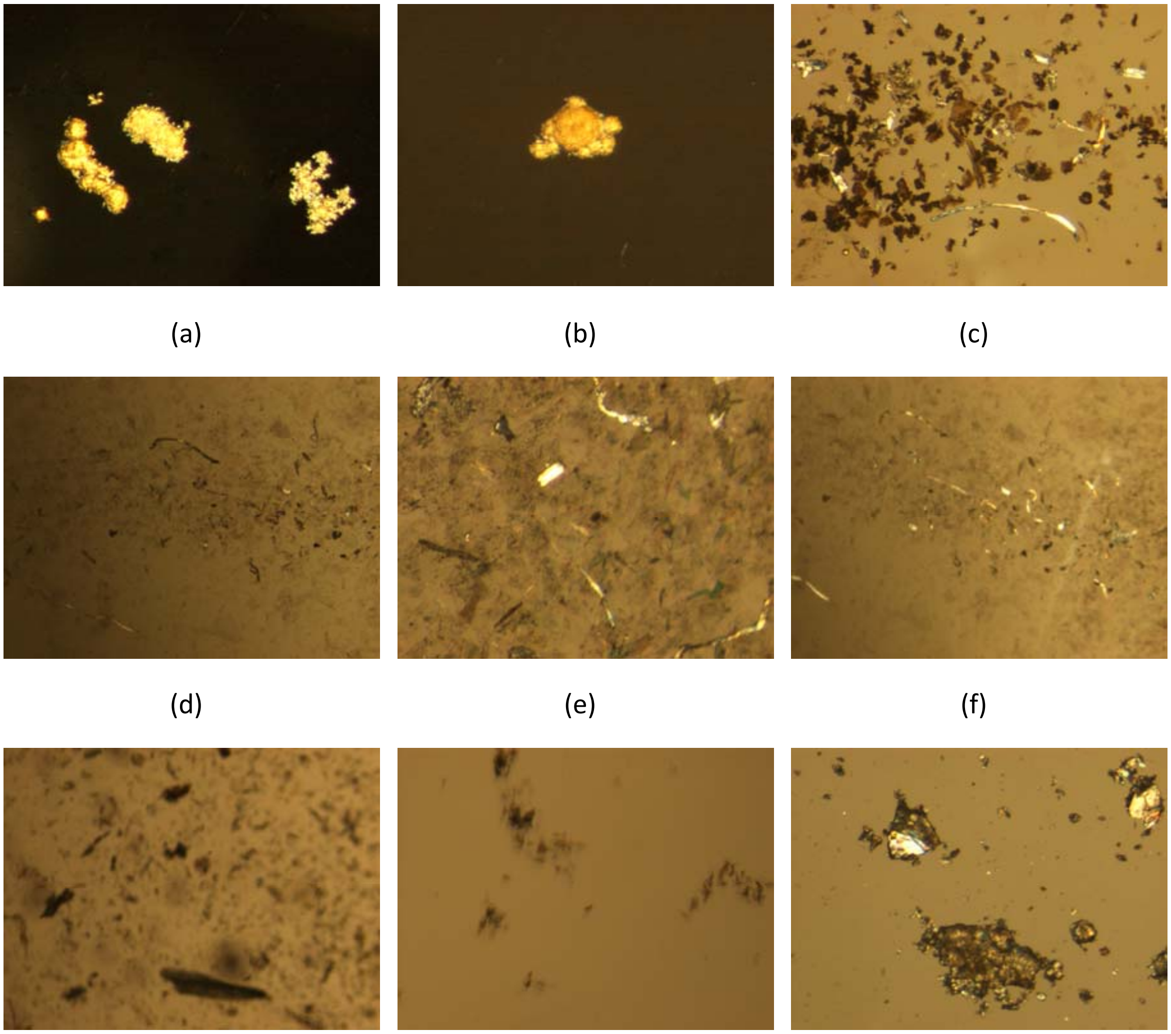

(a) (b) (c)

(d) (e) (f)

(g) (h) (i)

Figure 37| (a-c) Aspect of the product of the reaction of Cd(II), AdeH and RGD, (d-f) SucRGD at pH 5 and (g) RGD at pH 5.6 and (h) pH 6. (i) Control assay using same protocol as Yang *et al.* [104].

For these cases there was no formation of agglomerates of spherical structures and only amorphous solids deposited or at the surface could be seen (Figure 37g,h). As expected, the control experiment resulted in abundant number of crystals, believed to be of the 2D trinuclear Cd(II)-complex with adenine nucleobase described by Yang *et al.* [104].

The products from reaction assays P15A to P17B were further analyzed by SEM-EDS and results can be seen in Figure 39 and Figure 38.

The globular structures that resulted from P15A were actually formed by an agglomerate of spherical structures, as can be seen by the images captured by SEM analysis. After the solvent evaporation over a glass slide, it was already possible to see crystal like structures, though attributed to crystals of the metal salt only. Interestingly EDS elemental analysis revealed areas where Cd co-localizes with C, O and N, namely at zones Z2 (Figure 38a,e) and Z3 (Figure 38a,f).

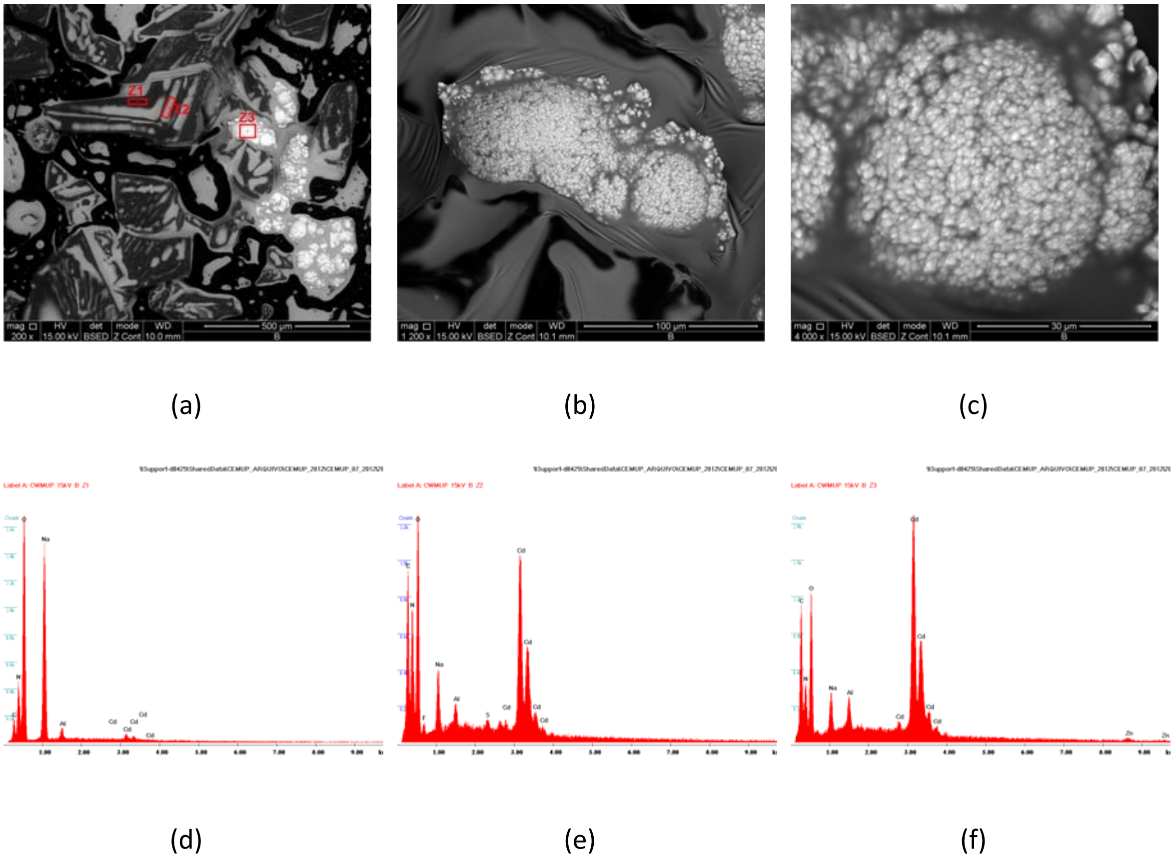

(a) (b) (c)

(d) (e) (f)

Figure 38| (a-c) SEM images of the product of the reaction of Cd(II), AdeH and RGD (P15A), after total evaporation of solvent, and EDS spectrum for distinct zones (d) Z1, (e) Z2 and (f) Z3 identified in the material.

These results can be interpreted by admitting the successful formation of the complex [Cd(AdeH)(RGD)], which could be found in zones as Z2 in crystal like structures. Further characterization of these potential crystals need to be done by X-ray diffraction in order to confirm the presence of the complex.

SEM images from P17B reaction product show a cell like formation with portions of material layered over each other (Figure 39). The composition is heterogeneous as it can be observed by the different color intensity and confirmed by EDS analysis. For zone Z1 (Figure 39a), composition analysis reveals co-localization of elements such as C, O, N - which can be from the peptide and the nucleobase – and Cd (Figure 39d). For zone Z2 (Figure 39a) the presence of N and O is not as strong as in Z1, and the Cd peak is also much less intense than in Z1 (Figure 39e).

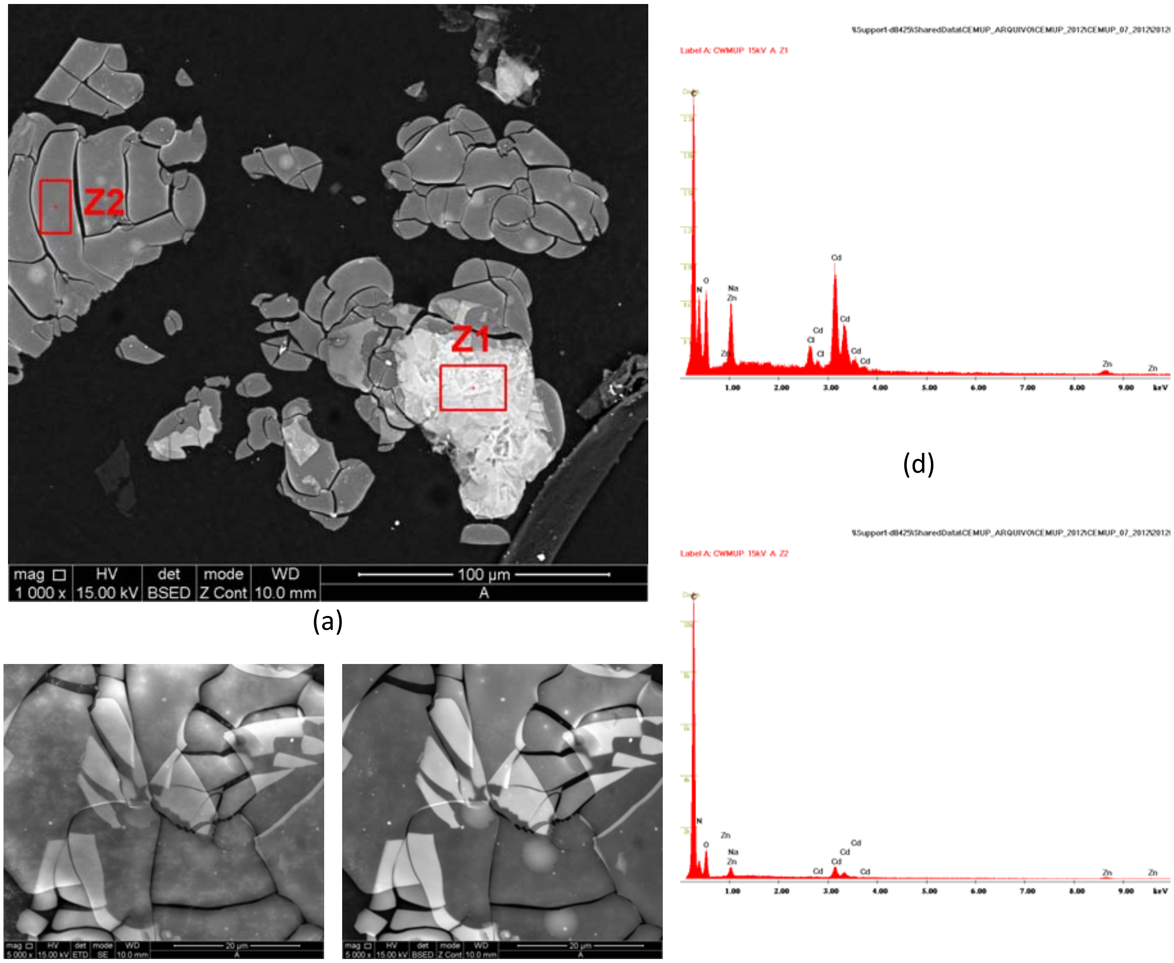

(a)

(b)

(c)

(d)

(e)

Figure 39| (a-c) SEM images of the product of the reaction of Cd(II), AdeH and RGD (P17B), after total evaporation of solvent, and EDS spectrum for zone (d) Z1 and (e) Z2 identified in the material.

Additionally in both EDS spectrums it is possible to notice the presence of Zn, possibly as a contaminant from previous synthesis where the same Teflon autoclaves were used. These structures are apparently not crystalline, though it is considered the possibility of the presence of the complex [Cd(AdeH)(RGD)] in zone Z1, given its elemental composition.

3.4. FTIR Spectra of Lyophilized Samples

Figure 40 shows a representative IR spectra of the pure RGD peptide (black full line), and the product of synthesis trials P7A-E (Table 6). Solutions that resulted from P7A-E assays were lyophilized in order to obtain a dry solid suitable for FTIR-ATR analysis.

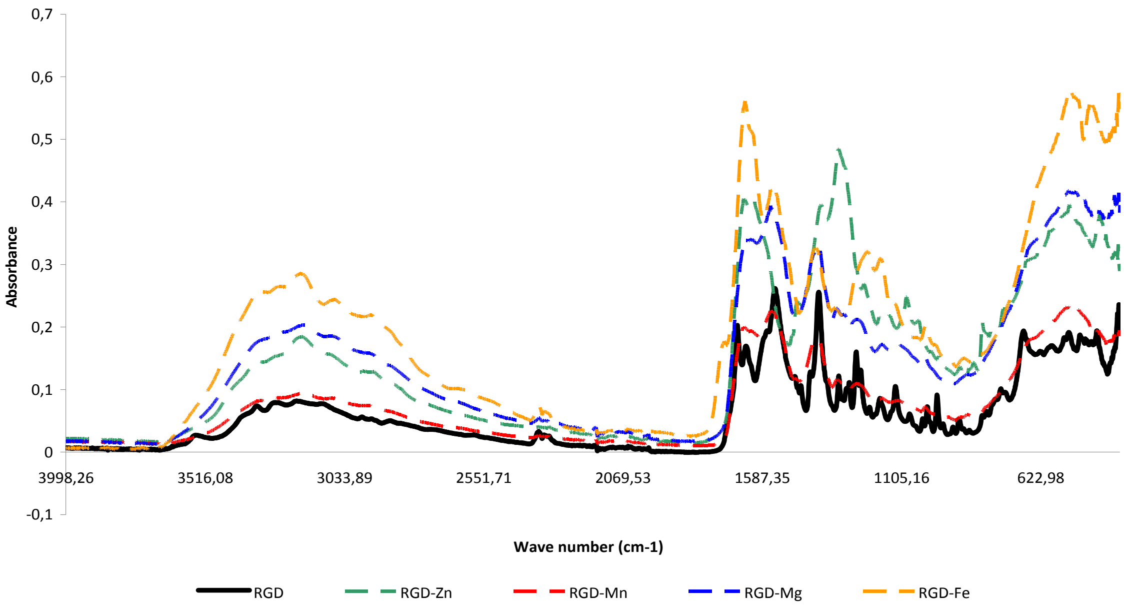

Figure 40| IR spectra of pure RGD and the product of reaction of RGD and Zn(II), Mn(II), Mg(II) and Fe(II) (Table 6, P7A-E)

The inspection of the IR spectra of RGD and its potential metal complexes, is based on some general references [133, 134] and made in comparison with other related molecules and complexes. Table 8 shows the measured IR bands positions of the pure RGD peptide and the products of reactions between RGD and four metals Zn(II), Mn(II), Mg(II) and Fe(II).

The bands at wavenumber 1260 cm^{-1} for the RGD peptide can be attributed to C-O stretching vibrations either from both Asp carbonyl terminal group and side chain. Shift in this band for Zn(II)-RGD and Fe(II)-RGD suggest the participation of the C-O group in the complex formation.

Table 8| IR assignment (4500 – 300 cm^{-1}) of RGD and products of reaction of P7A-E assays.

	υ(C-O)	υ(C=O)	$\upsilon_s(COO^-)$	$\upsilon_{as}(COO^-)$	δ(COH)	$\delta(NH_2)$	$\upsilon_s(CN_3H_5^+)$	$\upsilon_{as}(CN_3H_5^+)$	Amide I υ(C=O)	Amide II δ(N-H) + υ(C-N)	υ(M-O) [134]	υ(M-N) [134]
Asp (side chain) [133]	1120-1250	1716-1760	1402	1574-1579	1264-1450							
Arg (side chain) [133]							1633-1636	1672-1673				
RGD	1260 m		1417 sh 1389 s	1570 sh	1324 w	1541 s	1641 m	1672 s	1630 sh	1541 s	522 w	422 w
Zn(II)-RGD	1229 sh		1401 s	1623 w	1318 vs		1648 s		1618 sh		521 s	415 s
Mn(II)-RGD	1256 w		1391 s		1328 w	1554 s	1646 w		1623 sh	1554 s	517 m	
Mg(II)-RGD	1251 m		1387 s		1326 w	1550 s	1630 w		1618 sh	1550 s	511 s	415 w
Fe(II)-RGD	1223 s	1720 sh	1382 s	1620 sh	1338 w	1541 s	1646 vs		1623 sh	1541 s	520 vs	447 s

δ - in plane bending vibration, υ - stretching vibration, υ_s – symmetric stretching vibration, υ_s – antisymmetric stretching vibration, s – band of strong intensity, sh – shoulder, m – band of medium intensity, vs – band of very strong intensity, w – band of weak intensity

Band for Fe(II)-RGD at 1720 cm^{-1}, which can be assigned to C=O stretching, appears only for this product, what can indicate the intervention of this bond in the coordination of RGD with Fe(II) and not with any of the other tested metals.

A slight shift can be noticed for band at wavenumber 1389 cm^{-1} for RGD and Zn(II)-RGD which can be assigned for symmetric stretching of COO^- (deprotonated COOH). Also a shoulder type band at wavenumber 1570 cm^{-1} for RGD suffered a shift to higher frequencies of 1623 cm^{-1} and 1620 cm^{-1} for Zn(II)-RGD and Fe(II)-RGD respectively. The shifting in these bands seems to confirm a major role of COOH groups in the complexation reaction.

Very slight shifts can be observed for RGD bands that can be assigned to COH bending vibrations namely for Fe(II)RGD and NH_2 bending vibrations, namely Mn(II)-RGD and Mg(II)-RGD. For bands that can be assigned to Arg side chains stretching vibrations $\upsilon_s(CN_3H_5^+)$ no major shifts can be noted, but for the band with wavenumber 1672 cm^{-1} for RGD which possibly corresponds to $\upsilon_{as}(CN_3H_5^+)$ one can notice its disappearance for all the potential metal complexes. Though, this observation can be a misinterpretation of this particular band of the spectrum, once at this wavenumber also C=O stretch from amide I connections can be assigned.

No major shifts can be observed for amide I and II vibrations. Amide I vibrations are mostly related to C=O stretching and is directly related to peptide backbone conformation. Once no significant difference is noted from spectrum of RGD and Metal-RGD, it is possible to admit that no changes happened in the conformation of the peptide after the reaction with the metal. The lack of shifting in the band that can correspond to amide II can also confirm that the peptide maintained its original conformation after reacting with the metal.

Finally, based on data reported for $[Cu(Gly)_2]$ and $[Cu(Ala)_2]$ complexes [135] it is possible to suppose interactions between the metals and the peptide by looking for shifts in lower frequency bands. In this zone of the spectrum it is possible to see the augmented intensity for RGD band that can be assigned to M-O stretching vibrations, that happens when a metal is coordinated to peptide. Despite no major frequency shifts can be seen for this band, a very strong intensity band for Fe(II)-RGD and strong intensity band for Zn(II)-RGD and Mg(II)-RGD can be attributed to the interaction of the metal ion and the hydroxylate moieties of the peptide [134]. A minor intensity change can also be observed for bands that can be assigned to M-N stretching vibrations. Again an increase of band intensity from RGD (weak 422 cm^{-1}) to Zn(II)-

RGD (strong 415 cm^{-1}) and Fe(II)-RGD (strong 447 cm^{-1}) can be noticed, suggesting a possible interaction between the amine moieties and the Zn(II) and Fe(II) cations.

Therefore, in general the IR spectra suggest probable interactions either involving the metal ions and the deprotonated carboxyl and amino groups of RGD. Here Zn(II)-RGD and Fe(II)-RGD show the most significant band shifting for the assignments that well represent these type of interactions.

3.5. Molecular Dynamics Simulations

The developed computational protocol allowed a preliminary analysis of the interaction preferences between the motif Arg-Gly-Asp (RGD) and Zn(II). The defined 40 Å cubic simulation cell comprehends 100 RGD and 100 Zn units. Figure 41 represents a visualization of the simulation cell using VMD software [136].

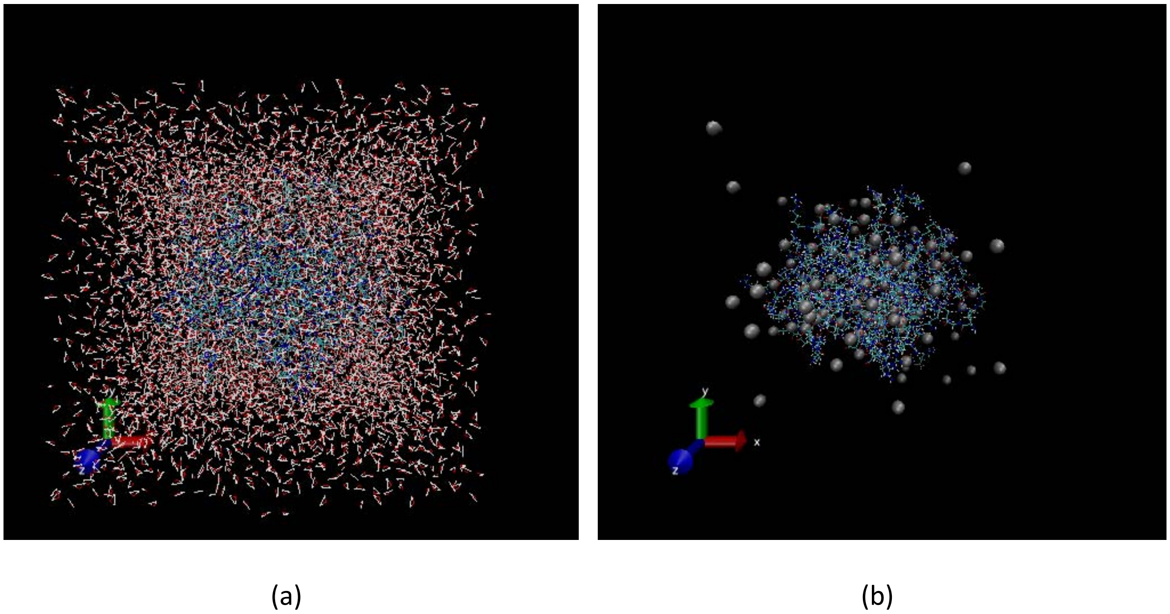

(a) (b)

Figure 41| (a) Graphical aspect of the simulation cell, where solvent is represented and (b) hidden from visualization ([136])

The simulation allowed to collect qualitative graphical data, such as the preferred coordination types between Zn(II), the C and N terminus of RGD backbone and the side chain groups of Asp and Arg. It is also possible to observe the bridging between two metal ions via one RGD ligand and the tendency to framework formation, in which the ligands connect consecutive Zn(II) atoms. Additionally, quantitative data about the evolution of the distances, during the simulation time, between the interacting atoms could also be obtained.

Pymol [137] starting structure for the RGD motif is represented in Figure 42, where the atom labels can be seen.

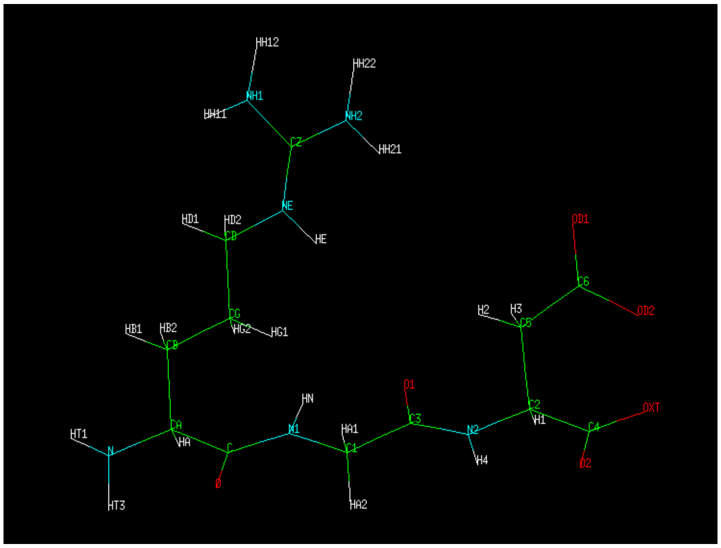

Figure 42| RGD motif atom labeling

3.5.1. Qualitative graphical analysis

Figure 43 illustrates the type of interactions that can be observed for the simulated system. In this representation tree Zn(II) atoms (residues 132, 150, 156, 174, 179 and 194) are connected in a cluster through a set of RGD residues The interactions are listed in Table 9

Table 9| Interactions based on six Zn(II) residues

Zn Residue ID	RGD Residue ID	Interacting atoms
132	55	OD1, O1
150	37	N
156	79	OD1, OD2, O, O1
174	20	N
	34	OD1, OD2
	37	OD2
	79	O2, OXT
179	37	O2, OXT
	20	O2, OXT
194	34	O2, OXT
	55	O2, OXT

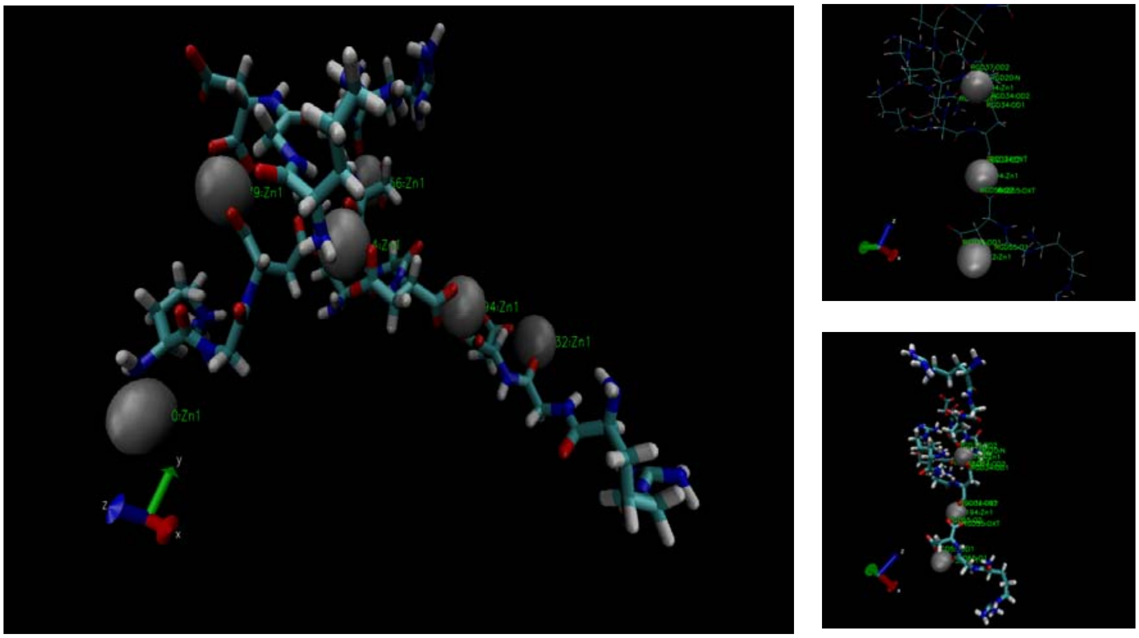

Figure 43| Representation of a cluster of interacting Zn(II) and RGD residues

From this portion of the system one can confirm that the RGD coordinates Zn(II) ions not just by the more probable carboxylate C terminal group (OXT, O2), but also through the carboxylate side chain of Asp (OD1, OD2), the O (O1) from the backbone and through the N terminal (N). It is interesting to see RGD residues acting as bridges between Zn(II) atoms, as the case of RGD residues 20, 34, 37 and 55. RGD residue 20 coordinates two different Zn(II) residues (174, 179), through both its C an N terminal (O2, OXT and N), while RGD 37 also coordinates the same Zn(II) residues via its N terminal but alternatively through the Asp side chain carboxylate (OD2). As these type of interactions are expected to occur in order for an ordered framework to form, it is considered that these preliminary data builds up for a probable RGD and Zn(II) based Metal Organic Framework.

3.5.2. Quantitative analysis – Interaction Distances

Studying the evolution of the distances, between the interacting atoms during the simulation time, gives information about the preferred interactions.

From Figure 44 and Figure 45 it is possible to note that for all interactions there is a maximum round 2.0 Å. For Figure 44 the prevalent orange line corresponds to interactions between the solvent H_2O molecules and the Zn(II) atoms which move to the solvent bulk and get surrounded by H_2O.

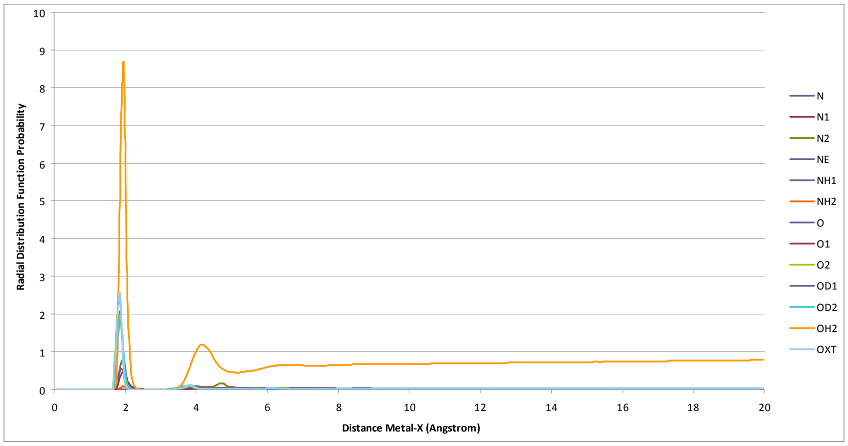

Figure 44| Average distances from interacting atoms of RGD and solvent H2O to Zn(II)

Figure 45 is similar to Figure 44 but the line for the solvent was removed, allowing an adjustment of scale

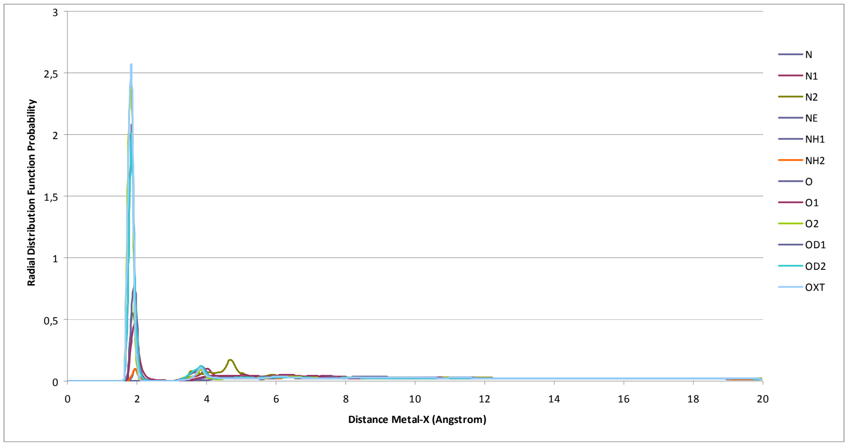

Figure 45| Average distances from interacting atoms of RGD to Zn(II)

Figure 46 represents a detail from Figure 45, where it is possible to see the prevalent interactions. These are: (1) The metal-OXT and metal O2 – from the carboxylate C-terminal from Asp; (2) The metal-OD2 and metal-OD1 – almost equivalent between them as expected for the Asp side chain carboxylate group. These four type of interactions are dominant and present an interaction maximum around 1,85 Å; (3) N atom – from the N-terminal of Arg – and the O atom

– from the carbonyl backbone of Arg – with a similar probability between them, though the average distances of interaction are higher for N; (4) N1 and N2 - from backbone - and NE - from Arg side chain are almost null until close to 3 Å

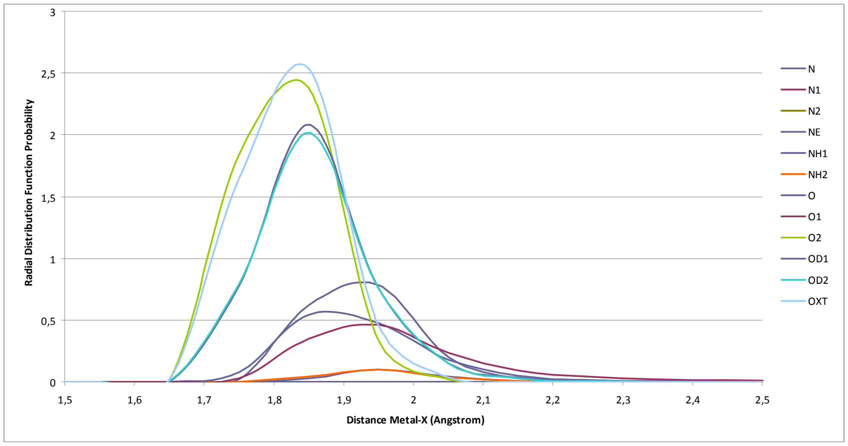

Figure 46| Detail from average distances from interacting atoms of RGD to Zn(II)

Figure 47 represents the accumulated total number of interactions as a function of distance. The number of interactions is null until close to 2,0 Å and increases progressively. For some interactions the value of distance is null until close to 3,0 Å as for N1, N2 and NE atoms.

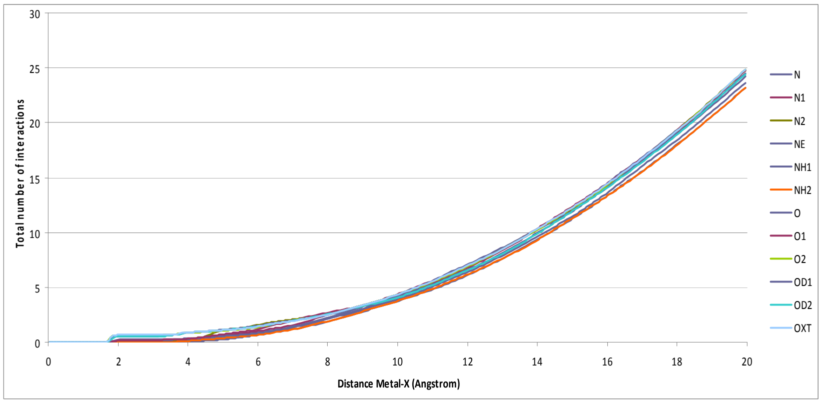

Figure 47| Accumulated total number of interactions as a function of distance

A detailed representation of the above figure can be seen in Figure 48

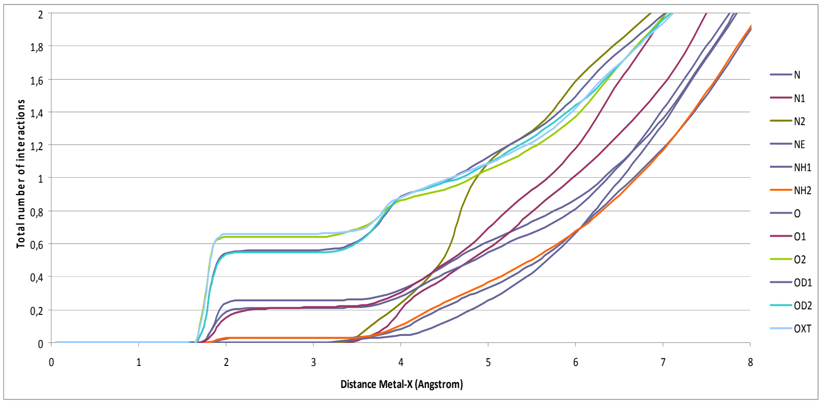

Figure 48| Accumulated total number of interactions as a function of distance detailed perspective

From the analysis of Figure 48 it is possible to confirm what was revealed in Figure 45 and Figure 46, and this is that the most prevalent interaction is the Metal-OXT, with a interacting distance of 1.85 Å, which corresponds to an accumulated number of 0.65 interactions of Zn-OXT.

4. CONCLUSIONS

With this project we started a quest for a novel kind of molecular vehicle. Until present the reports on MOFs built from biocompatible metals and peptides are scarce and to my knowledge none has explored the capacity of specific delivery by using cell receptor directing aminoacid sequences. Work has been done regarding the synthesis and characterization of a complex formed between the RGD peptide and diverse transition metals, where Fe(II), Zn(II) and Cu(II) deserved more attention. One of the major challenges found, that is important to refer, is the high cost of the commercial RGD peptide, which limits the quantity of material available for experiments, forcing the use of reduced reaction volumes (< 100 µl) in order to get significant concentrations of this precursor in solution.

Diverse conditions of synthesis were tested such as solvothermal, non-solvothermal and sonochemical synthesis, temperature protocols, the nature and quantity of metal and peptide precursors, solvents, total volume of reaction and initial reaction pH. Nevertheless, the number of variable parameters in this system may require high-throughput (HT) methods for solvothermal synthesis. These are accepted as a powerful tool to accelerate the discovery of new compounds, once large amounts of data are generated that allows one to establish crystallization fields and to extract relevant reaction trends. This in turn can contribute to a better understanding of the role of individual reaction parameters on the product formation.

The formation of the complex was tested by spectroscopic techniques such as FTIR and CD, though optimization in sample preparation is needed to allow an efficient interpretation of the resulting data. Despite results are not conclusive, FTIR analysis of samples P7A-E shows characteristic band shifts typically observed upon cation coordination. Also SEM-EDS analysis revealed co-localization of organic (C; N; O) and inorganic (metal) of some products of synthesis (P10A and P17).

Crystallization trials were explored with the purpose of obtaining diffracting crystals. Although all attempts had revealed unsuccessful it is possible to conclude from the assays done, that the control of the reaction pH is a fundamental issue and efforts need to be done in order to allow pH measurement and setting in micro volumes of reaction. The failure in obtaining crystals from the complex can be attributed to the large number of possible site interactions between the RGD and the metal, that depending of the reaction pH, can reach to twelve atoms. In order to limit the available sites, reaction pH should be set and potentially controlled during the time of reaction, a procedure that can represent a tough challenge for small volumes and high temperature synthesis.

Molecular dynamics simulations, though in a preliminary state for this system, had revealed interesting results and build more confidence in the chance of getting a metal- RGD MOF. Simulations revealed RGD ligands acting as a bridge between Zn(II) atoms, coordinating the metal trough not only its C and N terminal, but also with O and N atoms from Asp and Arg side chains respectively. Moreover it is possible to observe saturated coordination spheres for Zn(II), where the metal is commonly found tetra, penta and hexa-coordinated to up four different RGD residues. This behavior can suggest the formation of a complex 3D framework.

5. FUTURE PROSPECTS

The large amount of variables in play when synthesizing and crystallizing MOFs, and the fact that this is a relatively new area of research, leads to an extremely wide field of exploration. Therefore there is the need to experiment different reaction conditions as the pH, the quantities and stoichiometry of precursors, temperature profiles, volume, type of solvent, use of coligands. Also the crystallization methods that can be used are diverse. In the particular case of the RGD based MOFs it is also necessary to find other methods besides the ones used in this work (FTIR, SEM-EDS) that could confirm the formation of the complexes with metals. An ideal method should turn possible to follow the complexation reaction and reveal reaction parameters (K, kinetics, order). UV-Vis methods should be tried and optimized for this task.

One of the most important aspects that should deserve great attention the development of speciation studies for the RGD peptide. These studies may turn possible the selection of the interacting atoms available for metal coordination, by adjusting the reaction pH. These studies can also reveal preferential coordination sites that could lead to the formation of a porous framework with pre-determined architecture.

Recently, when working with mixed ligands (adenine and RGD) it was possible to identify (as referred in section 3.3.4) what can possibly be crystals of the complex [Cd(Ade)(RGD)]. Though, these crystals were not analyzed in the X-ray diffractometer once the equipment at IBMC got out of service due to malfunctioning, thus this task will be attained as soon as possible.

5.1. *In vitro* and *in vivo* assays

After the successful synthesis of the RGD based MOF, its capacity to uptate drug molecules in its pores will be tested using for example the model molecule Ibuprofen. Also evaluation of drug release kinetics at physiological conditions should be tested. Additionally, drug loaded MOFs should be tested for *in vitro* citotoxicity and binding assays. Finally, evaluation of toxicity and antitumour effect in human xenograft models should be performed

5.2. Computational Methods

Computational Methods protocols outlined in 2.2.7 are already being extended to study:

(1) The Influence of the Number of Metal Atoms (100 RGD + 200 Zn(II) and 100 RGD + 400 Zn(II)). Both attempts to simulate these systems failed, due to the high positive charges of the systems. Attempts to minimize the problem by the introduction of additional minimization and equilibration steps in the protocol did not change the outcome. The protocol could be improved by the addition of counter-ions (Cl^-), a typical procedure when running Molecular Dynamics simulations. However, the high number of Cl^- present could affect the validity of the study for the objectives here proposed. Nevertheless, this remains the best option, to be discussed in the future.

(2) The Influence of the Number in the Size of the Simulation Cell. The preliminary simulation cell, described in A, is based in packmol distribution of 100 RGD + 100 Zn(II) within a 40 Å cell. By increasing this cell the initial spaces between molecules would be higher, favoring a conformational rearrangement in regard to the initial structure. The test the possible impact of such effect, steps 2.2.7.1 and 2.2.7.3 were repeated starting with a simulation cell of 100 Å prepared with packmol for the same 100 RGD + 100 Zn(II) units. Upon solvation, this system reached a total number of 183,346 atoms (7 times bigger than the previous system, with 25,712 atoms). 10 ns MD simulations were attempted at 298 K. The simulation crashed due to unrelated problems in the server. This simulation is under reconsideration.

6. REFERENCES

1. Della Rocca, J., D. Liu, and W. Lin, *Nanoscale metal-organic frameworks for biomedical imaging and drug delivery.* Accounts of chemical research, 2011. **44**(10): p. 957-68.
2. Lee, H.-Y., et al., *Covalent Metal–Peptide Framework Compounds That Extend in One and Two Dimensions.* Crystal Growth & Design, 2007. **8**(1): p. 296-303.
3. Rabone, J., et al., *An adaptable peptide-based porous material.* Science, 2010. **329**(5995): p. 1053-7.
4. Horcajada, P., et al., *Porous metal-organic-framework nanoscale carriers as a potential platform for drug delivery and imaging.* Nature materials, 2010. **9**(2): p. 172-8.
5. Murphy, E.A., et al., *Nanoparticle-mediated drug delivery to tumor vasculature suppresses metastasis.* Proceedings of the National Academy of Sciences of the United States of America, 2008. **105**(27): p. 9343-8.
6. Temming, K., et al., *RGD-based strategies for selective delivery of therapeutics and imaging agents to the tumour vasculature.* Drug resistance updates : reviews and commentaries in antimicrobial and anticancer chemotherapy, 2005. **8**(6): p. 381-402.
7. Clearfield, A., Prog. Inorg. Chem., 1998. **47**: p. 371.
8. Eddaoudi, M., et al., Acc. Chem. Res., 2001. **34**: p. 319.
9. Férey, G., et al., Acc. Chem. Res., 2005: p. 317.
10. Férey, G., Chem. Soc. Rev., 2008. **37**: p. 191.
11. Janiak, C. and J.K. Vieth, *MOFs, MILs and more: concepts, properties and applications for porous coordination networks (PCNs).* New Journal of Chemistry, 2010. **34**(11): p. 2366-2388.
12. Hoskins, B.F. and R. Robson, J. Am. Chem. Soc., 1989. **111**: p. 5962.
13. O. M. Yaghi, H.L., *Hydrothermal Synthesis of a Metal-Organic Framework Containing Large Rectangular Channels.* J. Am. Chem. Soc., 1995. **117**: p. 10401-10402.
14. Chizallet, C., et al., J. Am. Chem. Soc., 2010. **132**: p. 12365.
15. Dang, D.B., et al., J. Am. Chem. Soc., 2010. **132**: p. 14321.
16. Fei, H.H., D.L. Rogow, and S.R.J. Oliver, J. Am. Chem. Soc., 2010. **132**: p. 7202.
17. Shimomura, S., et al., Nat. Chem., 2010. **2**: p. 633.
18. Lamia, N., et al., Chem. Eng. Sci., 2009. **64**: p. 3246.
19. Bae, T.H., et al., Angew. Chem., Int. Ed., 2010. **49**: p. 9863.
20. Gascon, J. and F. Kapteijn, Angew. Chem., Int. Ed., 2010. **49**: p. 1530.
21. Ameloot, R., et al., Chem. Commun., 2010. **46**: p. 3735.
22. Horcajada, P., et al., Adv. Mater. (Weinheim, Ger.), 2009. **21**: p. 1931.
23. Pereira, G.A., et al., Inorg. Chem., 2010. **49**: p. 2969.
24. Seo, J.S., et al., Nature, 2000. **404**: p. 982.
25. Ryu, D.W., et al., Chem. Commun., 2010. **46**: p. 8779.
26. Tian, H., et al., Chem. Commun., 2010. **46**: p. 5349.
27. Tong, X.L., et al., Chem. Commun., 2010. **46**: p. 8543.
28. Maspoch, D., D. Ruiz-Molina, and J. Veciana, J. Mater. Chem., 2004. **14**: p. 2713.
29. Horcajada, P., et al., *Metal-organic frameworks in biomedicine.* Chemical Reviews, 2012. **112**(2): p. 1232-68.
30. Gould, J.A., et al., *A homochiral three-dimensional zinc aspartate framework that displays multiple coordination modes and geometries.* Chemical communications, 2010. **46**(16): p. 2793-5.
31. Mantion, A., et al., *Metal-peptide frameworks (MPFs): "bioinspired" metal organic frameworks.* Journal of the American Chemical Society, 2008. **130**(8): p. 2517-26.

32. Horcajada, P., et al., *Metal–Organic Frameworks in Biomedicine.* Chemical Reviews, 2011. **112**(2): p. 1232-1268.
33. Kitagawa, S., R. Kitaura, and S.H. Noro, Angew. Chem., Int. Ed., 2004. **43**: p. 2334.
34. Férey, G. and C. Serre, Chem. Soc. Rev., 2009. **38**: p. 1380.
35. Eddaoudi, M., et al., Science, 2002. **295**: p. 469.
36. Li, J.R., et al., Chem.—Eur. J., 2008. **14**: p. 2771.
37. Devic, T., et al., J. Am. Chem. Soc., 2010. **132**: p. 1127.
38. Horcajada, P., et al., *Flexible porous metal-organic frameworks for a controlled drug delivery.* Journal of the American Chemical Society, 2008. **130**(21): p. 6774-80.
39. Davis, M.E., Z.G. Chen, and D.M. Shin, *Nanoparticle therapeutics: an emerging treatment modality for cancer.* Nature reviews. Drug discovery, 2008. **7**(9): p. 771-82.
40. Dyson, P.J. and G. Sava, *Metal-based antitumour drugs in the post genomic era.* Dalton transactions, 2006(16): p. 1929-33.
41. Grulke, C.M., M.R. Goldsmith, and D.A. Vallero, *Toward a blended ontology: applying knowledge systems to compare therapeutic and toxicological nanoscale domains.* Journal of biomedicine & biotechnology, 2012. **2012**: p. 308381.
42. Cho, K., et al., *Therapeutic nanoparticles for drug delivery in cancer.* Clinical cancer research : an official journal of the American Association for Cancer Research, 2008. **14**(5): p. 1310-6.
43. Peer, D., et al., *Nanocarriers as an emerging platform for cancer therapy.* Nature nanotechnology, 2007. **2**(12): p. 751-60.
44. Alexis, F., et al., *Factors affecting the clearance and biodistribution of polymeric nanoparticles.* Molecular pharmaceutics, 2008. **5**(4): p. 505-15.
45. Ferrari, M., *Cancer nanotechnology: opportunities and challenges.* Nature reviews. Cancer, 2005. **5**(3): p. 161-71.
46. Li, S.D. and L. Huang, *Pharmacokinetics and biodistribution of nanoparticles.* Molecular pharmaceutics, 2008. **5**(4): p. 496-504.
47. Sanhai, W.R., et al., *Seven challenges for nanomedicine.* Nature nanotechnology, 2008. **3**(5): p. 242-4.
48. Sundaram, P., J. Wower, and M.E. Byrne, *A nanoscale drug delivery carrier using nucleic acid aptamers for extended release of therapeutic.* Nanomedicine : nanotechnology, biology, and medicine, 2012.
49. Huxford, R.C., J. Della Rocca, and W. Lin, *Metal-organic frameworks as potential drug carriers.* Current opinion in chemical biology, 2010. **14**(2): p. 262-8.
50. Skoog, D.A., D.M. West, and F.J. Holler, *Fundamentals of analytical chemistry*. 7th ed. Saunders golden sunburst series1996, Fort Worth: Saunders College Pub.
51. Jones, L. and P.W. Atkins, *Chemistry : molecules, matter, and change*. 4th ed2000, New York: W.H. Freeman.
52. Roat-Malone, R.M., *Bioinorganic chemistry : a short course*2002, Hoboken, N.J.: Wiley. xvii, 348 p.
53. Imaz, I., et al., *Metal-biomolecule frameworks (MBioFs).* Chemical communications, 2011. **47**(26): p. 7287-302.
54. Rang, H.P., Dale, M. M., Ritter, J. M., Moore, P. K., *Pharmacology*. Fifth Edition ed2003, London: Churchill Livingstone.
55. Dietzel, P.D.C., R. Blom, and H. Fjellvag, Eur. J. Inorg. Chem., 2008. **23**: p. 3624.
56. Horcajada, P., et al., Chem. Commun., 2007: p. 2820.
57. An, J., S.J. Geib, and N.L. Rosi, J. Am. Chem. Soc., 2009. **131**: p. 8376.
58. Vimont, A., et al., J. Am. Chem. Soc., 2006. **128**: p. 3218.

59. McKinlay, A.C., et al., J. Am. Chem. Soc., 2008. **130**: p. 10440.
60. Horcajada, P., et al., Angew. Chem., Int. Ed., 2006. **45**: p. 5974.
61. Keskin, S. and S. Kizilel, Ind. Eng. Chem. Res., 2011. **50**(4): p. 1799.
62. Imaz, I., et al., Chem Commun., 2011. **47**: p. 7287.
63. Weber, R. and G. Bergerhoff, Z. Kristallogr., 1991. **195**: p. 878.
64. Serre, C., et al., Dalton Trans., 2008: p. 5462.
65. Serre, C., et al., Angew. Chem., Int. Ed., 2004. **43**: p. 6286.
66. Afonso, R., A. Mendes, and L. Gales, *Peptide-based solids: porosity and zeolitic behavior.* Journal of Materials Chemistry, 2012. **22**(5): p. 1709-1723.
67. Couvreur, P. and V. Vauthier, Pharm. Res., 2006. **23**: p. 1417.
68. Fattal, E., et al., Antimicrob. Agents Chemother, 1989. **33**: p. 1540.
69. Qiu, L.Y. and Y.H. Bae, Pharm. Res., 2006. **23**(1): p. 1.
70. Peer, D., et al., Nature Nanotechnol., 2007. **2**: p. 751.
71. Férey, G., et al., Angew. Chem., Int. Ed., 2004. **43**: p. 6296.
72. Imaz, I., et al., *Metal-biomolecule frameworks (MBioFs).* Chemical communications, 2011. **47**(26): p. 7287-7302.
73. Horcajada, P., et al., Nat. Mater., 2010. **9**: p. 172.
74. Taylor-Pashow, K.M.L., et al., J. Am. Chem. Soc., 2009. **131**: p. 14261.
75. Yamauchi, O., A. Odani, and M. Takani, *Metal-amino acid chemistry. Weak interactions and related functions of side chain groups.* Journal of the Chemical Society, Dalton Transactions, 2002(18): p. 3411-3421.
76. Lehninger, A.L., D.L. Nelson, and M.M. Cox, *Lehninger principles of biochemistry*. 4th ed2005, New York: W.H. Freeman.
77. Saunders, C.D.L., et al., *Preparation and Comprehensive Characterization of [Hg6(Alanine)4(NO3)4]·H2O.* Inorganic chemistry, 2008. **47**(9): p. 3693-3699.
78. Ch'ng, C.D., et al., *catena-Poly[[[diaquanickel(II)]-di-[mu]-glycine] dichloride].* Acta Crystallographica Section E, 2008. **64**(7): p. m865-m866.
79. Stenzel, K. and M. Fleck, *Poly[[[diaquacobalt(II)]-di-[mu]-glycine] dichloride].* Acta Crystallographica Section E, 2004. **60**(10): p. m1470-m1472.
80. Xie, Y., et al., *rac-Poly[bis([mu]-tryptophanato)manganese(II)].* Acta Crystallographica Section E, 2006. **62**(9): p. m2089-m2090.
81. Wang, J., et al., *rac-catena-Poly[nickel(II)-di-[mu]-tryptophanato].* Acta Crystallographica Section E, 2007. **63**(11): p. m2867-m2868.
82. Schveigkardt, José M., et al., *Structural and Single Crystal EPR Studies of the Complex Copper L-Glutamine: A Weakly Exchange-Coupled System with syn-anti Carboxylate Bridges.* European Journal of Inorganic Chemistry, 2002. **2002**(11): p. 2913-2919.
83. Strasdeit, H., et al., *Syntheses and Properties of Zinc and Calcium Complexes of Valinate and Isovalinate: Metal α-Amino Acidates as Possible Constituents of the Early Earth's Chemical Inventory.* Chemistry – A European Journal, 2001. **7**(5): p. 1133-1142.
84. Glowiak, T. and Z. Ciunik, *Two crystal structures of polymorphic bis(glycine)manganese(II) bromide dihydrate.* Acta Crystallographica Section B, 1978. **34**(6): p. 1980-1983.
85. Ashmead, S.D., *The chemistry of ferrous bis-glycinate chelate.* Archivos latinoamericanos de nutricion, 2001. **51**(1 Suppl 1): p. 7-12.
86. J. B. Weng, M.C.H., R. Cao, Q. Shi and A. S. C. Chan, *The Paramagnetic 2D Chiral-porous Polymer of L-Phenylalanine and Manganese.* Chinese J. Struct. Chem., 2003. **22**: p. 195-199.

87. D. Vanderhe, M.B.L.a.E.L.E., Acta Crystallogr., Sect. B: Struct. Crystallogr. Cryst. Chem., 1971. **B27**: p. 2411-2418.
88. Antolini, L., et al., *Thermal, spectroscopic, magnetic, and structural properties of mixed-ligand complexes of copper(II) with L-aspartic acid and amines. Crystal and molecular structure of (L-aspartato)(imidazole)copper(II) dihydrate.* Inorganic chemistry, 1982. **21**(6): p. 2263-2267.
89. Flook, R.J., H.C. Freeman, and M.L. Scudder, *An X-ray and neutron diffraction study of aqua(l-glutamato)cadmium(II) hydrate.* Acta Crystallographica Section B, 1977. **33**(3): p. 801-809.
90. Gramaccioli, C., *The crystal structure of zinc glutamate dihydrate.* Acta Crystallographica, 1966. **21**(4): p. 600-605.
91. Mizutani, M., et al., *An infinite chiral single-helical structure formed in Cu(II)-l-/d-glutamic acid system.* Inorganica Chimica Acta, 1998. **283**(1): p. 105-110.
92. Zhang, Y., M.K. Saha, and I. Bernal, *[Cobalt(ii)l-glutamate(H2O)[middle dot]H2O][infinity]: a new 3D chiral metal-organic interlocking network with channels.* CrystEngComm, 2003. **5**(5): p. 34-37.
93. Ohata, N., H. Masuda, and O. Yamauchi, *Aromatic carboxylate-controlled self-organization of copper(II)–l-arginine complexes.* Inorganica Chimica Acta, 1999. **286**(1): p. 37-45.
94. Ohata, N., et al., *Unprecedented double helical structure highly self-organized through hydrogen bonds between copper(II)-coordinated l-Arginine and dicarboxylate motifs.* Journal of inorganic biochemistry, 1995. **59**(2–3): p. 721.
95. Ohata, N., H. Masuda, and O. Yamauchi, *Dianion-controlled supramolecular assembly of copper(II)-arginine complex ion.* Inorganica Chimica Acta, 2000. **300–302**(0): p. 749-761.
96. Takayama, T., et al., *Structural Analysis of Cadmium–Glycylglycine Complexes Studied by X-Ray Diffraction and High Resolution ¹¹³Cd and ¹³C Solid State NMR.* Bulletin of the Chemical Society of Japan, 1996. **69**(6): p. 1579-1586.
97. Tiliakos, M., et al., *Dipeptides containing the alpha-aminoisobutyric residue (Aib) as ligands: preparation, spectroscopic studies and crystal structures of copper(II) complexes with H-Aib-X-OH (X=Gly, L-Leu, L-Phe).* Journal of inorganic biochemistry, 2003. **93**(3-4): p. 109-18.
98. Ueda, E., et al., *New Bioactive Zinc(II) Complexes with Peptides and Their Derivatives: Synthesis, Structure, and In Vitro Insulinomimetic Activity.* Bulletin of the Chemical Society of Japan, 2004. **77**(5): p. 981-986.
99. Ferrari, R., et al., *Interaction between Glyglu and Ca2+, Pb2+, Cd2+ and Zn2+ in solid state and aqueous solution.: Crystal structures of poly[aqua-1,2-κ-O-di[lead(gly-gluH)]bis(perchlorate)] and poly[bisglycylglutamic-cadmium(II) tetrahydrate].* Inorganica Chimica Acta, 2002. **339**(0): p. 193-201.
100. Wang, X.-G., et al., *2-Aminobenzothiazole-based CdII complexes incorporating carboxylate-containing coligand: synthesis, crystal structure, and fluorescences.* Journal of Coordination Chemistry, 2012. **65**(13): p. 2353-2364.
101. Yang, E.-C., et al., *Four Novel Three-Dimensional Triazole-Based Zinc(II) Metal−Organic Frameworks Controlled by the Spacers of Dicarboxylate Ligands: Hydrothermal Synthesis, Crystal Structure, and Luminescence Properties.* Crystal Growth & Design, 2007. **7**(10): p. 2009-2015.

102. Wang, F. and Y. Kang, *Unusual cadmium(II)–adenine paddle-wheel units for the construction of a metal-organic framework with mog topology.* Inorganic Chemistry Communications, 2012. **20**(0): p. 266-268.
103. Sivakova, S. and S.J. Rowan, *Nucleobases as supramolecular motifs.* Chemical Society reviews, 2005. **34**(1): p. 9-21.
104. Yang, E.-C., et al., *The first 2D trinuclear Cd(ii)-complex with adenine nucleobase: hydrothermal synthesis, crystal structure and fluorescent properties.* New Journal of Chemistry, 2007. **31**(11): p. 1887-1890.
105. Hynes, R.O., *Integrins: bidirectional, allosteric signaling machines.* Cell, 2002. **110**(6): p. 673-87.
106. Pytela, R., M.D. Pierschbacher, and E. Ruoslahti, *Identification and isolation of a 140 kd cell surface glycoprotein with properties expected of a fibronectin receptor.* Cell, 1985. **40**(1): p. 191-8.
107. Alberts, B., *Molecular biology of the cell*. 4th ed2002, New York: Garland Science. xxxiv, 1548 p.
108. Xiong, J.P., et al., *Crystal structure of the extracellular segment of integrin alpha Vbeta3.* Science, 2001. **294**(5541): p. 339-45.
109. Mahalingam, B., et al., *Stable Coordination of the Inhibitory Ca2+ Ion at the Metal Ion-Dependent Adhesion Site in Integrin CD11b/CD18 by an Antibody-Derived Ligand Aspartate: Implications for Integrin Regulation and Structure-Based Drug Design.* The Journal of Immunology, 2011. **187**(12): p. 6393-6401.
110. Mould, A.P. and M.J. Humphries, *Regulation of integrin function through conformational complexity: not simply a knee-jerk reaction?* Current opinion in cell biology, 2004. **16**(5): p. 544-551.
111. Xiong, J.P., et al., *Crystal structure of the extracellular segment of integrin alpha Vbeta3 in complex with an Arg-Gly-Asp ligand.* Science, 2002. **296**(5565): p. 151-5.
112. Pierschbacher, M.D. and E. Ruoslahti, *Influence of stereochemistry of the sequence Arg-Gly-Asp-Xaa on binding specificity in cell adhesion.* The Journal of biological chemistry, 1987. **262**(36): p. 17294-8.
113. Bogdanowich-Knipp, S.J., et al., *Solution stability of linear vs. cyclic RGD peptides.* The journal of peptide research : official journal of the American Peptide Society, 1999. **53**(5): p. 530-41.
114. Goodman, S.L., et al., *Nanomolar small molecule inhibitors for alphav(beta)6, alphav(beta)5, and alphav(beta)3 integrins.* Journal of medicinal chemistry, 2002. **45**(5): p. 1045-51.
115. Dechantsreiter, M.A., et al., *N-Methylated cyclic RGD peptides as highly active and selective alpha(V)beta(3) integrin antagonists.* Journal of medicinal chemistry, 1999. **42**(16): p. 3033-40.
116. Merckserono. 22/6/2012]; Available from: www.merckserono.com.
117. ClinicalTrials.gov. 22/6/2012]; Available from: www.clinicaltrials.gov.
118. White, D.E., et al., *Targeted disruption of beta1-integrin in a transgenic mouse model of human breast cancer reveals an essential role in mammary tumor induction.* Cancer cell, 2004. **6**(2): p. 159-70.
119. Desgrosellier, J.S. and D.A. Cheresh, *Integrins in cancer: biological implications and therapeutic opportunities.* Nature reviews. Cancer, 2010. **10**(1): p. 9-22.
120. Ong, H.T., et al., *Intravascularly administered RGD-displaying measles viruses bind to and infect neovessel endothelial cells in vivo.* Molecular therapy : the journal of the American Society of Gene Therapy, 2009. **17**(6): p. 1012-21.

121. Cao, L., et al., *Enhancement of antitumor properties of TRAIL by targeted delivery to the tumor neovasculature.* Molecular cancer therapeutics, 2008. **7**(4): p. 851-61.

122. Dijkgraaf, I., et al., *Alpha v beta 3 integrin-targeting of intraperitoneally growing tumors with a radiolabeled RGD peptide.* International journal of cancer. Journal international du cancer, 2007. **120**(3): p. 605-10.

123. Luedtke, N.W. and Y. Tor, *A Novel Solid-Phase Assembly for Identifying Potent and Selective RNA Ligands We thank Professors David Wilson and David Boykin for a generous gift of the aromatic amidine derivatives and Professor Kol for a generous gift of eilatin-containing complexes. We are grateful to Dr. Georg Schlechtingen and Professor Murray Goodman for assistance with peptide synthesis and to Ibis Therapeutics for partial support. N.W.L. is supported by a National Institute of Health Molecular Biophysics Training Grant (GM 08326).* Angewandte Chemie, 2000. **39**(10): p. 1788-1790.

124. Wang, J., et al., *Automatic atom type and bond type perception in molecular mechanical calculations.* Journal of molecular graphics & modelling, 2006. **25**(2): p. 247-60.

125. Wang, J., et al., *Development and testing of a general amber force field.* Journal of computational chemistry, 2004. **25**(9): p. 1157-74.

126. Duan, Y., et al., *A point-charge force field for molecular mechanics simulations of proteins based on condensed-phase quantum mechanical calculations.* Journal of computational chemistry, 2003. **24**(16): p. 1999-2012.

127. Case DA, D.T., Cheatham III TE, Simmerling CL, Wang J, Duke RE, Luo R, Crowley M, Walker RC, Zhang W, Merz KM, Wang B, Hayik S, Roitberg A, Seabra G, Kolossvary I, Wong KF, Paesani F, Vanicek J, Wu X, Brozell S, Steinbrecher T, Gohlke H, Yang L, Tan C, Mongan J, Hornak V, Cui G, Mathews DH, Seeting MG, Sagui MG, Babin V, Kollman PA, University of California San Francisco, 2008.

128. Essmann, U., et al., *A smooth particle mesh Ewald method.* The Journal of chemical physics, 1995. **103**(19): p. 8577-8593.

129. Stumm, W., Morgan, J.J., *Aquatic Chemistry: Chemical Equilibria and Rates in Natural Waters*1996, New York: Wiley-Interscience.

130. Millero, F.J., *The effect of ionic interactions on the oxidation of metals in natural watersters.* Geochim. Cosmochim. Acta, 1985(49): p. 547-553.

131. Morgan, B. and O. Lahav, *The effect of pH on the kinetics of spontaneous Fe(II) oxidation by O2 in aqueous solution--basic principles and a simple heuristic description.* Chemosphere, 2007. **68**(11): p. 2080-4.

132. Li, N., et al., *Novel Cu(II)-RGD-octapeptides: Synthesis, coordination mode, in vitro anti-platelet aggregation/in vivo anti-thrombotic evaluation and correlation of sequence with nano-structure.* Nanomedicine : nanotechnology, biology, and medicine, 2011. **7**(4): p. 403-409.

133. Barth, A., *The infrared absorption of amino acid side chains.* Progress in biophysics and molecular biology, 2000. **74**(3-5): p. 141-73.

134. Mohamed, G.G. and N.E. El-Gamel, *Synthesis, investigation and spectroscopic characterization of piroxicam ternary complexes of Fe(II), Fe(III), Co(II), Ni(II), Cu(II) and Zn(II) with glycine and DL-phenylalanine.* Spectrochimica acta. Part A, Molecular and biomolecular spectroscopy, 2004. **60**(13): p. 3141-54.

135. Su, C.-C., et al., *Spectroscopic and electronic properties of mixed ligand aminoacidatocopper(II) complexes: Molecular structure of [Cu(4,7-dimethyl-1,10-phenanthroline)(l-phenylalaninato)](ClO4).* Polyhedron, 1999. **18**(18): p. 2361-2368.

136. Humphrey, W., A. Dalke, and K. Schulten, *VMD: visual molecular dynamics.* Journal of molecular graphics, 1996. **14**(1): p. 33-8, 27-8.
137. *The Pymol Molecular Graphics System*, LLC.